Thèse de doctorat

Pour obtenir le grade de Docteur de

l'UNIVERSITE POLYTECHNIQUE HAUTS-DE-FRANCE ET L'INSA HAUTS-DE-FRANCE

Discipline, spécialité selon la liste des spécialités pour lesquelles l'Ecole Doctorale est accréditée :

Automatique

Présentée et soutenue par Marcelino SANCHEZ PANTOJA
le 18/12/2020, à Valenciennes

Ecole doctorale : Sciences Pour l'Ingénieur (ED SPI 072)

Equipe de recherche, Laboratoire :

Laboratoire d'Automatique, de Mécanique et d'Informatique Industrielles et Humaines (LAMIH - UMR 8201)

Hybrid Vehicle Design and Control

Conception et Commande de Véhicules Hybrides

JURY

Président du jury
- Ossart, Florence. Pr. Sobornne Université.

Rapporteurs
- Sciarreta, Antonio. Dr, HDR. ASN, IFP Energies nouvelles.
- Colin, Guillaume. Dr, HDR. Université d'Orléans, France.

Examinateurs
- Bideaux, Eric. Pr. INSA Lyon

Directeur de thèse
- Delprat, Sébastien. Pr. UPHF, INSA HdF, LAMIH UMR CNRS 8201.

Co-encadrant de thèse
- Hofman, Theo. Dr, HDR. Technische Universiteit Eindhoven (TU/e).

Membres invités
- Negenborn, Rudy. Pr. Delft University of Technology.

Abstract

This work is concerned with the development of hybrid electric vehicle technologies. It is split into three main topics:

- The first topic, covered in Chapter 2, is concerned with the energetic supervisory control that, by taking advantage of the extra degrees of freedom present in a hybrid vehicle, satisfies the power demand from the driver such that the total fuel consumption is minimized. This supervisory control can be cast as an optimal control problem. The contribution of this work is an approach based on Pontryagin's minimum principle, penalty functions, and an implicit Hamiltonian minimization that allows computing the offline energy management under multiple states subject to path constraints. The approach is used to compute the supervisory control, also known as energy management strategy, for two case studies: (1) a series hybrid electric vehicle (modeled as a mixed input-state constrained optimal control with two states) under cold operating conditions and (2) a dual series hybrid electric vehicle (modeled as a mixed input-state constrained optimal control problem with two states and two inputs). The approach is shown to be up to 46 times faster than dynamic programming.

- The second topic, covered in Chapter 3, is concerned with the undesired driveshaft oscillations. In a vehicle with a gear-based transmission, this phenomenon is mainly noticeable at low gear ratios (and therefore low speeds) when the torsional dynamics of the driveshaft are excited with large torque values. The contribution of this work is the design and implementation of a damping controller able to significantly reduce the undesired oscillations. The controller is implemented by adding a damping torque signal to the reference torque of the electric machine commanded by the energetic supervisory control (energy management strategy). No additional actuators are required for the implementation of the controller. Moreover, the damping controller is effective without significantly interfering with the energetic supervisory control.

- The third topic, covered in Chapter 4, is the design of hybrid vehicle architectures. The complex task of automatically computing the optimal architecture design subsumes other important tasks such as the optimization of the supervisory control, the technology of the powertrain components, and the parametrization of such components. In this work, building upon existing results, the powertrain components are fitted into piecewise affine convex models. In this convex formulation, the hybrid powertrain is seen as a power network. The main contribution is the

formulation of the energy management and the architecture design in a simultaneous framework via mixed-integer linear programming.

Keywords: Hybrid electric vehicle, energy management, state constraints, optimal control, Pontryagin Minimum Principle, convex programming, powertrain architecture design, driveshaft oscillations.

Résumé

La thèse s'intéresse au développement des technologies de véhicules hybrides. Elle comprend trois thèmes principaux:

- En portant des degrés de liberté supplémentaires du véhicule hybride, la stratégie de gestion énergétique répond aux demandes de puissance du conducteur de telle manière que la consommation totale d'essence soit minimisée. La contribution sur ce sujet est une méthodologie basée sur le principe du minimum de Pontryagin, des fonctions de pénalité, et la minimisation implicite du Hamiltonien. La méthodologie proposée est capable de calculer la stratégie de gestion énergétique, avec plusieurs contraintes sur les états. La méthodologie est illustrée avec deux exemples. Il est montré que la méthodologie proposée est jusqu'à 46 fois plus rapide que la programmation dynamique.

- Dans un véhicule avec une boîte de vitesses, la présence des oscillations dans la transmission, qui est plus notable quand le véhicule roule avec le 1^{er} ou 2^{nd} rapport engagé (et donc aux bas vitesses), arrive lorsque la dynamique de torsion de la transmission est excitée par des couples qui changent soudainement et qui atteignent des valeurs considérables. Notre contribution sur ce sujet est la conception et l'implémentation d'une loi de commande réduisant ces oscillations qui diminuent l'agrément de conduite. La commande est mise en œuvre en ajoutant un signal de commande à la consigne de couple de la machine électrique demandée par le superviseur énergétique. La loi de commande ne requiert aucun actionneur supplémentaire. En outre, elle n'interfère pas avec la stratégie de gestion énergétique, et par conséquent, son effet sur la consommation d'essence est négligeable.

- Le calcul de l'architecture optimale d'un véhicule hybride est un problème considérablement complexe qui englobe l'optimisation de la stratégie de gestion énergétique, le choix de la technologie des composants du groupe

motopropulseur (GMP), et les paramètres de ces composants. Dans ce travail, en s'appuyant sur des résultats existants, le comportement énergétique des composants du groupe motopropulseur est modélisé par des modèles convexes. Avec ces modèles convexes, le GMP hybride est considéré comme un réseau de puissance. La contribution principale est la formulation de la stratégie de gestion énergétique et du choix de l'architecture optimales via un problème de programmation linéaire mixte en nombres entiers.

Mots-clés: Véhicule hybride électrique, gestion énergétique, contraintes sur l'état, commande optimale, principe du minimum de Pontryagin, optimisation convexe, conception des GMPs, oscillations de torsion.

Contents

List of Figures

List of Tables

Chapter 1

Introduction

This chapter begins by explaining the relevance of the technology of hybrid electric vehicles (HEVs). It later explains what is an HEV, what are its main characteristics, and how it can reduce fuel consumption. The next section further explains how the energy management, the principal feature of an HEV, is computed and it includes a brief state of the art on the algorithms for energy management currently found in the literature. The contributions made in this work are presented in Section 1.4. The last two sections of the chapter present a list of publications and the organization of the rest of the manuscript.

1.1 Why hybrid electric vehicles

HEVs are one of the approaches aimed to reduce the consumption of fossil fuel resources used for transportation. The main reason why we are interested in reducing the amount of fuel that our vehicles consume comes from the fact that their consumption generates pollutants: CO_2, NO_x, particulate matter, hydrocarbons, and CO. These pollutants have damaging effects on the environment that range from local to a global. The local effects are the deterioration of air quality in urban areas [6, 7]. The global effects come from the emission of CO_2, a gas that contributes to climate change (greenhouse effect [8]) [9, 10]. In order to reduce these damaging effects, several government entities around the world have imposed progresively stricter fuel efficiency and pollution restrictions. At least ten government entities, representing the 80% of the light-duty vehicle world market, have imposed fuel efficiency and/or CO_2 emission standards for new light-duty vehicles [11]. One of these government entities, the Europen Union (EU), has gone as far as to set the target of reducing the average CO_2 emissions from new passenger vehicles by a 37.5% by 2030 with respect to the CO_2 emissions of 2021 [12]. If this tendency

continues and no drastic developments are made on increasing the efficiency of internal combustion engines (ICE), in a few decades from now, the only type of vehicles capable of meeting the fuel efficiency and CO_2 emission restrictions will be hybrid and electric vehicles. For instance, according to the United States (US) Environmental Protection Agency, the hybrid version of a 2020 Toyota Camry can achieve 55% less CO_2 emissions and a around 44% better fuel economy than the conventional 2020 Toyota Camry [13]. Moreover, according to a study from Emission Analytics, the average hybrid vehicle in the EU and US markets, having a 1.1 kWh battery, has 30% less CO_2 emissions than its conventional counterpart [14]. Nevertheless, hybrid and electric vehicles are by no means the only way in which CO_2 emission reduction targets can be achieved. There are other methods that may play a significant role in meeting these targets as well, for instance, the replacement of fossil fuels by low-carbon fuels, such as biofuels and e-fuels [15]. In fact, it is likely that meeting the CO_2 emission reduction targets will require the simultaneous implementation of several approaches [16].

1.2 What is a hybrid electric vehicle and how does it improve fuel efficiency

A vehicle is defined as hybrid if it is propelled by more than one source of energy and at least one these sources is reversible. An HEV is built by adding a battery pack and/or a supercapacitor (the reversible sources) and one or more electric machines (EM) to a conventional ICE vehicle. Fig. 1.1a and 1.1b compare the powertrains of an HEV and a conventional vehicle. An HEV can also be built combining a battery pack and/or a supercapacitor (the reversible sources) and one or more electric machines (EM) with a fuel-cell (nonreversible source), see Fig. 1.1d. The presence of the aforementioned components gives an HEV more degrees-of-freedom, with respect to a conventional vehicle, when meeting the power demand from the driver. The extra degrees-of-freedom can be used to achieve a better fuel consumption by:

- operating the ICE in its most efficient region available,
- recovering energy via regenerative braking,
- shutting down the engine during stand-still and low-power driving conditions.

HEVs can be classified in mild, full and plug-in HEVs. The ability of an HEV to improve fuel efficiency depends on to which of these classifications it belongs:

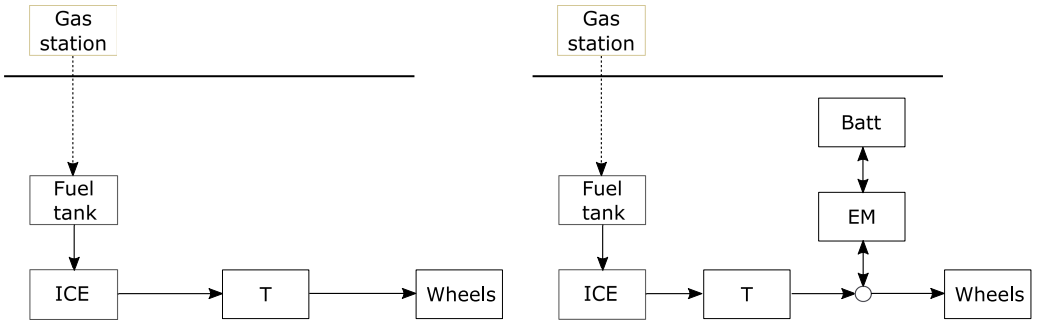

(A) A conventional ICE architecture

(B) A parallel HEV architecture.

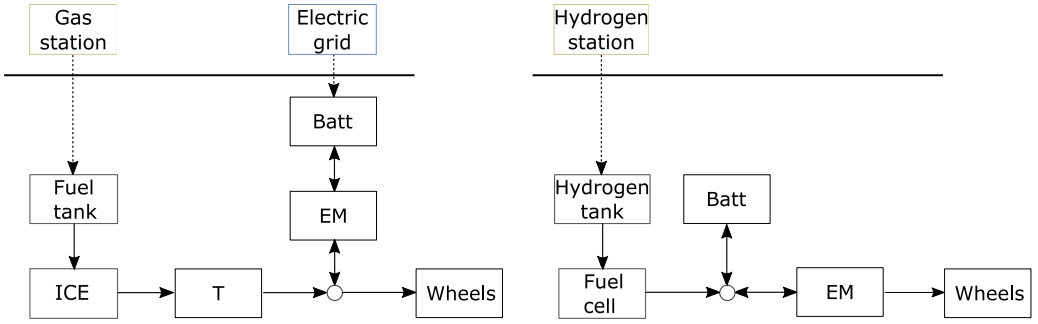

(C) A parallel plug-in HEV architecture.

(D) A fuel-cell HEV architecture

FIGURE 1.1: Four different vehicle architectures: (a) a conventional ICE arhitecture; (b) a parallel HEV architecture; (c) a parallel plug-in HEV architecture; (d) a fuel-cell HEV architecture. In these figures, T stands for transmission.

- A mild HEV has the smallest energy storage system and EM of the three types of HEV: around 0.4 kWh of capacity for the storage system. This HEV only has some of the three capabilities listed above: turning off the engine at standstill and regenerative braking. It does not turn off the engine during low-power driving conditions since its EM is too small to propel the vehicle by its own.

- A full HEV improves fuel efficiency with respect to a mild HEV through a bigger storage system (around 1.8 kWh of capacity) and more powerful EMs. It can perform all of the three capabilities listed above: operating the ICE in its most efficient region available, recovering energy via regenerative braking, shutting down the engine during stand-still and low-power driving conditions. Moreover, it can recover more energy via regenerative braking than a mild HEV.

- A Plug-in HEV can further improve the fuel efficiency by significantly increasing the size of its components, the storage system (typically between 5 and 20 kWh) and the EMs, and by having a battery pack that can be directly recharged from the grid, see Fig. 1.1c.

In the rest of the thesis, every discussion about HEVs will refer to full HEVs, unless it is explicitly stated otherwise. Other factors that influence an HEV performance are its architecture and the technology used by its components. A limitless number of HEV architectures can be conceived. The most common architectures are the series, parallel and power-split architectures. After an architecture has been chosen, it can be implemented using different technologies. For example, an ICE may be spark-ignited or compression-ignited, the battery pack may be built using lead–acid, or nickel-metal hydrides, or lithium-on cells, the EMs may be permanent-magnet, or induction, or switched reluctance machines, and the transmission may be a gearbox or a continuous variable transmission (CVT) technology. However, the chance of an HEV being built and deployed on the roads does not depend solely on its performance but also on its cost-effectiveness. A high-performance HEV may never hit the roads if it is prohibitively expensive.

1.3 Energy management strategies

The algorithm that handles the extra degrees-of-freedom such that the total fuel consumption is minimized is known as energy management strategy (EMS) [17]. Its operation is depicted in Fig. 1.2. Its inputs are the power request from the driver and the state of the vehicle's components; its outputs are set-points to the low-level controllers. Although the main objective of an EMS is to improve the fuel efficiency, additional criteria may be considered in its problem formulation as well, e.g., reducing the emission of pollutants (the optimal energetic operation of the vehicle may not coincide with the optimal operation of its catalyst) [18, 19], improving the driver's comfort [20, 21], and prolonging the lifetime of the energy sources [22, 23].

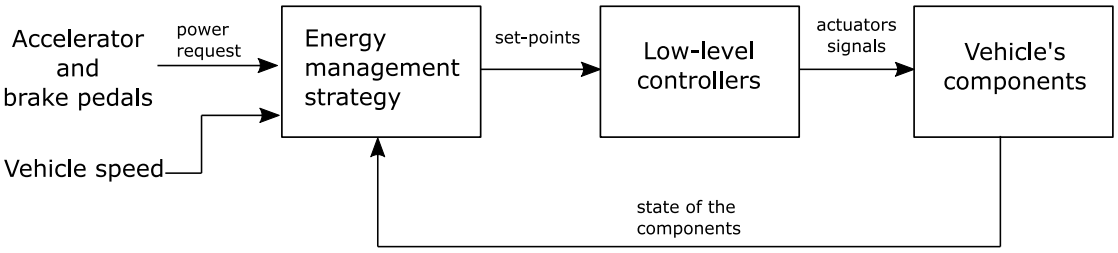

FIGURE 1.2: Diagram of the EMS operation.

1.3.1 Real-time energy management

Real-time EMS [24] are used to operate actual vehicles and can only rely on causal algorithms. Examples of real-time EMS techniques are model predictive control (MPC) [25], heuristic based control [26], and the equivalent consumption minimization strategy (ECMS) [27].

In MPC approaches, the optimal control problem equivalent to the EMS is computed at every sampling time but only the first control sequence is used as set-point for the vehicle's controllers. This receding horizon feature helps to overcome the uncertainties and unmodeled dynamics ignored during the design of the controller. One advantage of the MPC method is that the constraints on the states and inputs can be included in the problem formulation explicitly. Its main drawbacks are that (i) its performance depends on the availability of sufficiently accurate predictions of the future driving conditions and (ii) that it can required an important computation effort. The prediction of the future driving conditions can be estimated using sensors such as GPS navigation systems, cameras, LIDARs, general information about the traffic conditions ahead, exponential decay models for the future torque signal [25], and stochastic models for the driving profile [28].

Alternatively, heuristic rules can be designed using expert knowledge about the vehicle's powertrain and/or analyzing the offline solutions under different driving conditions [29, 30]. This approach can lead to close to optimal results and it has the advantage of requiring an small computational effort. The main drawback of this approach is that the heuristic rules designed for one vehicle architecture cannot be easily translated to another architecture. Therefore, the design of the heuristic rules can be a time-consuming task.

The Equivalent consumption minimization strategy (ECMS) is yet another real-time EMS [31]. ECMS is based on the fact that, in the case of charge sustaining HEVs, the energy depleted from the battery will be eventually replenished by the ICE, thus, consuming fuel. The ECMS consists in the instantaneous minimization of a function formed by the sum of the fuel consumption rate and the electric power provided by the battery pondered by an equivalent factor which accounts for the amount of fuel that will be required to recharge the battery. Although it was originally conceived using engineering intuition, it can be derived from the Pontryagin minimum principle (PMP) if the equivalent factor is seen as a co-state [32]. In order to achieve close to optimal results, ECMS requires a good estimate of the optimal co-state trajectory, which can be exactly determined only if the driving conditions are perfectly known beforehand. Despite this, the ECMS can achieve close to optimal results without any *a priori* knowledge of the driving profile. The main advantages of the ECMS are that it can be more easily adapted to different powertrain topologies than heuristic based approaches and that it requires a smaller computational effort than MPC methods. Its main drawback is that it cannot explicitly handle state constraints.

1.3.2 Offline energy management

In simulation, finding the offline EMS consists in computing (eventually, in a non-causal way) the ultimate performance of the HEV. In practice, the obtained results allow assessing, from an energy consumption perspective, different vehicle architectures and component sizing [33]. They can also be used to evaluate the performance of real-time energy management algorithms. EMS in its most general form can be formulated as an optimal control problem with:

- mixed input-state constraints,
- discrete and continuous inputs, and
- discrete and continuous dynamics.

The methods for solving this optimal control problem can be classified in three groups:

- dynamic programming (DP),
- *direct-approach* methods, and
- *indirect-approach* methods.

1.3.2.1 Dynamic programming

In the DP approach, all the variables, inputs, states and time, are quantized. Then, the resulting discrete static optimization problem is solved to determine the optimal EMS. The DP approach is widely used in the literature of HEV, since it can solve the EMS in its most general form, i.e, with hybrid dynamics and input and state constraints. The main drawback of this method comes from its computational expensiveness, referred as the *curse of dimensionality* [34]. Namely, the number of elementary operations has an exponential relationship with respect to the number of states and inputs in the problem formulation. Likewise, the memory requirements increase exponentially with respect to the number of states. As a consequence, DP is, usually, restricted to problems with only one [35, 36], or two continuous states [37, 38].

1.3.2.2 Direct-approach methods

In the *direct-approach* methods, only the time is often quantized (finite-time problems). The resulting static minimization problem is solved using mathematical programming techniques such as nonlinear programming, e.g., sequential quadratic programming

(SQP) [39, 40], or convex programming, e.g., second-order cone programming (SOCP) [41], quadratic programming (QP) [42], and linear programming (LP) [43, 44]. State constraints can be taken into account. Optimizing discrete controls leads to very large mixed-integer programming problems due to the considered long optimization horizon (typically, more than 1000 time steps). These problems are not tractable in general, even if they are restricted to be mixed-integer linear programming (MILP) problems. Nonetheless, when only continuous controls are considered, the direct approach does not posses the *curse of dimensionality* suffered by DP, therefore, it can be applied to obtain the optimal EMS, when several continuous states are considered. Moreover, it has been even applied to obtain, simultaneously, the optimal EMS and the optimal sizing of the main powertrain components [45].

1.3.2.3 Indirect-approach methods

In the group of indirect methods, the calculus of variations or the Pontryagin minimum principle (PMP) is applied to obtain optimality conditions. The original EMS is then reduced to a simpler equivalent problem, namely, a boundary value problem (BVP). Hybrid-PMP [46, 47] allows considering both continuous and discrete systems, and thus, handling discrete controls signals, although they can lead to singular control issues [48, 49]. State constraints lead to many theoretical difficulties, and there is no algorithm available to efficiently derive a solution in the general case. An algorithm is proposed in [50] to solve the EMS problem restricted to a single state.

1.4 Contribution

The contribution of the this work is in three important topics in the filed of hybrid vehicle technology. How these topics are related and a brief explanation of the contributions made on each of these topics will be discussed in the following. The first topic covered is the main characteristic of an HEV: the EMS. In this work, its offline version is considered, Section 1.4.1. In an HEV, having the energetic performance as the paramount objective may lead to the replacement or removal of components that provide a passive damping to the driveline, i.e, an energetically efficient driveline may be underdamped, and hence present driveshaft oscillations noticeable enough to affect the driver's comfort. This drawback may be overcome by taking advantage of the additional actuators available in a hybrid powertrain to implement an active damping controller. The main constraint of this controller is that it should not interfere with the EMS. The design and implementation of this damping controller is the second topic covered in this work, Section 1.4.2. The third and last topic, Section 1.4.3, is the optimal design of powertrain

architectures. This is the most general topic and it can subsume all the other ones: we cannot determine the optimal architecture without first solving the EMS and we could include the maximization of the driveline damping in the problem formulation affecting the relevance of the second topic. In this work, the single criterion to be considered for computing the optimal architecture is the minimization of the total losses along the powertrain, i.e., the EMS is included in the problem formulation but damping maximization is not. The rest of this section explains the contributions made on each topic.

1.4.1 State constrained energy management for HEVs: an implicit Hamiltonian minimization approach

The energy management under several constrained states can be solved using the penalty function approach. It consists in adding an additional cost to the criterion that forces the state to stay in the feasible region. This approach converts the state constrained problem into an unconstrained one that can be solved using the classical PMP [51, 52]. Nevertheless, the resulting optimality conditions are significantly more difficult to solve [53].

The contribution of this work is a novel method for the minimization of the Hamiltonian that overcomes the difficulties found in the penalty-based approaches to satisfy the optimality conditions. The novel method is based on an implicit Hamiltonian minimization that, under strict convexity assumptions, can solve the EMS formulated with n states and m inputs under mixed input-state constraints. Although other penalty approaches have been successfully applied to the EMS under state constraints, they have been so far restricted to formulations with only one state [51, 52]. Increasing the number of states and inputs is relevant since it is necessary to produce a more accurate representation of the vehicle and all its subsystems that have an effect on the energy management [54].

1.4.2 Energy management and active damping of the side-shaft oscillations

Beyond the energetic management, the extra actuators in an HEV can help mitigate the presence of drive-shaft oscillations. In a vehicle with a gear-based transmission, the driveshaft oscillations are mainly noticeable at the first and second gear, and therefore at relatively low speeds: when a low gear is engaged and the driver demands strong accelerations, the driveshaft experiences steep and particularly high torque changes, thus, exciting its torsional dynamics to the point of producing noticeable torque and speed oscillations. These oscillations affect the driver's comfort and can wear off the

driveline components [55, 56]. The contribution of the thesis is a control law based on a discrete RST approach able to mitigate these oscillations without significantly interfering with the EMS: it is found in simulation that the total fuel consumption increases only in a +0.26% when a synthetic driving mission designed to have a high number of steep torque changes in a short period of time is used. This synthetic driving cycle is unlikely to arrive in normal driving conditions and as such it is used as a worst case scenario. The controller does not require the installation of new hardware and it has been validated experimentally.

1.4.3 Architecture design for hybrid electric vehicles

The optimal design of powertrain topologies is a complex nonconvex and nonlinear problem. It is a nondeterministic polynomial time (NP) problem in general. For this reason, the works available in the literature constraint the number of components from which the topology architectures can be built [4, 5, 57]. In order to answer the question of what is the best topology design, one has to simultaneously determine, what technology should be used for each of the components, how should the size of each of the components be chosen together with the EMS. In this work, building upon existing results [42, 43, 58] the powertrain components are fitted into piecewise affine convex models. In this convex formulation, the hybrid powertrain is modeled as a power network. The main contribution is the formulation of the energy management and the architecture design in a simultaneous framework via mixed-integer linear programming.

1.5 List of publications

The following publications were made on the topics presented in this work:

- International journals:
  - Energy management of hybrid vehicles with state constraints: A penalty and implicit Hamiltonian minimization approach (2020); M. Sanchez, S. Delprat, T. Hofman. Applied Energy, 260, 114149.
- International conferences:
  - Hybrid Vehicle Energy Management: Avoiding the Explicit Hamiltonian Minimization; M. Sanchez; S. Delprat. 2018 IEEE Vehicle Power and Propulsion Conference (VPPC). IEEE, 2018. p. 1-5.

  - Optimal Hybrid Vehicle Energy Management and Active Damping of the Side-Shaft Oscillations; M. Sanchez, S. Delprat, W. Lhomme, F. Tournez ,2018 IEEE Vehicle Power and Propulsion Conference (VPPC). IEEE, 2018. p. 1-5.

The following publications were made outside the scope of the main topics presented in this work:

- International journals:
  - A novel parameter-dependent polynomial approach for robust automated lane keeping (2020); M. Sanchez, J. Alvarez, S. Delprat, M. Bernal. International Journal of Fuzzy Systems. *Status*: accepted for publication.
  - A Tighter Exact Convex Modelling for Improved LMI-Based Nonlinear System Analysis and Design (2020); S. Delprat, J. Alvarez, M. Sanchez, M. Bernal. IEEE Transactions on Fuzzy Systems.

1.6 Organization

Contribution 1.4.1 is found in Chapter 2. Contribution 1.4.2 is found in Chapter 3. Contribution 1.4.3 is found in Chapter 4. At last, Chapter 5 presents conclusions and future work perspectives for all the topics covered in the thesis.

Chapter 2

State-constrained energy management for HEVs: an implicit Hamiltonian minimization approach

2.1 General energy management strategy

The algorithm that handles the extra degrees-of-freedom such that the total fuel consumption is minimized is known as energy management strategy (EMS) [17]. In its more general form, the EMS can be cast as an optimal control problem with:

- nonlinear and nonconvex functions,
- mixed input-state constraints,
- discrete and continuous inputs, and
- discrete and continuous dynamics.

Let us use $u(t)$ to denote the vector of continuous inputs, $\vartheta[k]$ the vector of discrete inputs, $x(t)$ the vector of continuous state dynamics, and $\xi[k]$ the vector of discrete state

dynamics. The general EMS can be posed as the following optimal control problem:

$$\min_{u(t),\vartheta[k]} J = \int_0^{t_f} \dot{m}_f\left(u(t), \vartheta[k]\right) \mathrm{d}t, \tag{2.1a}$$

subject to:

$$\dot{x}(t) = f(x(t), u(t), \xi[k], \vartheta, w(t)) \tag{2.1b}$$

$$\xi[k+1] = g(\xi[k], \vartheta[k], w(t)) \tag{2.1c}$$

$$x \in X(t), \tag{2.1d}$$

$$\xi \in \Xi[k] \tag{2.1e}$$

$$u \in U(t, w(t))), \tag{2.1f}$$

$$\vartheta \in \Theta(t, w(t)), \tag{2.1g}$$

with $\dot{m}_f$ (g/s) the fuel consumption rate, $(\cdot)[k]$ denoting $(\cdot)\left(t \in k \cdot \Delta t\right)$, $k \in \mathbb{N}$, $\Delta t \in [0, t']$, $w(t)$ the vector of exogenous variables, and where X, Ξ, U, and Θ are nonconvex sets in general. The vector of exogenous variables typically includes the power demand from the driver, the vehicle longitudinal speed and the road slope. In short, EMS seeks to minimize the total fuel consumption for a given *driving mission* under several constraints. The main constraint being that the power demand from the driver has to be satisfied all along the driving mission ($t \in [0, t_f]$).

In simulation, the power demand from the driver, for a given driving mission, is commonly computed using a quasi-static approach [17]. This is the approach taken in this work. Let us as denote m (kg) as the vehicle mass, $v(t)$ (m/s) as the vehicle longitudinal velocity, r (m) as the radius of the wheels, c_{rr} (-) as the rolling resistance coefficient, g (m/s^2) as the acceleration of gravity, α (rad) as the grade of the road, ρ (kg/m^3) as the air density, A_{s} (m^2) as the vehicle frontal area, and c_{air} (-) as the aerodynamic drag coefficient. In the quasi-static approach, the vehicle is modeled as a lumped mass under the action of 4 forces:

$$m_{\mathrm{eq}} \cdot a_{\mathrm{v}} = F_{\mathrm{trac}} - F_{\mathrm{rr}} - F_{\mathrm{slope}} - F_{\mathrm{air}}, \tag{2.2}$$

with $m_{\mathrm{eq}} = m + I_{\mathrm{v}}(t)/r^2$ (kg) the equivalent mass and $I_{\mathrm{v}}(t)$ (kg·m^2) the powertrain total moment of inertia seen from the wheels[1], $a_{\mathrm{v}} = \mathrm{d}v/\mathrm{d}t$ (m/s^2) the vehicle acceleration, F_{trac} (N) the force provided by the vehicle powertrain, $F_{\mathrm{rr}} = c_{\mathrm{rr}} \cdot m \cdot g \cdot \cos\alpha$ (N) the rolling resistance of the wheels, $F_{\alpha} = m \cdot g \cdot \sin\alpha$ (N) the force exerted on the vehicle, by the acceleration of gravity, due to the slope of the road, and $F_{\mathrm{air}} = \frac{1}{2} \cdot \rho \cdot c_{\mathrm{air}} \cdot A_{\mathrm{s}} \cdot v^2$ (N) the aerodynamic drag force. Therefore, assuming that $v(t)$, $a_{\mathrm{v}}(t)$ and $\alpha(t)$ are known

[1] $I_{\mathrm{v}}(t)$ depends on the vehicle architecture and the clutch and gears state of engaged/disengagement.

and solving (2.2) for F_{tract}, the power demand can be computed as follows:

$$P_w(t) = F_{\text{trac}}(t) \cdot v(t). \tag{2.3}$$

$$P_w(t) = (m_{\text{eq}} \cdot a_{\text{v}} + F_{\text{rr}} + F_\alpha + F_{\text{air}}) \cdot v(t), \tag{2.4}$$

From a torque and angular velocity perspective, the powertrain has to provide the following torque signal at the wheels:

$$T_{\text{w}}(t) = (m_{\text{eq}} \cdot a_{\text{v}} + F_{\text{rr}} + F_\alpha + F_{\text{air}}) \cdot r \tag{2.5}$$

under the kinematic constraints imposed by the angular speed:

$$\omega_w(t) = v(t)/r, \tag{2.6}$$

in order to complete the driving mission. Quasi-static models are considered valid for energy management applications because most of the energy flowing through the vehicle is carried by low-frequency signals, which makes reasonable to neglect the transient response of the vehicle components. As mentioned in the previous chapter, additional criteria may be added to (2.1a). For instance, minimizing the total amount of pollutant and green-house effect tailpipe emissions [18, 19], improving the driver's comfort [20, 21], and prolonging the lifetime of the energy sources [22, 23]. In simulation, the methods for solving (2.1) can be classified in three groups:

- dynamic programming (DP),
- *direct-approach* methods, and
- *indirect-approach* methods.

The contribution of this work lies within the third group: the indirect-methods. However, a general discussion on the three groups of methods will be provided before entering into the details of the contribution.

2.2 State-of-the-art

2.2.1 Dynamic programming

In the DP approach, all the continuous variables, inputs, states and time, are quantized:

$$\min_{u[k],\vartheta[k]} J = \sum_{k=0}^{N-1} \dot{m}_f\left(u[k],\vartheta[k]\right)\cdot\Delta t, \tag{2.7a}$$

subject to:

$$\dot{x}[k+1] = f(x[k],u[k],\xi[k],\vartheta[k],w[k]) \tag{2.7b}$$

$$\xi[k+1] = g(\xi[k],\vartheta[k],w[k]) \tag{2.7c}$$

$$x \in X[k], \tag{2.7d}$$

$$\xi \in \Xi[k] \tag{2.7e}$$

$$u \in U(k,w[k]), \tag{2.7f}$$

$$\vartheta \in \Theta(k,w[k]), \tag{2.7g}$$

with Δt the time period of the quantization, $k \in \mathbb{N}$; and where $X \subset \mathbb{R}^n$, $\Xi \subset \mathbb{N}^{n_d}$, $U \subset \mathbb{R}^m$, and $\Theta \subset \mathbb{N}^{m_d}$ are finite sets. Then, the resulting discrete static optimization problem, (2.7) is solved to determine the optimal EMS. The DP approach is widely used in the literature, since it can solve the EMS in its most general form and its solution is globally optimal. The DP algorithm implements a backwards and a forwards simulation. The backwards simulation of the DP algorithm is summarized in Algorithm 1. By ana-

Algorithm 1 Backward sub-routine of the DP algorithm. Adapted from [17].

for $k = N-1:0$ **do**
  for all $x \in X$, $\xi \in \Theta$ **do**
    for all $u \in U$, $\vartheta \in \Theta$ **do**
      $x[k+1] = f\left(x,u,\xi,\theta,w[k]\right)$
      $\xi[k+1] = g\left(\xi,\theta,w[k]\right)$
      $L = \dot{m}_f(u,\theta)\cdot\Delta_t$
      $J\left(u,\vartheta\right) = L + J_{\text{ctg}}\left(x[k+1],\xi[k+1],k+1\right)$
    end for
    $J_{\text{ctg}}(x,\xi,k) = \min J\left(u,\vartheta\right)$
    $[U_{\text{ctg}}(x,\xi,k),\Theta_{\text{ctg}}(x,\xi,k)] = \arg\min J\left(u,\vartheta\right)$
  end for
end for

lyzing this algorithm (pseudocode) and using $|.|$ to define the cardinality of a set, it can be inferred that its computational complexity is given by $\mathcal{O}\left(N\times|X|\times|\Xi|\times|U|\times|\Theta|\right)$: it grows linearly with respect to the length of the driving mission and the cardinality of each set. However, $|\Xi|$ and $|\Theta|$ are usually small with respect to $|X|$ and $|U|$. For

this reason, we will focus on the effect that continuous states and inputs have on the computation complexity. Assuming a grid with $\mathcal{X}$ values for each of the n continuous states and a grid with $\mathcal{U}$ values for each of the m continuous inputs, we have $|X| = \mathcal{X}^n$ and $|U| = \mathcal{U}^m$, thus, the computational complexity grows exponentially with respect to the number of continuous inputs and states:

$$\mathcal{O}(N \times \mathcal{X}^n \times \mathcal{U}^m \times |\Xi| \times |\Theta|), \tag{2.8}$$

Moreover, from lines 7, 9, and 10 of the algorithm, it can be concluded that the memory requirements are determined by matrices $J(u, \vartheta)$ which contains $U^m \times |\Theta|$ real numbers, $J_{\text{ctg}}(x, \xi, k)$, which contains $N \times \mathcal{X}^n \times |\Xi|$ real numbers, $U_{\text{ctg}}(x, \xi, k)$ which contains $N \times \mathcal{X}^n \times |\Xi|$ m-length real vectors or $m \times N \times \mathcal{X}^n \times |\Xi|$ real numbers, and $\Theta_{\text{ctg}}(x, \xi, k)$, which contains $N \times \mathcal{X}^n \times |\Xi|$ m_d-length integer vectors or $m_d \times N \times \mathcal{X}^n \times |\Xi|$ integer numbers, thus:

$$\mathcal{O}\left((m + m_d) \times (N \times \mathcal{X}^n \times |\Xi|) + \mathcal{U}^m \times |\Theta|\right), \tag{2.9}$$

Therefore, the memory requirements also grow exponentially with respect to the number of continuous inputs and states. In general, $\mathcal{X}$ is much greater than $\mathcal{U}$. For HEV applications in particular, $n \approx m$. Therefore, the memory requirements can be estimated by $m \times N \times \mathcal{X}^n$ for HEV applications.

Let us consider an EMS problem with 1 continuous state and $\mathcal{X} = 2000$, 1 continuous input and $\mathcal{U} = 25$, 1 discrete state and $\Xi = 5$, 1 discrete input and $\Theta = 3$, and a driving mission of length $N = 1000$. Based on (2.8) and (2.9), the number of basic computations and the required number of variables will be estimated as $N \times \mathcal{X}^n \times \mathcal{U}^m \times |\Xi| \times |\Theta|$ and $(m + m_d) \times (N \times \mathcal{X}^n \times |\Xi|) + \mathcal{U}^m \times |\Theta|$, respectively. Assuming that each basic operation takes 1 μ second and each variable requires 64 bits (or 8 bytes) of memory, the total computation time and the total memory requirements can be estimated as 750 seconds and 160 MB, respectively. If we add a continuous state, the computation time grows to $1.5 \cdot 10^6$ seconds or about 17 days. The memory goes up to 320 GB. If a total of three continuous sates are considered, the requirements reach $3 \cdot 10^9$ seconds (or about 95 years!) of computation time and 640 TB of memory! In other words, the requirements become highly prohibitive for $n = 3$ states. This computational expensiveness, referred as the *curse of dimensionality* [34], explains why DP is usually restricted to EMS problems with only one [35, 36] or two continuous states [37, 38]. The estimations on the computational resources required by DP discussed in this paragraph are summarized in Table 2.1.

States $\mathcal{X} = 2000$; $\Xi = 5$	Inputs $\mathcal{U} = 25$; $\Theta = 3$	Computation time (seconds)	Memory
1 continuous; 1 discrete.	1 continuous; 1 discrete.	750	160 MB
2 continuous; 1 discrete.	1 continuous; 1 discrete.	$1.5{\cdot}10^6$	320 GB
3 continuous; 1 discrete.	1 continuous; 1 discrete.	$3{\cdot}10^9$	640 TB

TABLE 2.1: Estimated computation time and memory requirements for the DP algorithm for different number of continuous states. $N = 1000$. Each basic operation is assumed to take 1 μ second. Each variable is assumed to be stored using 64 bits (8 bytes) of memory.

2.2.2 Direct methods

In the *direct-approach* methods, only the time is often quantized (finite-time problems). The resulting static minimization problem is solved using mathematical programming techniques such as nonlinear programming, e.g., sequential quadratic programming (SQP) [39, 40], or convex programming, e.g., second-order cone programming (SOCP) [41], quadratic programming (QP) [42], and linear programming (LP) [43, 44]. State constraints can be taken into account. Optimizing discrete controls leads to (nonconvex) very large mixed-integer programming problems due to the considered long optimization horizon (typically, more than 1000 time steps). These problems are not tractable in general, even if they are restricted to be mixed-integer linear programming (MILP) problems. Nonetheless, when only continuous controls are considered, the direct approach does not posses the *curse of dimensionality* suffered by DP, therefore, it can be applied to obtain the optimal EMS, when several continuous states are considered. Moreover, it has been even applied to obtain, simultaneously, the optimal EMS and the optimal sizing of the main powertrain components [45]. Including discrete controls can be feasible by combining convex programming with another method better suited for dealing with discrete inputs. For instance, it has been combined with DP in an iterative approach in order to compute the EMS of a parallel HEV including discrete variables: engine on/off state and gear-shifting [59]. Necessary and sufficient optimality conditions for the iterative approach are provided therein. Similarly, in [60], convex programming was combined with an indirect approach to compute the EMS of a parallel HEV with engine on/off state.

One of the main difficulties that limits the use of convex programming is the challenge of determining if the concerned mathematical program is indeed a convex program. This is not tractable in general and it may require a high level of expertise. A modeling tool

called *disciplined convex programming* was conceived to ease these expertise requirements on potential convex programming users [61]. A *disciplined convex program* can be straightforwardly identified as such by applying a finite set of rules. Every *disciplined convex program* is a convex program but the opposite is not true: a mathematical program may not be a *disciplined convex program* and still be a convex program. If a mathematical program is indeed a *disciplined convex program*, it can be modeled as such using the Matlab-based tool CVX [62]. Once the *disciplined convex* program has been modeled, CVX will translate it into a standard form suitable for a convex programming solver[2]. CVX has been regularly used in HEV applications. For instance, in [45], [41], [59], and [60], among others.

2.2.3 Indirect methods

In the group of indirect methods, the calculus of variations or Pontryagin minimum principle (PMP) is applied to obtain optimality conditions. The original EMS is then reduced to a simpler equivalent problem, namely, a boundary value problem (BVP). Although the optimality conditions usually do not require any quantization, computing the solution of the BVP does require the quantization of the independent variable whenever an analytic solution is not possible. The conditions offered by PMP are necessary conditions only. Assuming that an optimal solution exists, it can be obtained by computing all the trajectories that satisfy the necessary conditions and then choosing the one with the best performance. If it is proven that only one trajectory satisfies PMP conditions, the necessary conditions become sufficient as well.

2.2.3.1 Classical Pontryagin minimum principle

The original version of PMP [63], referred in this work as *classical PMP*, offers necessary optimality conditions on the assumption of smooth dynamics and absence of path constraints. In other words, it does not allow to consider (2.1c), only allows continuous

[2]Up to its 2.2 version, CVX supports four solvers: SeDuMi, SDPT3, GUROBI, and MOSEK.

inputs in (2.1b), and only terminal constraints in (2.1d):

$$\min_{u(t)} J = \int_0^{t_f} \dot{m}_f\left(u(t)\right) \mathrm{d}t, \tag{2.10a}$$

subject to:

$$\dot{x}(t) = f(x(t), u(t), w(t)) \tag{2.10b}$$

$$x(0) = X(0), \tag{2.10c}$$

$$x(t_f) = X(t_f), \tag{2.10d}$$

$$u \in U(t, w(t))), \tag{2.10e}$$

In order to apply PMP, the Hamiltonian has to be computed first. For (2.10), the Hamiltonian is defined as follows:

$$H(x(t), u(t) \,|\, w(t)) = \dot{m}_f(u(t)) + \lambda(t)^T f(x(t), u(t), w(t)), \tag{2.11}$$

where $\lambda(t) \in \mathbb{R}^n$ is the vector of costates of the optimal control problem. PMP states the following necessary optimality conditions for (2.10) [63]:

$$\dot{\lambda}(t) = -\frac{\partial H\left(x(t), u(t) \,|\, w(t)\right)}{\partial x}, \tag{2.12a}$$

$$u^*(t) = \arg\min_{u(t) \in U} H\left(x(t), u(t) \,|\, w(t)\right). \tag{2.12b}$$

Additionally, for each state x_i that does not have a fixed terminal condition, i.e., $x_i(t_f) \notin X(t_f)$, the following terminal condition has to be added [64, Page 200]:

$$\lambda_i(t_f) = 0. \tag{2.13}$$

2.2.3.2 Hybrid Pontryagin minimum principle

An extended version of PMP allows finding necessary optimality conditions for systems with hybrid dynamics, and thus, handling discrete control signals [46, 47]:

$$\min_{u(t),\vartheta[k]} J = \int_0^{t_f} \dot{m}_f\left(u(t), \vartheta[k]\right), \tag{2.14a}$$

subject to:

$$\dot{x}(t) = f(x(t), u(t), \xi[k], \vartheta, w(t)) \tag{2.14b}$$

$$\xi[k+1] = g(\xi[k], \vartheta[k], w(t)) \tag{2.14c}$$

$$x(0) = X(0), \tag{2.14d}$$

$$x(t_f) = X(t_f), \tag{2.14e}$$

$$u \in U(t, w(t))), \tag{2.14f}$$

$$\vartheta \in \Theta(t, w(t)), \tag{2.14g}$$

Defining the Hamiltonian of (2.14) as follows:

$$H(x(t), \xi[k], u(t), \vartheta[k] \,|\, w(t)) = \dot{m}_f(u(t), \vartheta[k]) + \lambda(t)^T f(x(t), \xi[k], u(t), \vartheta[k], w(t)), \tag{2.15}$$

the necessary conditions of optimality offered by Hybrid-PMP are:

$$\dot{\lambda}(t) = -\frac{\partial H\left(x(t), \xi[k], u(t), \vartheta[k] \,|\, w(t)\right)}{\partial x}, \tag{2.16a}$$

$$\{u(t), \vartheta[k]\} = \arg \min_{\vartheta[k] \in \Theta[k]} \left(\arg \min_{u(t) \in U} H\left(x(t), \xi[k], u(t), \vartheta[k] \,|\, w(t)\right) \right) \tag{2.16b}$$

Again, for each state x_i that does not have a fixed terminal condition, i.e., $x_i(t_f) \notin X(t_f)$, the following terminal condition has to be added:

$$\lambda_i(t_f) = 0. \tag{2.17}$$

However, the inclusion of discrete inputs for EMS applied to HEV may lead to singular control arcs[3] [49]. A singular control arc occurs when, for a non-trivial period of time $[t_1, t_2]$, PMP optimality condition (2.16b) is not enough to compute an optimal control candidate [64].

[3] In some works, this phenomenon was wrongly blamed on numerical inaccuracy [48].

2.3 Motivation

State constraints lead to many theoretical difficulties, and there is no algorithm available to efficiently derive a solution in the general case. An algorithm is proposed in [50] to solve the EMS problem restricted to a single state.

Problems with many constrained states can be handled using the penalty function approach. It consists in adding an additional cost to the criterion that forces the state to stay in the feasible region. This approach converts the state constrained problem into an unconstrained one that can be solved using the classical PMP [51, 52]. Nevertheless, the resulting optimality conditions are significantly more difficult to solve [53].

2.4 Contribution: A penalty function and implicit Hamiltonian minimization approach

The first part of this section explains the penalty function approach: how the constraints of the original EMS can be relaxed by adding nonlinear terms to the Hamiltonian. The second part explains how the PMP optimality conditions can transform the relaxed EMS formulation into an equivalent BVP. The optimal control must be chosen to minimize the Hamiltonian, a given scalar function. The relaxation of the constraints by adding nonlinear terms to the Hamiltonian makes more difficult its explicit minimization. Hence, the last subsection explains the main contribution: an implicit minimization scheme.

The contribution will be explained assuming an EMS with the following form[4]:

$$\min_{\underline{u}(t)\leq u(t)\leq \bar{u}(t)} J = \int_0^{t_f} \dot{m}_f\left(u(t)\right), \tag{2.18a}$$

subject to:

$$\dot{x}(t) = f(x(t), u(t), w(t)) \tag{2.18b}$$

$$\underline{x} \leq x(t) \leq \bar{x}, \tag{2.18c}$$

$$\underline{u}(t) \leq u(t) \leq \bar{u}(t), \tag{2.18d}$$

$$x(0) = X(0), \tag{2.18e}$$

$$x(t_f) = X(t_f), \tag{2.18f}$$

Discrete signals are omitted in EMS (2.18) in order to focus on the handling of the path state constraints, the main contribution of the chapter; since their inclusion may lead to

[4]Throughout the rest of the chapter, an underline ($\_$) and an overline ($\bar{}$) are used to denote minimum and maximum value, respectively.

singular control issues, which would require the explanation of additional methodologies outside the scope of the contribution.

2.4.1 Penalty function approach

In the penalty approach, inequality constraints (2.18c) and (2.18d) are taken into account by adding nonlinear terms, denoted as penalties, to the cost functional, (2.18a). These nonlinear terms drastically increase their values, whenever a constraint is violated (for exterior penalty functions) or close to be violated (for interior and extended penalty functions). These characteristics force the optimal solution to satisfy the constraints. Consider a function P_z defined as follows:

$$P_z = P(z) = \begin{cases} (\underline{z} - z)^n, & z \leq \underline{z} \\ (z - \bar{z})^n, & z \geq \bar{z} \\ 0, & \text{otherwise.} \end{cases} \tag{2.19}$$

with $\underline{z}$ the minimum allowed value for z, $\bar{z}$ the maximum allowed value for z, and $n > 1$ a function parameter. P_z is classified as an exterior penalty function, as it only affects the cost-functional when the constraints have been violated. Define P_u and P_x as the exterior penalty functions for state constraints (2.18c) and input constraints (2.18d), respectively. Given cost functional (2.18a), the penalty approach solves EMS (2.18) by solving an equivalent unconstrained version of the problem:

$$\min_{u(t)\in\mathbb{R}^m} \hat{J}(u) = \int_0^{t_f} \left[\dot{m}_f(u) + \frac{1}{\varepsilon}(P_u + P_x)\right] \mathrm{d}t, \tag{2.20a}$$

subject to:

state dynamics (2.18b), and boundary conditions (2.18e)-(2.18f), (2.20b)

where ε is a real positive parameter pondering the penalty functions P_u and P_x. If ε is small enough, the effect of P_u and P_x increases to force the solution to EMS (2.20), $\hat{J}^*$, to be approximately equal to the solution to EMS (2.18), J^*. Moreover, $\hat{J}^* \to J^*$ as $\varepsilon \to 0$. Therefore, in order to get a fairly accurate approximation for the solution to EMS (2.18), it is sufficient to solve EMS (2.20) for a small enough value of ε. Proofs on the convergence of the penalty approach are given in [65, 66].

2.4.2 Optimality conditions

As mentioned in section 2.2.3.1, necessary optimality conditions for EMS (2.20) can be obtained from PMP. In order to apply PMP, the Hamiltonian of the problem has to be

computed first. The Hamiltonian for EMS (2.20) is given by:

$$H(u, x, \lambda, w) = \dot{m}_f + \frac{1}{\epsilon}\left(P_u + P_x\right) + \lambda^T \dot{x} \tag{2.21}$$

with $\lambda(t) \in \mathbb{R}^n$ denoting the vector of co-states. The necessary optimality conditions for EMS (2.20) are the following [64]: (i) the optimal control, $u^*(t)$, minimizes the Hamiltonian for every possible control:

$$u^*(t) = \arg\min_{u \in \mathbb{R}} \{H\left(u, x, \lambda, w\right)\}, \tag{2.22}$$

(ii) the co-states obey the following dynamics:

$$\dot{\lambda}(t) = -\frac{\partial H}{\partial x}, \tag{2.23}$$

and (iii) for each state x_i that does not have a fixed terminal condition, i.e., $x_i(t_f) \notin X(t_f)$, the following terminal condition has to be added [64, Page 200]:

$$\lambda_i(t_f) = 0. \tag{2.24}$$

It is not always possible to obtain u^* explicitly. Nevertheless, let us assume by now that an explicit expression can be computed for u^* and let us denote this expression as $\Pi(u, x, \lambda, w)$:

$$u^*(t) = \Pi(u, x, \lambda, w). \tag{2.25}$$

On the assumption that an optimal solution exists and that H satisfies the following sufficient strict convexity condition with respect to u:

$$\frac{\partial^2 H}{\partial u^2} > 0, \tag{2.26}$$

conditions (2.22)-(2.24) become necessary and sufficient optimality conditions [67, 68]. Using (2.22)-(2.25), EMS (2.20) can be formulated as an equivalent boundary value problem (BVP):

$$\dot{x}(t) = f(x(t), \Pi\left(u(t), x(t), \lambda(t), w(t)\right), w(t)) \tag{2.27a}$$

$$\dot{\lambda}(t) = -\frac{\partial H}{\partial x}, \tag{2.27b}$$

$$\lambda_i(t_f) = 0, \forall x_i(t_f) \notin X(t_f) \tag{2.27c}$$

$$\text{state boundary constraints (2.18e)} - \text{(2.18f)}. \tag{2.27d}$$

This BVP can be solved through different numerical methods, e.g. shooting, multiple-shooting, or collocation [69][70]. Due to its numerical stability, a collocation method

has been chosen in this work [70]. The use of penalty functions increases the difficulty for minimizing the Hamiltonian, which is a necessary optimality condition. A solution to overcome this issue is presented in the following subsection.

2.4.3 Implicit Hamiltonian minimization

Firstly, consider the minimization of the Hamiltonian with respect to the input vector: optimality condition (2.22). For an unconstrained input signal and assuming that H satisfies strict convexity condition (2.26), the optimal control, $u^*(t)$, can be defined from first order optimality conditions as follows:

$$u^*(t) = \left\{ u(t) \,|\, \frac{\partial H\left(u, x, \lambda, w\right)}{\partial u(t)} = 0 \right\}. \tag{2.28}$$

In general, (2.28) cannot be solved explicitly but an implicit Hamiltonian minimization can be used instead. Let us define $q(t) \in \mathbb{R}^m$ as follows:

$$q(t) = \frac{\partial H\left(u, x, \lambda, w\right)}{\partial u}. \tag{2.29}$$

The following equivalent conditions for $u^*(t)$ can be obtained from $q(t)$:

$$q(0) = 0, \tag{2.30}$$

$$\dot{q}(t) = 0, \tag{2.31}$$

From (2.31), it follows:

$$\frac{\partial q}{\partial u}\dot{u} + \frac{\partial q}{\partial x}\dot{x} + \frac{\partial q}{\partial \lambda}\dot{\lambda} + \frac{\partial q}{\partial w}\dot{w} = 0,$$

from which the following optimal input dynamics can be computed:

$$\dot{u}^*(t) = -\left(\frac{\partial q}{\partial u}\right)^{-1}\left(\frac{\partial q}{\partial x}\dot{x} + \frac{\partial q}{\partial \lambda}\dot{\lambda} + \frac{\partial q}{\partial w}\dot{w}\right), \tag{2.32}$$

Therefore, the explicit minimization of the Hamiltonian can be replaced by (2.30) and (2.31), since $\frac{\partial q}{\partial u} = \frac{\partial^2 H}{\partial u^2}$, (2.26) guarantees that $\left(\frac{\partial q}{\partial u}\right)^{-1}$ is defined. A methodology to approximate $\dot{w}$ for the case when only $w(t)$ is available is given in Appendix A.2. Considering these new optimality conditions, EMS (2.20) can be solved via the following

BVP [53, 71]:

$$\dot{x}(t) = f(x(t), u^*(t), w(t), w(t)) \tag{2.33a}$$

$$\dot{\lambda}(t) = -\frac{\partial H}{\partial x}, \tag{2.33b}$$

$$\dot{u}^*(t) = -\left(\frac{\partial q}{\partial u}\right)^{-1}\left(\frac{\partial q}{\partial x}\dot{x} + \frac{\partial q}{\partial \lambda}\dot{\lambda} + \frac{\partial q}{\partial w}\dot{w}\right), \tag{2.33c}$$

$$q(0) = 0, \tag{2.33d}$$

$$\lambda_i(t_f) = 0, \forall x_i(t_f) \notin X(t_f) \tag{2.33e}$$

$$\text{state boundary constraints (2.18e)} - \text{(2.18f)}. \tag{2.33f}$$

In the following, the solution to BVP (2.33) will be denoted as $Y(t) \in \mathbb{R}^{2n+m}$. The dynamics of Y will be denoted as $F(Y, t)$. Note that the idea of computing higher order time derivatives of the Hamiltonian was also considered in [72]. There, it is presented an inversion approach that allows parameterizing an optimal control problem using only one higher-order unknown parameter. However, their inversion method requires having access to an explicit expression of the optimal control, which is not the case for the problem formulation considered in our contribution.

2.4.4 Numerical solution of the EMS

Whenever a state reaches its boundary, its corresponding co-state becomes discontinuous [73]. BVP solvers cannot easily handle such discontinuities straightforwardly. This section deals with the numerical aspects that need to be considered when computing the solution to BVP (2.33). The first two subsections discuss the *continuation procedure*, a numerical routine that breaks down the initial BVP into a sequence of several simpler sub-problems, starting from an unconstrained one down to a fully constrained one. Solutions to these sub-problems may temporarily exceed the state and control limits and as a result, the solutions may even lay outside the definition domain of $F(Y, t)$. To deal with this issue, the third subsection proposes to extend $F(Y, t)$ outside its domain of definition.

2.4.4.1 Continuation Procedure

The numerical success of the BVP solver depends on the initial guess solution being *close enough* to the unknown solution. The difficulty of generating a *good enough* initial guess is overcome by the implementation of a continuation or homotopy procedure [74, 75]. Before explaining the continuation procedure used for the considered BVP, let us briefly recall how a continuation procedure is implemented in general.

Let us consider a BVP that depends on a set of parameters ζ. The objective is to compute a solution for the parameter values ζ_N using a BVP solver. This is a difficult task in general. Let us use Y_i to denote the solution to the BVP for the set of parameters ζ_i, with $i \in \{1, 2, \ldots, N\}$. In the continuation procedure, a set of parameters ζ_0 is chosen such that Y_0 can be easily computed. Y_0 is used as an initial guess for Y_1, where ζ_1 is chosen such that its values are between ζ_0 and ζ_N but close enough to ζ_0 such that Y_0 is a good enough initial guess for Y_1. At each iteration i, with $i > 0$, Y_i is computed using the solution computed at the previous iteration, Y_{i-1}, as an initial guess. The values of ζ_i smoothly approach those of the original problem at each iteration. The algorithm converges when Y_N, the solution to the original BVP, is reached. The convergence and the computation time of the algorithm depend on the total number of iterations, N, and the update function applied to vary the parameters from ζ_0 to ζ_N. The general continuation procedure described in the present paragraph is summarized in Algorithm 2.

Algorithm 2 General continuation procedure

Inputs: ζ_0, Y_0, ζ_N, N
Outputs: Y_N
  for $i = 1$ ***to*** N **do**
    $\zeta_i \leftarrow \text{update}\,(\zeta_{i-1})$
    $Y_i \leftarrow \text{solve}\,(\zeta_i, Y_{i-1})$
  end for

2.4.4.2 Application to the considered problem

In order to solve BVP (2.33), first, an initial guess is generated and then two continuation procedures are used. In order to identify the parameters of each continuation procedure, the following notation is introduced: ζ_i^j denotes parameter values at iteration $i \in \{0, 1, \ldots, N\}$ of the continuation procedure described in step $j \in \{a, b, c\}$.

2.4.4.3 Step a: generation of an initial solution

The penalty pondering coefficient ε^a is initially set to a large value so the penalty functions are negligible. The initial co-states are selected such that strict convexity assumption (2.26) is satisfied. Failing to meet this assumption could lead to $\frac{\partial^2 H}{\partial u^2} = \frac{\partial q}{\partial u}$ equal to zero, rendering the optimal control dynamics, (2.33c), undefined. The initial values for the optimal control $u(0)$ are numerically computed by solving $q(0) = 0$. Given these initial conditions, a solution is numerically computed by integrating differential equations (2.33a) -(2.33c) using an ODE solver. This solution is denoted by $Y^a(t)$.

2.4.4.4 Step b: First continuation procedure

The purpose of the first continuation procedure is to bring the states and co-states to its prescribed final values $X(t_f)$ and $\lambda_i(t_f) = 0, \forall x_i(t_f) \notin X(t_f)$, respectively. The penalty pondering coefficient ε remains unchanged : $\varepsilon^b = \varepsilon^a$. The continuation procedure parameters are $\zeta^b = \left[x(t_f), \lambda(t_f)\right]^T$. ζ_0^b is set equal to the final conditions $\left[x^a(t_f), \lambda^a(t_f)\right]^T$ from the initial solution Y^a. ζ_N^b is set to $\left[X(t_f), \lambda_i(t_f) = 0\right]^T$ as defined in (2.33e) and (2.33f). The parameter update function is assumed linear, values of ζ_i^b are given by:

$$\zeta_i^b = \frac{\zeta_N^b - \zeta_0^b}{N^b} + \zeta_{i-1}^b, \tag{2.34}$$

Algorithm 3 First continuation procedure.

Inputs: $\zeta_0^b = \left[x^a(t_f), \lambda^a(t_f)\right]^T$, $Y_0^b = Y^a$, $\zeta_N^b = \left[X(t_f), \lambda_i(t_f) = 0\right]^T$, N^b;
Outputs: Y_N^b;
  for $i = 1$ ***to*** N^b **do**
    $\zeta_i^b \leftarrow \left(\zeta_N^b - \zeta_0^b\right)/N^b + \zeta_{i-1}^b$
    $Y_i^b \leftarrow \text{solve}\left(\zeta_i^b, Y_{i-1}^b\right)$
  end for

The output of the continuation procedure is the unconstrained (non-penalized) solution to EMS (2.18). The continuation procedure is summarized in Algorithm 3.

2.4.4.5 Step c: Second continuation procedure

The second continuation procedure activates the penalty functions by reducing the value of ε, thus $\zeta^c = \varepsilon$. ζ_0^c is set equal to the large value of ε used initially: $\zeta_0^c = \varepsilon^b = \varepsilon^a$. In order to obtain a solution that fulfills the constraints, a very small value of ε should be reached at the end of this continuation procedure : $\zeta_N^c \approx 0$. The values of ζ_i^c are chosen to be varied exponentially. The continuation procedure can be summarized in the following algorithm:

Algorithm 4 Second continuation procedure.

Inputs: ζ_0^c, $Y_0^c = Y_N^b$, $\zeta_N^c \approx 0$, N^c;
Outputs: Y_N^c;
  $\alpha \leftarrow \left(\ln(\zeta_N^c) - \ln(\zeta_0^c)\right)/N^c$
  for $i = 1$ ***to*** N^c **do**
    $\zeta_i^c \leftarrow e^{\alpha} \cdot \zeta_{i-1}^c$
    $Y_i^c \leftarrow \text{solve}\left(\zeta_i^c, Y_{i-1}^c\right)$
  end for

The output of the second continuation procedure is the solution to constrained (penalized) EMS (2.18). The general numerical procedure presented in this subsection is summarized in Fig. 2.1.

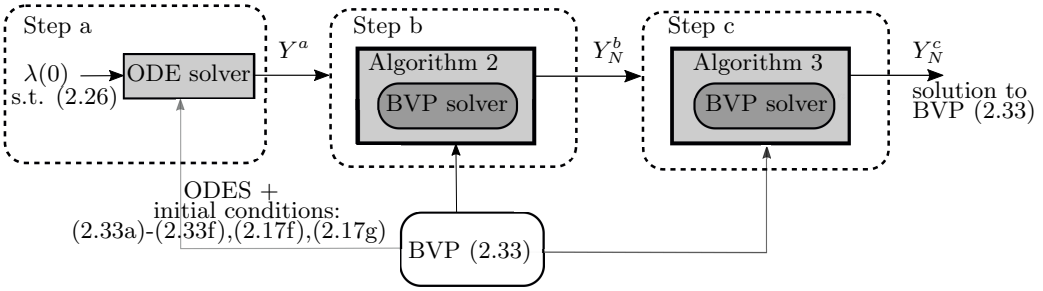

FIGURE 2.1: Overview of *Step a*, *Step b*, and *Step c*.

2.4.4.6 Function extension

We now consider the case where dynamics $F(Y,t) : \mathbb{U} \to R^{2n+m}$ in (2.33) have a definition domain such that $\mathbb{U} \neq R^{2n+m}$. For instance, it is frequently encountered that the state dynamics f contains a term $\sqrt{E^2 - 4R \cdot u}$ and therefore $\mathbb{U} = \left[-\infty, \frac{E^2}{4 \cdot R}\right] \times \mathbb{R}^{2n+m-1}$. Since the only constraint for the initial co-states, used to generate the initial solution in *Step a*, is to satisfy strict convexity assumption (2.26), the states may reach values outside the definition domain of F. As a consequence, *Step a* and *b* may not be feasible. Moreover, even in *Step c*, the BVP solver may require to evaluate $F(Y,t)$ outside its definition domain. To overcome the latter problems, $F(Y,t)$ is extended outside its definition domain and the resulting function is denoted by $F_{\text{ext}}(Y,t) : \mathbb{R}^{2n+m} \to \mathbb{R}^{2n+m}$. F and F_{ext} are identical for all $Y \in \mathbb{U}$. F_{ext} is obtained by replacing every scalar nonlinear term in F which is not defined for all $\mathbb{R}^{n_i}$, denoted as $h_i(y)$ with $y \in H_i \subset \mathbb{R}^{n_i}$, by a function extension based on the Taylor series, $g_i(y)$. Let us that all the h_i terms are C^∞. The Taylor series expansion of h_i around of $\tilde{y}$ is defined as follows:

$$\begin{aligned} h_i(y) =& h_i(\tilde{y}) + (y-\tilde{y})^T \nabla f_i(\tilde{y}) + \\ &+ \frac{1}{2}(y-\tilde{y})^T \nabla^2 f_i(\tilde{y})(y-\tilde{y}) + \dots \end{aligned}$$

With ∇h_i and $\nabla^2 h_i$ defined as the gradient and Hessian matrix of h_i, respectively. Given $\tilde{y} \in \partial H_i$, and $z \notin X_i$, the domain of h_i is extended outside H_i by the following function:

$$g_i(z) = h_i(\tilde{y}) + (z-\tilde{y})^T \nabla h_i(\tilde{y}) + \frac{1}{2}(z-\tilde{y})^T \nabla^2 h_i(\tilde{y})(z-\tilde{y}), \tag{2.35}$$

where $\tilde{y}$ is defined as the closest point on the boundary of H_i, ∂H_i, with respect to z.

Taylor-based function extension (2.35) can preserve the convexity properties of the original function and thus guarantee that the strict convexity assumption on the Hamiltonian, (2.26), which in turn guarantees that the solution remains unique and that optimal control dynamics (2.33c) is well defined.

2.5 Application 1: Series HEV with battery thermal dynamics

In this first application, the *penalty function and implicit Hamiltonian minimization approach* will be applied to compute the two-state (the battery state-of-energy and the battery temperature) single-input (the power generated by the APU) EMS under input and state constraints. The studied vehicle is a Series-HEV, shown in Fig. 2.2. We would like to study the effect that extreme cold conditions (-20 degrees Celsius) have on fuel consumption when battery thermal dynamics are considered in the EMS.

The driving mission used to model the power demand from the user is the Worldwide Light-vehicle Test Cycle Class 3 (WLTC-C3), and it is depicted in Fig. 2.3 (left). For the considered series hybrid vehicle, see Fig. 2.2, and the parameters of Table 2.2 the EMS input data is the power $w(t)$ (kW) required to propel the vehicle along the given driving cycle [17].

In the rest of this section, the offline-EMS will be defined in more detail for the considered series hybrid vehicle. However, it is worth noticing that the methodology presented in this work can be applied to many other hybrid vehicle topologies as well.

2.5.1 Modeling

Consider the HEV powertrain topology displayed in Fig. 2.2. The power required by the traction motor (TM) for propelling, $w(t) \in \mathbb{R}$, must be provided at each instant by the

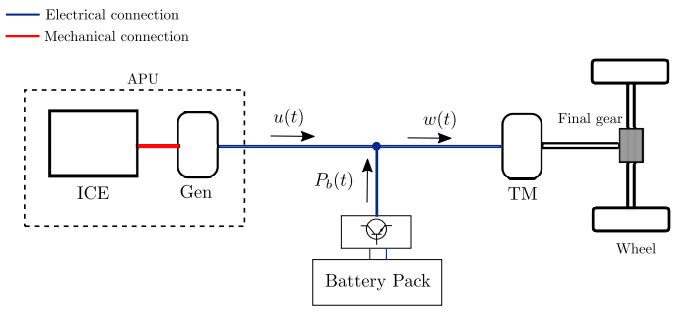

FIGURE 2.2: Diagram of the series-HEV powertrain.

auxiliary power unit (APU), $u(t) \in \mathbb{R}$, and/or the battery pack, $P_b(t) \in \mathbb{R}$. Moreover, the APU is subject to a on/off command signal, $\vartheta(t) \in \{0, 1\}$. The series topology imposes the following restriction among the power signals:

$$w(t) = \vartheta(t) \cdot u(t) + P_b(t). \tag{2.36}$$

The models required to compute $w(t)$, $P_b(t)$, and $u(t)$ are discussed in the following subsections. For the ease of readiness, in the following, the time dependence of the variables will be omitted when convenient.

2.5.1.1 Traction subsystem

The traction subsystem includes the vehicle model and transmission from the wheels to the TM. The corresponding model allows evaluating the energetic requirement of the vehicle. Given a velocity profile $v(t)$, the vehicle parameters, and assuming a flat road the torque $T_w(t)$ and the angular velocity at the wheels $\omega_w(t)$, required to complete the driving mission, are computed [17]:

$$T_w(t) = r_w \left(m_{eq} \cdot \frac{\mathrm{d}v(t)}{\mathrm{d}t} + m \cdot g \cdot c_r + \frac{1}{2} \rho_a \cdot A_s \cdot c_d \cdot v^2(t) \right), \tag{2.37}$$

$$\omega_w(t) = v(t)/r_w, \tag{2.38}$$

with c_r the tire rolling resistance (-), g the gravity acceleration $\left(\mathrm{kg} \cdot \mathrm{m/s^2}\right)$, ρ_a the air density $\left(\mathrm{kg/m^3}\right)$, A_s the vehicle frontal area $\left(\mathrm{m^2}\right)$, c_d the drag coefficient (-), γ the final gear ratio (-), r_w the radius of the wheels (m), m the vehicle mass (kg), and $m_{eq} = m + J_{tm}/\left(\gamma^2 r_w^2\right)$ the equivalent mass of the vehicle (kg). The vehicle is rear wheel driven (RWD): when braking, $T_w < 0$, only 40% of the torque is assumed to be provided by regenerative braking and the remaining 60% is assumed to be provided by the mechanical brakes. Indicated with $\mu_b(t)$ as a piecewise constant torque brake factor. A constant torque brake factor for regenerative braking is considered for the sake of simplicity. More advanced blending braking strategies may be applied, as in [76]. Finally, the TM torque and speed, denoted as T_{tm} and ω_{tm}, are derived:

$$T_{tm}(t) = \gamma \cdot \mu_b(t) \cdot T_w(t), \tag{2.39}$$

$$\mu_b(t) = \begin{cases} 0.4, & T_w(t) < 0 \\ 1, & \text{otherwise} \end{cases} \tag{2.40}$$

$$\omega_{tm}(t) = \omega_w(t)/\gamma. \tag{2.41}$$

At last, the power demand signal $w(t)$ is computed using the traction motor efficiency map η_{tm}:

$$w(t) = T_{tm}(t)\omega_{tm}(t)\eta_{tm}\left(T_{tm}(t), \omega_{tm}(t)\right)^{-sign(T_{tm}(t))} \tag{2.42}$$

Given the WLTC-C3 driving cycle, the power demand signal $w(t)$ is displayed in Fig. 2.3 (right).

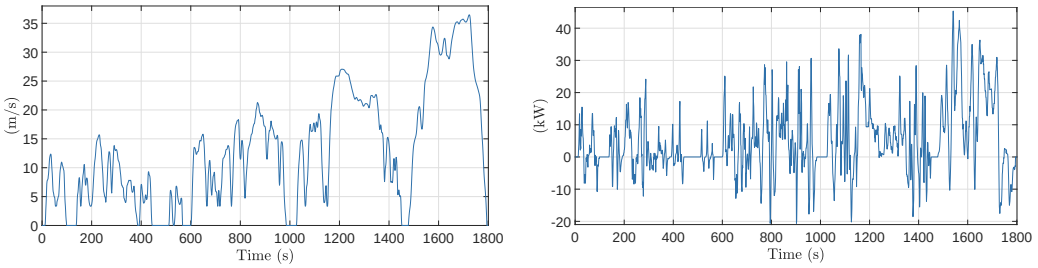

FIGURE 2.3: Worldwide Light-vehicle Test Cycle Class 3 (WLTC-C3) in m/s (left). Power demand signal $w(t)$ for the WLTC-C3 (right).

2.5.1.2 Battery Pack

The battery pack is connected to a DC/DC converter that fixes the DC bus voltage. Its losses are assumed to be negligible. The energetic behavior is modeled using both the state-of-energy dynamics given in [42] and a thermal model similar to the one found in [77]. They relate the battery power, $P_b(t)$, to the state-of-energy, denoted as $x_1(t)$, and the battery temperature, denoted as $x_2(t)$. The battery state-of-energy, $x_1(t)$, is derived from an equivalent electric circuit model. It consists of an open circuit voltage $U(x_1(t))$ in series with a temperature dependent resistance $R_b(x_2(t))$. The state-of-energy, $x_1(t)$, has the following dynamics:

$$\dot{x}_1(t) = \frac{1}{\bar{U} \cdot Q}\left[-P_b(t) - \frac{R_b(x_2(t))}{U^2(x_1(t))}P_b^2(t)\right], \tag{2.43}$$

with $\bar{U}$ the maximum open circuit voltage (V) and Q the charge capacity of the battery pack (Ah). The battery state-of-energy, $x_1(t)$, is constrained between $\underline{x}_1$ and $\bar{x}_1$

$$\underline{x}_1 \leq x_1(t) \leq \bar{x}_1. \tag{2.44}$$

Within the battery pack operating range (30%–90%), U is modeled as a linear function of x_1: $U(x_1) = a_{x_1} + b_{x_1}x_1$, derived from $LiFePO_4$ battery cell data found in [1], as shown in Fig. 2.4. The resistance R_b (Ω) is given by a linear function of x_2 (K).

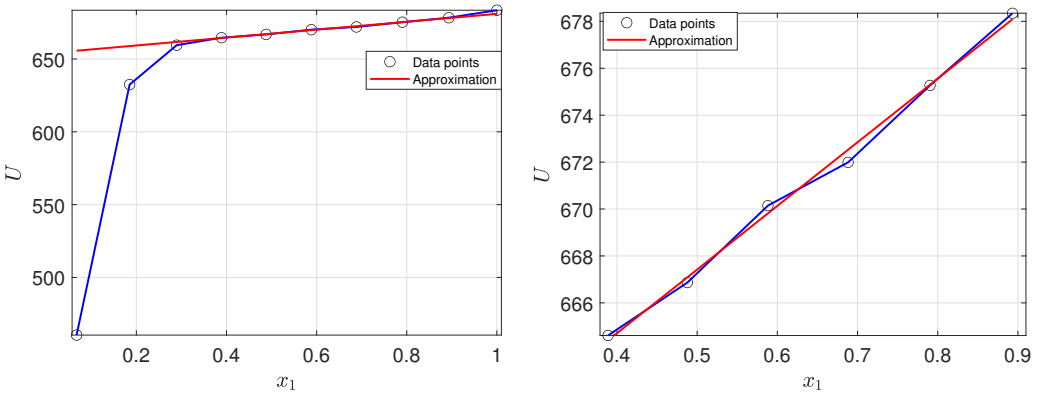

FIGURE 2.4: Open circuit voltage U as a function of x_1 derived from [1] (in blue) and the considered model $U(x_1) = a_{x_1} + b_{x_1} x_1$ (in red); plotted along the whole range of available data (left); plotted along the operating range (right). The parameters of $U(x_1)$ are $a_{x_1} = 27.14$ and $b_{x_1} = 653.85$.

The battery pack power $P_b(t)$ is constrained by the current limitations of the battery pack:

$$\underline{P}_b(R_b, U) \leq P_b(t) \leq \bar{P}_b(R_b, U), \tag{2.45}$$

with $\underline{P}_b = \underline{I} \cdot U - R_b \cdot \underline{I}^2$ and $\bar{P}_b = \bar{I} \cdot U - R_b \cdot \bar{I}^2$, $\underline{I}$ the minimum, and $\bar{I}$ the maximum battery pack current (A).

For the dynamics of x_2, the whole battery pack is modeled as a lumped mass and then the model is derived from a thermal energy balance equation [42, 77–79]:

$$\dot{x}_2(t) = \frac{1}{C_b}\left[h \cdot (T_\infty - x_2(t)) + \frac{R_b(x_2(t))}{U^2(x_1(t))} P_b^2(t)\right] \tag{2.46}$$

with C_b the heat capacity of the battery pack (kJ/K), T_∞ the ambient temperature (K), and h the heat transfer coefficient between the battery pack and its surroundings (W/K). The term depending on P_b stands for the heat dissipated by the battery resistance R_b whose dependency on x_2 has been derived from [1]. The battery resistance increases for low temperatures, thus reducing both the battery pack efficiency and the maximum power $\bar{P}_b$.

2.5.1.3 Auxiliary Power Unit

The APU consists of one ICE coupled with one generator (Gen) to produce electrical energy using fuel. The APU instantaneous fuel consumption, $\dot{m}_f(t)$ (g/s), required to generate electric power $u(t)$ (W), is estimated by the following quadratic function [42, 80]:

$$\dot{m}_f\left(u(t)\right) = a + b \cdot u(t) + c \cdot u^2(t). \tag{2.47}$$

The data used to compute the parameters of (2.47) is given in Appendix A.3. The criterion to be minimized by the EMS is the total fuel consumption:

$$J = \int_0^{t_f} \left[\dot{m}_f\left(u(t)\right)\vartheta(t) + d\cdot\left(1-\vartheta(t)\right)u^2(t)\right]\mathrm{d}t, \tag{2.48}$$

where t_f stands for the duration of the driving cycle and d is a conversion factor $\left(\frac{\mathrm{g}}{(\mathrm{kW})^2\cdot\mathrm{s}}\right)$. The additional term $(1-\vartheta)\cdot u^2$ allows enforcing $u=0$, whenever $\vartheta=0$ [53].

Recall that optimizing the binary variable ϑ may lead to theoretical difficulties, such as singular controls [49] and non-unique optimal solutions. As stated in Section 2.4.1, in order to focus on the state constraints handling, the binary signal ϑ is assumed to be fixed beforehand as a function of $w(t)$. For instance, it can be computed using a set of empirical rules according to the power demand $w(t)$. The power produced by the APU is constrained by the physical limits of its components:

$$0 \leq u(t) \leq \bar{u}, \tag{2.49}$$

yet also by the limits of other components on the powertrain via (2.36):

$$w(t) - \bar{P}_b(t) \leq u(t) \leq w(t) - \underline{P}_b(t). \tag{2.50}$$

Constraints (2.49) and (2.50) can be combined together:

$$\begin{aligned} &\underline{u}'(t) \leq u(t) \leq \bar{u}'(t), \\ &\underline{u}'(t) = \max\left[0, w(t) - \bar{P}_b\right], \\ &\bar{u}'(t) = \min\left[\bar{u}, w(t) - \underline{P}_b\right]. \end{aligned} \tag{2.51}$$

2.5.2 Problem statement

At last, the EMS can be cast as follows:

$$\min J(u) = \int_0^{t_f} \left[\vartheta \cdot \left(a + b \cdot u + c \cdot u^2\right) + d \cdot (1 - \vartheta) \cdot u^2\right] \mathrm{d}t, \tag{2.52a}$$

subject to:

$$\dot{x}_1(t) = \frac{1}{\bar{U} \cdot Q} \left[-(w - \vartheta u) - \frac{R_b(x_2)}{U^2(x_1)} (w - \vartheta u)^2\right], \tag{2.52b}$$

$$\dot{x}_2(t) = \frac{1}{C_b} \left[h \cdot (T_\infty - x_2) + \frac{R_b(x_2)}{U^2(x_1)} (w - \vartheta u)^2\right], \tag{2.52c}$$

$$\underline{u}'(t) \leq u(t) \leq \bar{u}'(t), \tag{2.52d}$$

$$\underline{u}'(t) = \max\left[0, w(t) - \bar{P}_b(t)\right],$$

$$\bar{u}'(t) = \min\left[\bar{u}, w(t) - \underline{P}_b(t)\right].$$

$$\underline{x}_1 \leq x_1(t) \leq \bar{x}_1, \tag{2.52e}$$

$$x_1(0) = x_{1,0}, \tag{2.52f}$$

$$x_2(0) = x_{2,0}, \tag{2.52g}$$

$$x_1(t_f) = x_{1,f}. \tag{2.52h}$$

The final condition $x_1(t_f)$ allows to guarantee that a certain amount of energy will remain in the battery at the end of the driving cycle. The final state-of-energy $x_1(t_f)$ is often assumed to be equal to $x_1(0)$ to allow a fair comparison with respect to the fuel consumption of conventional vehicles.

The problem statement above is a state and input constrained formulation of the EMS. As it accounts for the battery thermal modeling, its solution allows investigating the effect that a battery operating under *low-temperature* has on fuel consumption.

2.5.3 Solution

2.5.3.1 Penalty functions

Path constraint (2.52e) and input constraint (2.52d) are relaxed by adding $\frac{1}{\varepsilon}\left(\tilde{P}_u + P_x\right)$ to cost functional (2.52a)

$$\min \hat{J}(u) = \int_0^{t_f} \left[\vartheta \cdot \dot{m}_f(u) + d \cdot (1 - \vartheta) \cdot u^2 + \frac{1}{\varepsilon}\left(\tilde{P}_u + P_x\right)\right] \mathrm{d}t, \tag{2.53}$$

with:

$$P_x = P(x) = \begin{cases} (\underline{x} - x)^2, & x \leq \underline{x} \\ (x - \bar{x})^2, & x \geq \bar{x} \\ 0, & \text{otherwise,} \end{cases} \tag{2.54}$$

and $\tilde{P}_u = \phi \cdot P_u$, where

$$P_u = P(u) = \begin{cases} (\underline{u} - u)^2, & u \leq \underline{u} \\ (u - \bar{u})^2, & u \geq \bar{u} \\ 0, & \text{otherwise,} \end{cases} \tag{2.55}$$

and where $\phi = (1/\bar{u})^2$ is meant to scale $\tilde{P}_u$ down to the range of values of P_x.

2.5.3.2 Implicit Hamiltonian minimization

Considering optimality conditions (2.33c)-(2.33d) and cost functional, (2.52) can be solved via the following BVP:

$$\dot{x}_1(t) = \frac{1}{\bar{U} \cdot Q} \left[-(w - \vartheta \cdot u^*) - \frac{R_b(x_2)}{U^2(x_1)} (w - \vartheta \cdot u^*)^2 \right], \tag{2.56a}$$

$$\dot{x}_2(t) = \frac{1}{C_b} \left[h \cdot (T_\infty - x_2) + \frac{R_b(x_2)}{U^2(x_1)} (w - \vartheta \cdot u^*)^2 \right], \tag{2.56b}$$

$$\dot{\lambda}_1(t) = -\frac{1}{\varepsilon} \frac{\partial P_x}{\partial x_1}, \tag{2.56c}$$

$$\dot{\lambda}_2(t) = -\lambda_1 \frac{\partial \dot{x}_1}{\partial x_2} - \lambda_2 \frac{\partial \dot{x}_2}{\partial x_2}, \tag{2.56d}$$

$$\dot{u}^*(t) = -\left(\frac{\partial q}{\partial u} \right)^{-1} \left(\frac{\partial q}{\partial x_1} \dot{x}_1 + \frac{\partial q}{\partial x_2} \dot{x}_2 + \frac{\partial q}{\partial \lambda_1} \dot{\lambda}_1 + \frac{\partial q}{\partial \lambda_2} \dot{\lambda}_2 + \frac{\partial q}{\partial w} \dot{w} + \frac{\partial q}{\partial \vartheta} \dot{\vartheta} \right), \tag{2.56e}$$

$$q(0) = 0, \tag{2.56f}$$

$$\lambda_2(t_f) = 0, \tag{2.56g}$$

$$\text{state boundary constraints (2.52f)} - \text{(2.52h)}, \tag{2.56h}$$

The solution to (2.56) is denoted as $Y(t) = \left[x_1(t), x_2(t), \lambda_1(t), \lambda_2(t), u^*(t) \right]^T$. The dynamics of Y is denoted as $F(Y, t)$.

2.5.3.3 Function extension

Dynamics $F(Y, t)$ is not defined for open circuit voltage $U(x_1) = a_{x_1} x_1 + b_{x1} = 0$ due to the presence of the term $1/U(x_1)$ in (2.56a) and (2.56b). $F(Y, t)$ is replaced by

$F_{\text{ext}}(Y,t) \in \mathbb{R}^5$ via (2.35). Namely, F_{ext} is obtained by replacing $f(x_1) = 1/U(x_1) : (-a_{x_1}/b_{x_1}, +\infty] \to \mathbb{R}^+$ by $f_{\text{ext}}(x_1 \,|\, \tilde{x}_1) : \mathbb{R} \to \mathbb{R}^+$, with:

$$f_{\text{ext}}(x_1 \,|\, \tilde{x}_1) = \begin{cases} 1/U(x_1), & \text{if } x_1 \geq \tilde{x}_1 \\ g(x_1), & \text{otherwise} \end{cases} \tag{2.57}$$

$$\begin{aligned} g(x_1) =& 1/U(\tilde{x}_1) + (x_1 - \tilde{x}_1)\frac{\mathrm{d}\,(1/U(x_1))}{\mathrm{d}x_1} + \\ & \frac{1}{2}(x_1 - \tilde{x}_1)^2 \frac{\mathrm{d}^2\,(1/U(x_1))}{\mathrm{d}x_1^2}, \end{aligned} \tag{2.58}$$

where $\tilde{x}_1$ is a scalar to be chosen from the interval $(-a_{x_1}/b_{x_1}, \underline{x}_1]$.

In this case, the Taylor-based function extension preserves the convexity properties of the original function, thus, preserving strict convexity assumption (2.26).

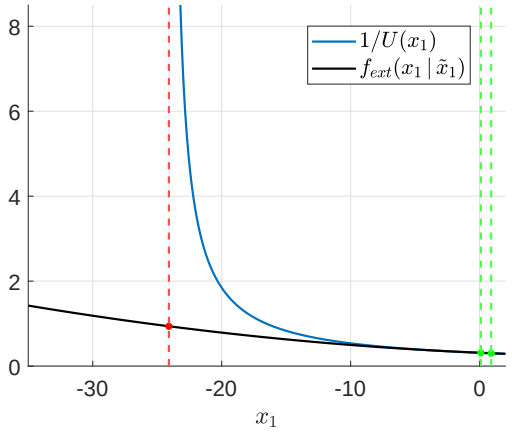

FIGURE 2.5: $1/U(x_1)$ (blue line), its function extension $f_{ext}(x_1 \,|\, \tilde{x}_1)$ (black line), the limit of the definition domain of $1/U(x_1)$: $x_1 = -a_{x_1}/b_{x_1}$ (red dotted line), and $\tilde{x}_1 = \underline{x}_1 = 0.1$ (green dotted line).

2.5.4 Numerical Results

Considering the vehicle parameters contained in Table 2.2, the offline-EMS is solved under *low-temperature* and *warm* operation conditions in order to study the effect that battery temperature has on fuel consumption.

2.5.5 Low-temperature operation

The *low-temperature* operation is defined here as starting the vehicle with $T_\infty = 253.15$ K (-20 °C), where T_∞ is assumed to remain constant along the entire driving cycle. At the beginning of the driving cycle, the following assumption holds: $x_2 = T_\infty$. Considering the WLTC-C3 driving cycle, the offline-EMS defined in (2.52) is solved via the equivalent

BVP (2.56) using a collocation solver [70] and the numerical procedure and function extension described in Section 2.4.4.

First, the initial guess Y^a is generated as described in *Step a* using $\lambda(0) = \begin{bmatrix} 1.4 \cdot 10^5 & 1.45 \cdot 10^5 \end{bmatrix}^T$ and the initial penalty pondering coefficient $\varepsilon^a = 1 \cdot 10^{12}$. The obtained initial solution Y^a is depicted in Fig. 2.6. The state-of-energy reaches negative values, showing that the initial guess does not necessarily have a physical meaning.

The final conditions from Y^a, $\begin{bmatrix} x_1^a(t_f), \lambda_2^a(t_f) \end{bmatrix}^T = \begin{bmatrix} -7.3, 5.32 \cdot 10^6 \end{bmatrix}^T$, are applied at the beginning of *Step b*: $\zeta_0^b = \begin{bmatrix} x_1^a(t_f), \lambda_2^a(t_f) \end{bmatrix}^T$. *Step b* allows computing a solution that reaches the expected final state-of-energy and the necessary final condition for the second co-state: $\zeta_f^b = [x_1(t_f), 0]^T$. This procedure is depicted in Fig. 2.7. Its output Y_N^b, shown in Fig. 2.8, is the solution to EMS (2.52) without constraints, since the penalty functions are negligible: $\varepsilon^b = \varepsilon^a = 1 \cdot 10^{12}$.

Parameter	Value	Units
M_{eq}	2166	kg
A_s	1.98	m^2
c_d	0.32	-
c_r	0.01	-
γ	4.2	-
r_w	0.26	m
g	9.81	$\mathrm{kg{\cdot}m/s^2}$
J_{tm}	0.045	$\mathrm{kg{\cdot}m^2}$
$\underline{I}$	-40	A
$\bar{I}$	40	A
a_{x_1}	653.85	V
b_{x_1}	27.14	V
Q	1800	A·s
h	4.343	W/K
C_b	142.56	kJ/K
a	0.2924	g/s
b	0.0834	$\frac{\mathrm{g}}{\mathrm{kW{\cdot}s}}$
c	0.0055	$\frac{\mathrm{g}}{(\mathrm{kW})^2{\cdot}\mathrm{s}}$
d	1	$\frac{\mathrm{g}}{(\mathrm{kW})^2{\cdot}\mathrm{s}}$
$\bar{u}$	17.5	kW

TABLE 2.2: Parameters considered in the numerical experiments of application 1.

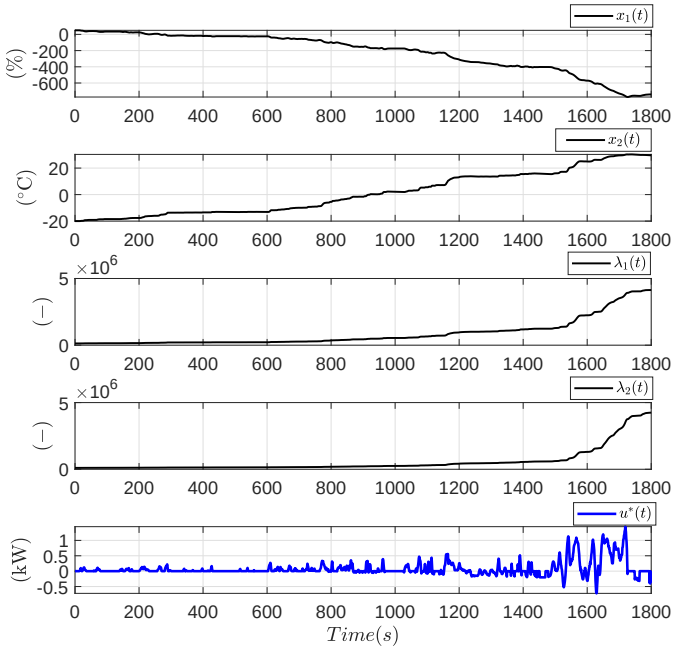

FIGURE 2.6: Initial guess Y^a generated in *Step a* for the WLTC-C3 driving cycle.

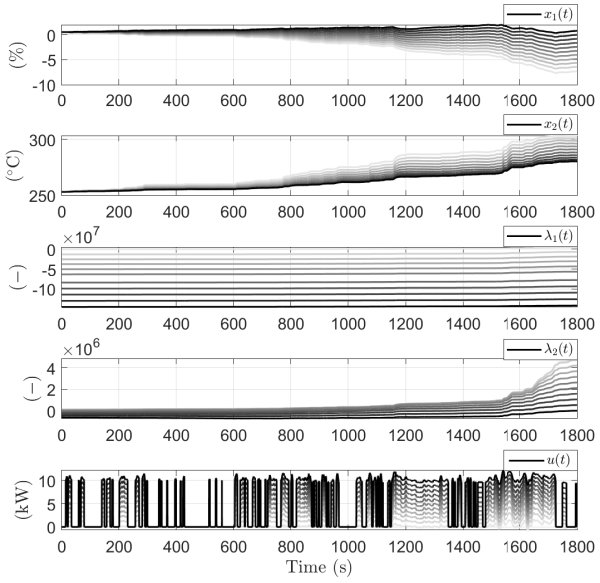

FIGURE 2.7: Set of solutions computed in *Step b* for the *low-temperature* operation and the WLTC-C3 driving cycle: the light gray trajectory denotes the first solution of the continuation procedure. As the trajectories become darker, they approach the final boundary conditions. The final trajectory of the procedure is displayed in black.

The output of *Step b*, Y_N^b, is fed into *Step c*: $Y_0^c = Y_N^b$. *Step c* is used to activate the penalty functions. The initial penalty pondering coefficient is set to the same value of *Step b*: $\zeta_0^c = \varepsilon_0^c = \varepsilon^b = 1 \cdot 10^{12}$. The final penalty pondering coefficient is set to a small positive value: $\varepsilon_N^c = 1 \cdot 10^{-9}$. This procedure is depicted in Fig. 2.9. The output of *Step c*, Y_N^c, is the solution to constrained EMS (2.52) and is shown in Fig. 2.10. It allows

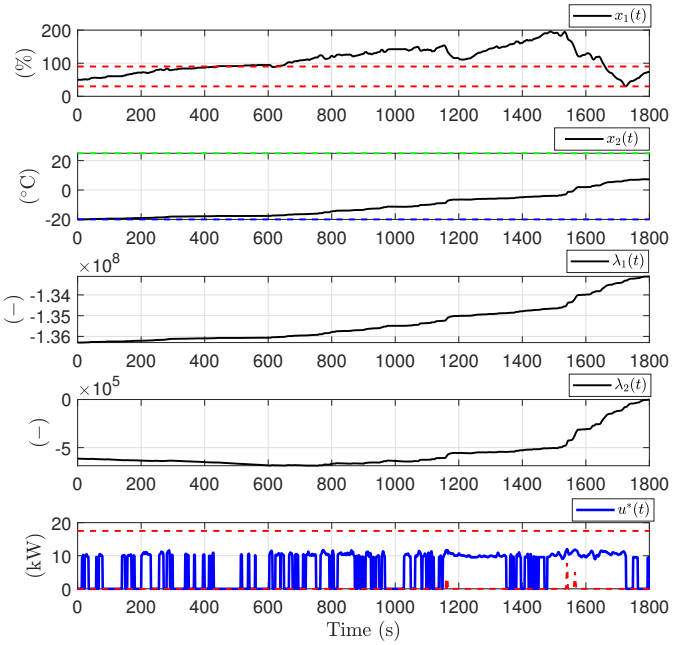

FIGURE 2.8: Unconstrained solution to (2.52) for the *low-temperature* operation and the WLTC-C3 driving cycle. The fuel consumption is 9.53 l/100 km. The red dashed lines at the top and bottom subfigures represent the bounds on the state-of-energy and the control input, (2.52e) and (2.52d), respectively.

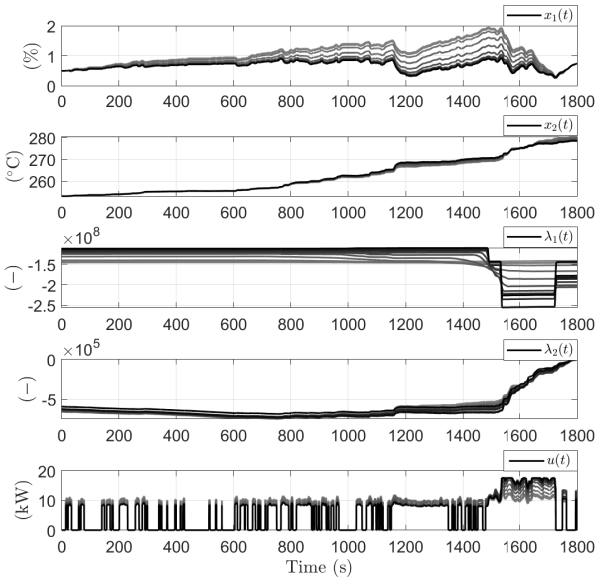

FIGURE 2.9: Set of solutions computed in *Step c* for the *low-temperature* operation and the WLTC-C3 driving cycle: the light gray trajectory denotes the first solution of the continuation procedure. As the trajectories become darker, they approach the constrained solution. The final trajectory of the procedure is displayed in black.

computing the fuel consumption for the *low-temperature* operation : 9.85 l/100km.

The constrained solution for the EMS, Fig. 2.10, shows a discontinuity phenomenon

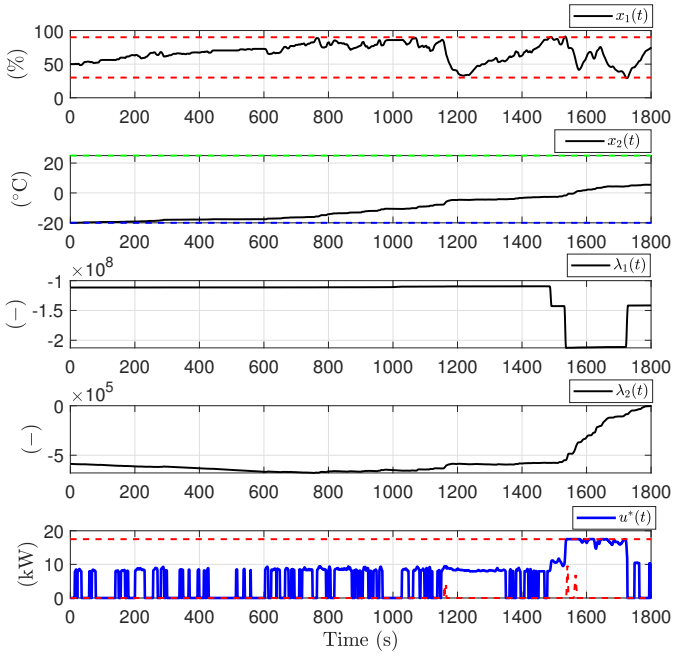

FIGURE 2.10: Constrained solution to (2.52) for *low-temperature* operation and the WLTC-C3 driving cycle. The fuel consumption is 9.85 l/100 km. The red dashed lines at the top and bottom subfigures represent the bounds on the state-of-energy and the control input, (2.52e) and (2.52d), respectively.

for $\lambda_1(t)$. This phenomenon is to be expected, whenever a state makes contact with its bounds [73]. It is worth noticing that the procedure proposed in this work does not require any *a priori* knowledge about these discontinuities.

2.5.6 Warm versus low-temperature operation

Here, the fuel consumption of the *low-temperature* operation will be compared with an ideal *warm* operation. The *warm* operation is defined as $T_\infty = 298.15$ K (25 °C), with T_∞ assumed constant along the entire driving cycle. At the beginning of the driving cycle $x_2 = T_\infty$ holds. Moreover, in the *warm operation*, the dynamics of the battery temperature is considered to be equal to zero; on the assumption that a cooling system is in place to keep $x_2 \approx 298.15$ K (25 °C) along the entire driving cycle. The offline-EMS is solved under *warm* operation conditions using the same vehicle parameters of the *low-temperature* operation. The fuel consumption for each operation is shown in Table 2.3. The *low-temperature* operation increases the fuel consumption with respect to the ideal *warm* operation in a 4.01%.

Operation	Fuel consumption (WLTC-C3)	Difference
Warm	9.47 l/100km	-
Low-temperature	9.85 l/100km	+4.01 %

TABLE 2.3: Fuel consumption results for each operating condition.

2.5.7 Solution via DP

The optimal energy management for the low-temperature operation will be solved again using DP. The objective is to validate the optimality of the proposed approach and to benchmark its computational efficiency. As mentioned in Section 2.2.1, DP has been widely used to solve the EMS in the literature of hybrid electric vehicles [35][36]. Its advantages are that it can solve the EMS with mixed input-state constraints with a guarantee of global optimality. Its main drawback is that it has an exponential growth of space and computational complexity with respect to the number of states and inputs, denoted as the *curse of dimensionality* [34]. For this reason, its use is limited to EMS formulations with one [35] or two states [37]. The DP algorithm is implemented using the Matlab code from [81], together with the iterative approach described in [82]. The solution has been computed using the parameters presented in Table 2.2. The results of the DP solution to (2.52) are displayed in Fig. 2.11 along with the solution computed with the proposed approach. The fuel consumption and computation times are compared in Table 2.4. The proposed approach is 46 times faster than DP but obtains +0.4% more fuel consumption as well. The small difference in fuel consumption can be due to the limited accuracy that DP posses as a consequence of the quantization of all variables and the Euler integration scheme in which it relies on.

Method	Fuel consumption (WLTC-C3)	Computation time (hours)
DP	9.81 l/100km (100%)	17.186 (≈4600%)
Implicit Hamiltonian minimization	9.85 l/100km (100.4%)	0.366 (100%)

TABLE 2.4: Fuel consumption and computation time for DP and the proposed implicit Hamiltonian minimization under *low-temperature* conditions. The algorithms were implemented in a workstation with 64 GB of RAM and a processor Intel(R) Core(TM) i7-9800X CPU @3.80GHz with 8 cores.

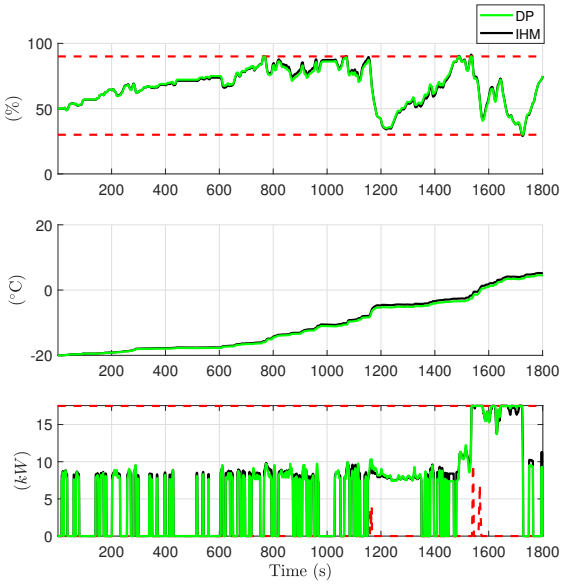

FIGURE 2.11: Solution to (2.52) for the *low-temperature* operation and the WLTC-C3 driving cycle with DP (green solid line) and the proposed implicit Hamiltonian minimization (black solid line). The red dashed lines at the top and bottom subfigures represent the bounds on the state-of-energy and the control input, (2.52e) and (2.52d), respectively.

2.6 Application 2: Dual Series HEV

In this application, the energy management is solved for an HEV equipped with a battery pack and a supercapacitor in a series configuration, see Fig. 2.12. The problem formulation has two states (the battery state-of-charge and the capacitor voltage), and two inputs (the current going through the battery and the current going through the supercapacitor). Both states are subject to path constraints. Both inputs are constrained as well. As in the previous application, the solution will be bench-marked and validated with the help of iterative-dynamic programming. The solution provided by our contribution is once more able to solve the problem significantly faster than the I-DP approach.

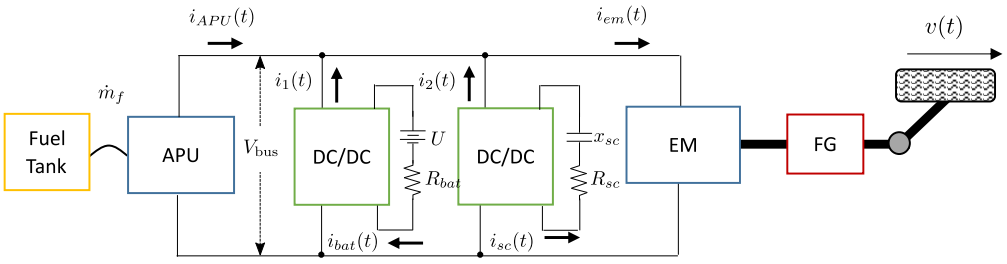

FIGURE 2.12: Dual Series HEV diagram.

2.6.1 Modeling

Consider the HEV powertrain topology displayed in Fig. 2.12. The power required by the traction motor (TM) for propelling, $w(t) \in \mathbb{R}$, must be provided at each instant by the auxiliary power unit (APU), $u_1(t) \in \mathbb{R}$, and/or the battery pack, $P_b(t) \in \mathbb{R}$, and/or the supercapacitor. The series topology operates with a constant DC voltage V_{bus} and imposes the following restriction among the power signals:

$$w(t) = u_1(t) + P_{sc}(t) + P_b(t). \tag{2.59}$$

The models required to compute $w(t)$, $P_{sc}(t)$, $P_b(t)$ and $u_1(t)$ are discussed in the following subsections. For the ease of readiness, in the following, the time dependence of the variables will be omitted when convenient.

2.6.1.1 Traction subsystem

The traction subsystem includes the vehicle model and transmission from the wheels to the TM. The corresponding model allows evaluating the energetic requirement of the vehicle. Given a velocity profile $v(t)$, the vehicle parameters, and assuming a flat road, the torque $T_w(t)$ and the angular velocity at the wheels $\omega_w(t)$, required to complete the driving mission, are computed [17]:

$$T_w(t) = r_w \left(m_{eq} \cdot \frac{\mathrm{d}v(t)}{\mathrm{d}t} + m \cdot g \cdot c_r + \frac{1}{2} \rho_a \cdot A_s \cdot c_d \cdot v^2(t) \right), \tag{2.60}$$

$$\omega_w(t) = v(t)/r_w, \tag{2.61}$$

with c_r the tire rolling resistance (-), g the gravity acceleration $\left(\mathrm{kg} \cdot \mathrm{m/s^2}\right)$, ρ_a the air density $\left(\mathrm{kg/m^3}\right)$, A_s the vehicle frontal area $\left(\mathrm{m^2}\right)$, c_d the drag coefficient (-), γ the final gear ratio (-), r_w the radius of the wheels (m), m the vehicle mass (kg), and $m_{eq} = m + J_{tm}/\left(\gamma^2 r_w^2\right)$ the equivalent mass of the vehicle (kg). The vehicle is rear wheel driven (RWD): when braking, $T_w < 0$, only 40% of the torque is assumed to be provided by regenerative braking and the remaining 60% is assumed to be provided by the mechanical brakes. Indicated with $\mu_b(t)$ as a piecewise constant torque brake factor. A constant torque brake factor for regenerative braking is considered for the sake of

simplicity. Finally, the TM torque and speed, denoted as T_{tm} and ω_{tm}, are derived:

$$T_{tm}(t) = \gamma \cdot \mu_b\,(t) \cdot T_w(t), \tag{2.62}$$

$$\mu_b(t) = \begin{cases} 0.4, & T_w(t) < 0 \\ 1, & \text{otherwise} \end{cases} \tag{2.63}$$

$$\omega_{tm}(t) = \omega_w(t)/\gamma. \tag{2.64}$$

At last, the power demand signal $w(t)$ is computed using the traction motor efficiency map η_{tm}:

$$w(t) = T_{tm}(t)\omega_{tm}(t)\eta_{tm}\left(T_{tm}(t), \omega_{tm}(t)\right)^{-sign(T_{tm}(t))} \tag{2.65}$$

Given the WLTC-C3 driving cycle, the power demand signal $w(t)$ is displayed in Fig. 2.3 (right).

2.6.1.2 Battery Pack

The battery pack is connected to a DC/DC converter that fixes the DC bus voltage V_{bus}. Its losses are assumed to be negligible. The energetic behavior is modeled using a single dynamics model: it relates the battery power, $P_b(t)$, to the state-of-charge, denoted as $x_1(t)$. It is derived from an equivalent electric circuit model. It consists of a fixed open circuit voltage U in series with a fixed resistance R_b. The state-of-charge, $x_1(t)$, has the following dynamics:

$$\dot{x}_1(t) = \frac{-U + \sqrt{U^2 - 4 \cdot R_b \cdot V_{bus} \cdot i_1(t)}}{2 \cdot Q\, R_b}, \tag{2.66}$$

with Q the charge capacity of the battery pack (As). The battery state-of-charge, $x_1(t)$, is constrained between $\underline{x}_1$ and $\bar{x}_1$

$$\underline{x}_1 \leq x_1(t) \leq \bar{x}_1, \tag{2.67}$$

likewise, i_1 is constrained as follows:

$$\underline{i}_1 \leq i_1(t) \leq \bar{i}_1. \tag{2.68}$$

2.6.1.3 Supercapacitor Pack

Assuming a DC/DC converter with negligible losses, the power at the SC, P_{sc}, can be described as:

$$P_{sc} = i_1(t) \cdot V_{bus} = i_{sc} \cdot (x_{sc}(t) - R_{sc} \cdot i_{sc}(t)) = -R_{sc} \cdot i_{sc}^2(t) + i_{sc} \cdot x_{sc},$$

then, we can obtain the expression for the current from $-R_{sc} \cdot i_{sc}^2(t) + i_{sc} \cdot x_{sc} - i_1(t) \cdot V_{bus} = 0$:

$$i_{sc}(t) = \frac{-x_{sc} \pm \sqrt{x_{sc}^2 - 4 \cdot R \cdot i_1(t) \cdot V_{bus}}}{-2 \cdot R_{sc}} = \frac{-x_{sc} \pm \sqrt{x_{sc}^2 - 4 \cdot R \cdot i_1(t) \cdot V_{bus}}}{-2 \cdot R_{sc}}. \quad (2.69)$$

Defining $x_2 = x_{sc}$ and considering that voltage and current in a capacitor obey $i_{sc}(t) = C \cdot \frac{\mathrm{d}x_{sc}}{\mathrm{d}t}$, the voltage dynamics of the SC are given as follows:

$$\dot{x}_2(t) = -\frac{1}{C} i_{sc}(t) = \frac{-x_2 + \sqrt{x_2^2 - 4 \cdot R \cdot i_2(t) \cdot V_{bus}}}{2 \cdot C \cdot R_{sc}}. \quad (2.70)$$

x_2 is constrained between $\underline{x}_2 \leq x_2 \leq \bar{x}_2$:

$$\underline{x}_2 \leq x_2(t) \leq \bar{x}_2, \quad (2.71)$$

likewise, i_2 is constrained as follows:

$$\underline{i}_2 \leq i_2(t) \leq \bar{i}_2. \quad (2.72)$$

2.6.1.4 Auxiliary Power Unit

The APU consists of one ICE coupled with one generator (Gen) to produce electrical energy using fuel. The APU instantaneous fuel consumption, $\dot{m}_f(t)$ (g/s), required to generate a given electric power $u_1(t)$ (W), is estimated by the following quadratic function [42, 80]:

$$\dot{m}_f(u_1(t)) = a + b \cdot u_1(t) + c \cdot u_1^2(t). \quad (2.73)$$

The data used to compute the parameters of (2.47) is given in Appendix A.3. The criterion to be minimized by the EMS is the total fuel consumption:

$$J = \int_0^{t_f} \dot{m}_f(u_1(t))\, \mathrm{d}t, \quad (2.74)$$

where t_f stands for the duration of the driving cycle. The power produced by the APU is constrained by the physical limits of its components:

$$0 \leq u_1(t) \leq \bar{u}_1, \tag{2.75}$$

and by (2.36):

$$w(t) - \bar{P}_b - \bar{P}_b \leq u_1(t) \leq w(t) - \underline{P}_b - \underline{P}_{sc}, \tag{2.76}$$

with $\underline{P}_b = V_{bus} \cdot \underline{i}_1$, $\underline{P}_{sc} = V_{bus} \cdot \underline{i}_2$, $\bar{P}_b = V_{bus} \cdot \underline{i}_1$, and $\bar{P}_{sc} = V_{bus} \cdot \bar{i}_2$. These constraints can be combined together as follows:

$$\begin{aligned} &\underline{u}'_1(t) \leq u_1(t) \leq \bar{u}'(t), \\ &\underline{u}'_1(t) = \max\left[0, w(t) - V_{bus} \cdot \bar{i}_1 - V_{bus} \cdot \bar{i}_2\right], \\ &\bar{u}'_1(t) = \min\left[\bar{u}_1, w(t) - V_{bus} \cdot \underline{i}_1 - V_{bus} \cdot \underline{i}_2\right]. \end{aligned} \tag{2.77}$$

2.6.2 Problem statement

Defining $u_2 = i_2$ and considering solving (2.59) for P_b, the EMS can be cast as follows:

$$\min J(u_1) = \int_0^{t_f} \left[a + b \cdot u_1 + c \cdot u_1^2\right] \, \mathrm{d}t, \tag{2.78a}$$

subject to:

$$\dot{x}_1(t) = \frac{-U + \sqrt{U^2 - 4 \cdot R_b \cdot (w - u_1 - V_{bus} \cdot u_2)}}{2 \cdot Q \, R_b}, \tag{2.78b}$$

$$\dot{x}_2(t) = \frac{-x_2 + \sqrt{x_2^2 - 4 \cdot R_{sc} \cdot V_{bus} \cdot u_2}}{2 \cdot C \cdot R_{sc}}, \tag{2.78c}$$

$$\underline{u}'_1(t) \leq u_1(t) \leq \bar{u}'_1(t), \tag{2.78d}$$

$$\begin{aligned} &\underline{u}'_1(t) = \max\left[0, w(t) - V_{bus} \cdot \bar{i}_1 - V_{bus} \cdot \bar{u}_2\right], \\ &\bar{u}'_1(t) = \min\left[\bar{u}_1, w(t) - V_{bus} \cdot \underline{i}_1 - V_{bus} \cdot \underline{u}_2\right], \end{aligned}$$

$$\underline{u}_2 \leq u_2(t) \leq \bar{u}_2, \tag{2.78e}$$

$$\underline{x}_1 \leq x_1(t) \leq \bar{x}_1, \tag{2.78f}$$

$$\underline{x}_2 \leq x_2(t) \leq \bar{x}_2, \tag{2.78g}$$

$$x_1(0) = x_{1,0}, \tag{2.78h}$$

$$x_2(0) = x_{2,0}, \tag{2.78i}$$

$$x_1(t_f) = x_{1,f}. \tag{2.78j}$$

$$x_2(t_f) = x_{2,f}. \tag{2.78k}$$

The final condition $x_1(t_f)$ allows to guarantee that a certain amount of energy will remain in the battery at the end of the driving cycle. The final state-of-charge $x_1(t_f)$ is

often assumed to be equal to $x_1(0)$ to allow a fair comparison with respect to the fuel consumption of conventional vehicles.

The problem statement above is a state and input constrained formulation of the EMS.

2.6.3 Solution

2.6.3.1 Penalty functions

Path constraints (2.78f)-(2.78g) and input constraints are relaxed by adding $\frac{1}{\varepsilon}\left(\tilde{P}_{u_1}+\tilde{P}_{u_2}+P_{x_1}+\tilde{P}_{x_2}\right)$ to cost functional (2.78a)

$$\min \hat{J}(u)=\int_0^{t_f}\left[\dot{m}_f+\frac{1}{\varepsilon}\left(\tilde{P}_{u_1}+\tilde{P}_{u_2}+P_{x_1}+\tilde{P}_{x_2}\right)\right]\mathrm{d}t, \tag{2.79}$$

with:

$$P_{x_1}=P(x_1)=\begin{cases}(\underline{x}_1-x_1)^2, & x_1\leq\underline{x}_1\\ (x_1-\bar{x}_1)^2, & x_1\geq\bar{x}_1\\ 0, & \text{otherwise,}\end{cases} \tag{2.80}$$

$\tilde{P}_{u_1}=\phi_1\cdot P_{u_1}$, $\tilde{P}_{u_2}=\phi_2\cdot P_{u_2}$, and $\tilde{P}_{x_2}=\phi_3\cdot P_{x_2}$, where

$$P_{u_1}=P(u_1)=\begin{cases}(\underline{u}_1-u_1)^2, & u_1\leq\underline{u}_1\\ (u_1-\bar{u}_1)^2, & u_1\geq\bar{u}_1\\ 0, & \text{otherwise,}\end{cases},$$

$$P_{u_2}=P(u_2)=\begin{cases}(\underline{u}_2-u_2)^2, & u_2\leq\underline{u}_2\\ (u_2-\bar{u}_2)^2, & u_2\geq\bar{u}_2\\ 0, & \text{otherwise,}\end{cases},$$

$$P_{x_2}=P(x_2)=\begin{cases}(\underline{x}_2-x_2)^2, & x_2\leq\underline{x}_2\\ (x_2-\bar{x}_2)^2, & x_2\geq\bar{x}_2\\ 0, & \text{otherwise,}\end{cases},$$

and where $\phi_1=(1/\bar{u}_1)^2$, $\phi_2=(1/\bar{u}_2)^2$, and $\phi_3=(1/\bar{x}_2)^2$ are meant to scale $\tilde{P}_{u_1}$, $\tilde{P}_{u_2}$, and $\tilde{P}_{x_2}$ down to the range of values of P_{x_1}.

2.6.3.2 Implicit Hamiltonian minimization

Considering optimality conditions (2.33c)-(2.33d) and cost functional, (2.78a) can be solved via the following BVP:

$$\dot{x}_1(t) = \frac{-U + \sqrt{U^2 - 4 \cdot R_b \cdot (w - u_1^* - V_{bus} \cdot u_2^*)}}{2 \cdot Q\, R_b}, \tag{2.81a}$$

$$\dot{x}_2(t) = \frac{-x_2 + \sqrt{x_2^2 - 4 \cdot R_{sc} \cdot V_{bus} \cdot u_2^*}}{2 \cdot C \cdot R_{sc}}, \tag{2.81b}$$

$$\dot{\lambda}_1(t) = -\frac{1}{\varepsilon}\frac{\partial P_{x_1}}{\partial x_1}, \tag{2.81c}$$

$$\dot{\lambda}_2(t) = -\lambda_2 \frac{\partial \dot{x}_2}{\partial x_2} - \frac{1}{\varepsilon}\frac{\partial \tilde{P}_{x_2}}{\partial x_2}, \tag{2.81d}$$

$$\dot{u}^*(t) = -\left(\frac{\partial q}{\partial u}\right)^{-1}\left(\frac{\partial q}{\partial x}\dot{x} + \frac{\partial q}{\partial \lambda}\dot{\lambda} + \frac{\partial q}{\partial w}\dot{w}\right), \tag{2.81e}$$

$$q(0) = 0, \tag{2.81f}$$

$$\text{state boundary constraints (2.78h)} - \text{(2.78k)}. \tag{2.81g}$$

with $u = \begin{bmatrix} u_1 & u_2 \end{bmatrix}^T$, $x = \begin{bmatrix} x_1 & x_2 \end{bmatrix}^T$, $q = \begin{bmatrix} q_1 & q_2 \end{bmatrix}^T$. The solution to (2.81) is denoted as $Y(t) = \begin{bmatrix} x_1(t) & x_2(t) & \lambda_1(t) & \lambda_2(t) & u_1^*(t) & u_2^*(t) \end{bmatrix}^T$. The dynamics of Y is denoted as $F(Y, t)$.

2.6.3.3 Function extension

Dynamics $F(Y, t)$ is not defined for all $\mathbb{R}^6$ due to the presence of the terms $\sqrt{U^2 - 4 \cdot R_b \cdot P_b}$ and $\sqrt{x_2^2 - 4 \cdot R_{sc} \cdot P_{sc}}$. The former term, which is defined for $U^2 - 4 \cdot R_b \cdot P_b \geq 0$, will be replaced by:

$$f_{\text{ext},1}(P_b \,|\, \tilde{P}_b) = \begin{cases} \sqrt{U^2 - 4 \cdot R_b \cdot P_b}, & \text{if } P_b \geq \tilde{P}_b \\ g_1(P_b), & \text{otherwise} \end{cases}$$

$$g_1(P_b) = \sqrt{U^2 - 4 \cdot R_b \cdot \tilde{P}_b} + (P_b - \tilde{P}_b)\frac{\mathrm{d}\left(\sqrt{U^2 - 4 \cdot R_b \cdot P_b}\right)}{\mathrm{d}P_b} + \frac{1}{2}(P_b - \tilde{P}_b)^2 \frac{\mathrm{d}^2\left(\sqrt{U^2 - 4 \cdot R_b \cdot P_b}\right)}{\mathrm{d}P_b^2},$$

with $\tilde{P}_b \leq \frac{U^2}{4 \cdot R_b}$. The term $\sqrt{x_2^2 - 4 \cdot R_{sc} \cdot P_{sc}}$, which is defined for $x_2^2 - 4 \cdot R_{sc} \cdot P_{sc} \geq 0$, will be replaced by the following extended function:

$$f_{\text{ext},2}(x_2, P_{sc} \,|\, \tilde{x}_2, \tilde{P}_{sc}) = \begin{cases} \sqrt{x_2^2 - 4 \cdot R_{sc} \cdot P_{sc}}, & \text{if } P_{sc} \geq \tilde{P}_{sc} \text{ or } x_2 \leq \tilde{x_2} \\ g_2(x_2, P_{sc}), & \text{otherwise} \end{cases}$$

$$g_2(x_2, P_{sc}) = \sqrt{\tilde{x}_2^2 - 4 \cdot R_{sc} \cdot \tilde{P}_{sc}} + \left(\begin{bmatrix} x_2 - \tilde{x}_2 \\ P_{sc} - \tilde{P}_{sc} \end{bmatrix} \right)^T \frac{\partial \left(\sqrt{x_2^2 - 4 \cdot R_{sc} \cdot P_{sc}} \right)}{\partial \begin{bmatrix} x_2 \\ P_{sc} \end{bmatrix}} + \left(\begin{bmatrix} x_2 - \tilde{x}_2 \\ P_{sc} - \tilde{P}_{sc} \end{bmatrix} \right)^T \frac{\partial \left(\sqrt{x_2^2 - 4 \cdot R_{sc} \cdot P_{sc}} \right)}{\partial \begin{bmatrix} x_2 \\ P_{sc} \end{bmatrix}} \left(\begin{bmatrix} x_2 - \tilde{x}_2 \\ P_{sc} - \tilde{P}_{sc} \end{bmatrix} \right),$$

with $\tilde{P}_{sc} = 2 \cdot 10^4$ (W) and $\tilde{x}_2 = 60$ (V) which ensures that $x_2^2 - 4 \cdot R_{sc} \cdot P_{sc} \geq 0$.

2.6.4 Numerical results

The EMS will be solved considering the vehicle parameters of Table 2.5. The initial guess Y^a is generated as described in *Step a* 2.4.4.3 using $\lambda(0) = \begin{bmatrix} 3.258 \cdot 10^7 & 3.622 \cdot 10^7 \end{bmatrix}^T$ and the initial penalty pondering coefficient $\varepsilon^a = 1 \cdot 10^{10}$. The obtained initial solution Y^a is depicted in Fig. 2.13. The supercapacitor voltage reaches negative values, illustrating that the initial guess does not necessarily have a physical meaning.

The final conditions from Y^a, $\begin{bmatrix} x_1^a(t_f), x_2^a(t_f) \end{bmatrix}^T = \begin{bmatrix} 2.66 \cdot 10^4 & -1.89 \cdot 10^6 \end{bmatrix}^T$, are applied at the beginning of *Step b*: $\zeta_0^b = \begin{bmatrix} x_1^a(t_f), x_2^a(t_f) \end{bmatrix}^T$. *Step b* allows computing a solution that reaches the expected final state-of-charge and the necessary final condition for the second co-state: $\zeta_f^b = [x_1(t_f), x_2(t_f)]^T$. This procedure is depicted in Fig. 2.14. Its output Y_N^b, shown in Fig. 2.15, is the solution to EMS (2.78) without constraints, since the penalty functions are negligible: $\varepsilon^b = \varepsilon^a = 1 \cdot 10^{10}$. The output of *Step b*, Y_N^b, is used in *Step c*: $Y_0^c = Y_N^b$. *Step c* is used to activate the penalty functions. The initial penalty pondering coefficient is set to the same value of *Step b*: $\zeta_0^c = \varepsilon_0^c = \varepsilon^b = 1 \cdot 10^{10}$. The final penalty pondering coefficient is set to a small positive value: $\varepsilon_N^c = 1 \cdot 10^{-9}$. This procedure is depicted in Fig. 2.16. The output of *Step c*, Y_N^c, is the solution to constrained EMS (2.78) and is shown in Fig. 2.17. It allows computing the total fuel consumption : 9.415 l/100km.

As it ocurred in the solution of the previous application, the constrained EMS, see Fig. 2.17, presents discontinuity phenomena for $\lambda_1(t)$ and $\lambda_2(t)$. These phenomena are to be expected, whenever a state makes contact with its bounds [73]. The procedure proposed in this work does not require any *a priori* knowledge about these discontinuities.

Parameter	Value	Units
M_{eq}	2166	kg
A_s	1.98	m^2
c_d	0.32	-
c_r	0.01	-
γ	4.2	-
r_w	0.26	m
g	9.81	kg·m/s^2
J_{tm}	0.045	kg·m^2
V_{bus}	30	V
$\underline{P}_b$	-22656	W
$\bar{P}_b$	19584	W
U	528	V
Q	900	A·s
R_b	0.96	Ω
$\underline{x}_1$	0	%
$\bar{x}_1$	100	%
R_{sc}	0.0258	Ω
C	27.27	F
$\underline{x}_2$	55	V
$\bar{x}_2$	308	V
a	0.2924	g/s
b	0.0834	$\frac{g}{kW \cdot s}$
c	0.0055	$\frac{g}{(kW)^2 \cdot s}$
$\bar{u}_1$	17.5	kW
$\underline{u}_2$	-500	A
$\bar{u}_2$	500	A

TABLE 2.5: Parameters considered in the numerical experiments of application 2.

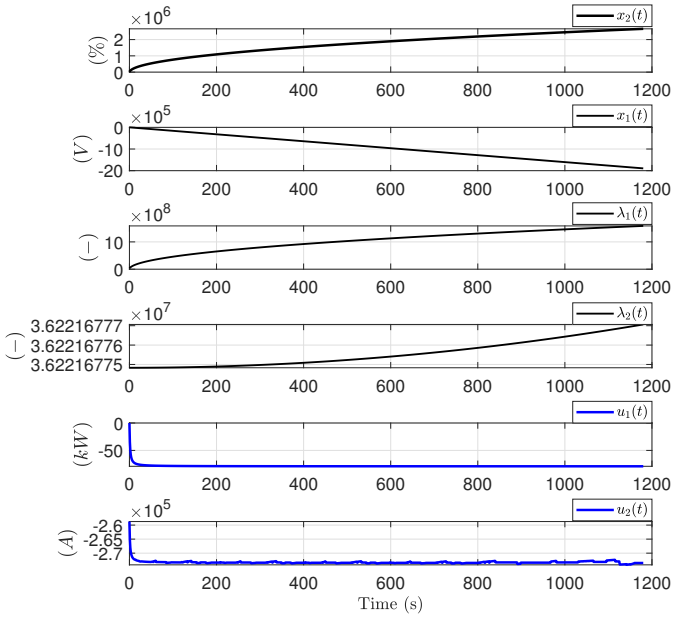

FIGURE 2.13: Initial guess Y^a generated in *Step a* for the WLTC-C3 driving cycle and the Dual Series HEV.

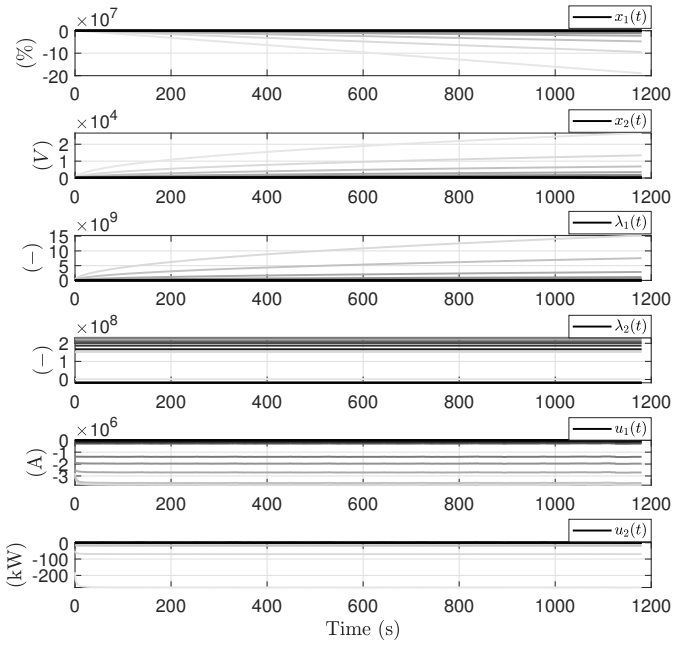

FIGURE 2.14: Set of solutions computed in *Step b* for the *low-temperature* operation and the WLTC-C3 driving cycle: the light gray trajectory denotes the first solution of the continuation procedure. As the trajectories become darker, they approach the final boundary conditions. The final trajectory of the procedure is displayed in black.

2.6.5 Solution via DP

The optimality of the approach will be validated by solving the EMS once again using DP. The DP algorithm is implemented using the Matlab code from [81], together with the iterative approach described in [82]. The solution has been computed using

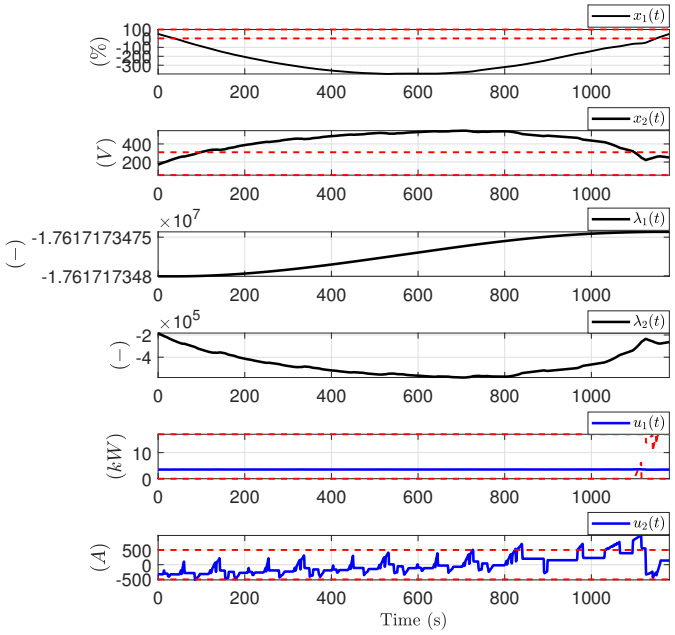

FIGURE 2.15: Unconstrained solution to (2.78) for the WLTC-C3 driving cycle. The fuel consumption is 9.2935 l/100km. The red dashed lines at the top and bottom subfigures represent the bounds on the state-of-charge, the supercapacitor voltage, and the control inputs (2.78f), (2.78g), (2.78d), and (2.78e), respectively.

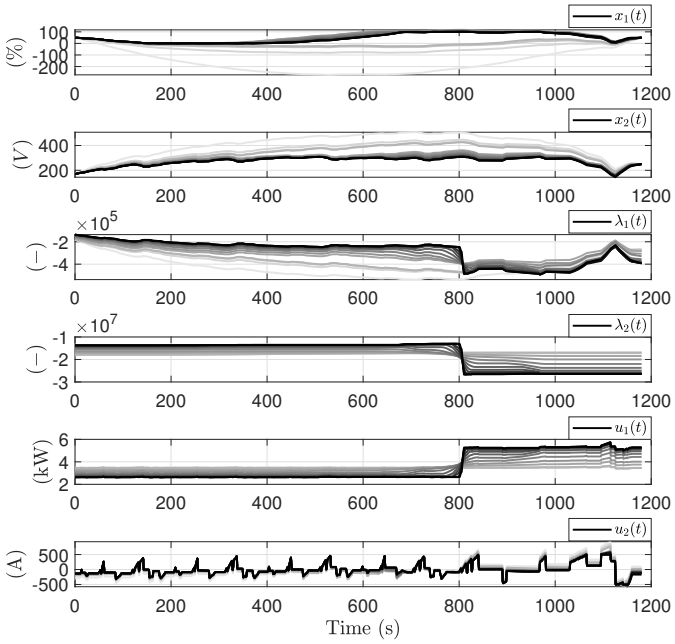

FIGURE 2.16: Set of solutions computed in *Step c* for the *low-temperature* operation and the WLTC-C3 driving cycle: the light gray trajectory denotes the first solution of the continuation procedure. As the trajectories become darker, they approach the constrained solution. The final trajectory of the procedure is displayed in black.

the parameters presented in Table 2.5. The results of the DP solution to (2.78) are displayed in Fig. 2.18 along with the solution computed with the implicit Hamiltonian minimization approach. The fuel consumption and computation times are compared in

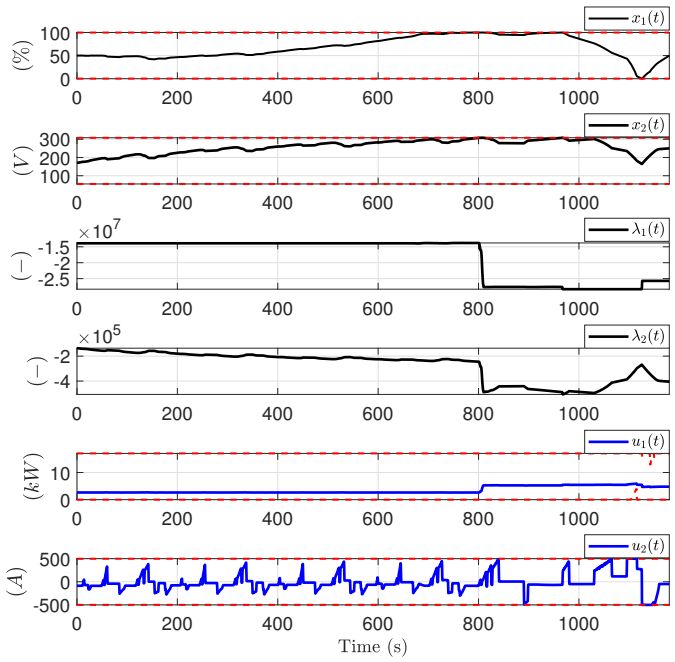

FIGURE 2.17: Constrained solution to (2.78) for the WLTC-C3 driving cycle. The fuel consumption is 9.415 l/100km. The red dashed lines at the top and bottom subfigures represent the bounds on the state-of-charge, the supercapacitor voltage, and the control inputs (2.78f), (2.78g), (2.78d), and (2.78e), respectively.

Table 2.6. The proposed approach is 35 times faster than DP but obtains +0.043% more fuel consumption. The small difference in fuel consumption can be due to the limited accuracy that DP posses as a consequence of the quantization of all variables and the Euler integration scheme in which it relies on.

Method	Fuel consumption (WLTC-C3)	Computation time (hours)
DP	9.411 l/100km (100%)	7.286 (≈3500%)
Implicit Hamiltonian minimization	9.415 l/100km (100.043%)	0.206 (100%)

TABLE 2.6: Fuel consumption and computation time for DP and the proposed implicit Hamiltonian minimization for the dual series HEV application. The algorithms were implemented in a workstation with 64 GB of RAM and a processor Intel(R) Core(TM) i7-9800X CPU @3.80GHz with 8 cores.

2.7 Conclusion

An indirect-approach method to compute the optimal offline energy management strategy of a hybrid vehicle with several continuous states and under input and state constraints has been proposed. The indirect-approach method relies on exterior penalty functions and an implicit Hamiltonian minimization to handle the constraints and solve

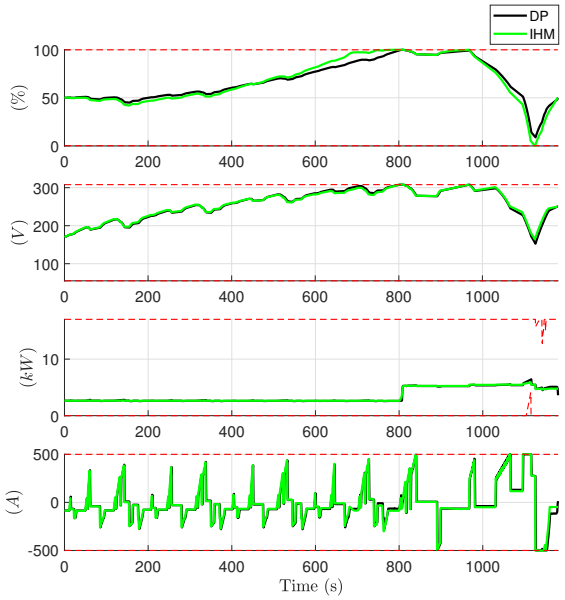

FIGURE 2.18: Solution to (2.78) for operation and the WLTC-C3 driving cycle with DP (green solid line) and the proposed implicit Hamiltonian minimization (black solid line). The red dashed lines at the top and bottom subfigures represent the bounds on the state-of-charge, the supercapacitor voltage, and the control inputs (2.78f), (2.78g), (2.78d), and (2.78e), respectively.

the Pontryagin's minimum principle optimality conditions. A continuation procedure and a domain function-extension are also proposed to deal with the difficulties of computing a numerical solution. The proposed method does not require any *a priori* knowledge on the optimal solution and can be applied to energy management formulations with several inputs and states. The proposed method is shown effective by solving the offline energy management strategy for:

- a series HEV under *low-temperature* conditions modeled as a two-state, the battery state-of-energy and temperature, mixed input-state constrained problem, and
- a dual series HEV modeled as a two-state, the battery state of charge and the supercapacitor voltage, two-input, the APU power and the current going through the supercapacitor, mixed input-state constrained problem.

The optimality of the solution is validated by obtaining a slightly different solution via dynamic programming. The small difference is not surprising since in dynamic programming all variables are quantized, which limits the accuracy of the solution. Moreover, the proposed method shows to be up to 46 times faster than dynamic programming.

One possible extension of this work is to solve a more general energy management formulation, for example, by considering both the engine and the catalytic converter temperature and including the emission of pollutants in the objective function [18, 83].

Also, real-time algorithms for hybrid vehicle energy management were derived using the Pontryagin's minimum principle within a model predictive control framework in [84]. The method proposed here could be combined with the latter to account for mixed input-state constraints and a second dynamics in a real-time energy management algorithm but more work is needed to cope with the actual computing power available on a vehicle.

Chapter 3

Energy management and active damping of the side-shaft oscillations

3.1 Introduction

In a hybrid electric vehicle (HEV) powertrain, the main role of the electric machines (EMs) is to achieve the powersplit that reduces the total fuel consumption for a given driving mission. Furthermore, the capabilities of a powertrain to solve automotive related problems go beyond this main purpose. One of these problems is the presence of drive-shaft oscillations. In a vehicle with a gear-based transmission, it is is mainly perceivable at low gear ratios (first and second), so it occurs at relatively low speeds. The reason behind this is that when a low gear ratio is engaged and the driver demands strong accelerations, the driveshaft experiences steep and particularly high torque changes, thus, exciting its torsional dynamics to the point of producing noticeable torque and speed oscillations. These oscillations affect the driver's comfort and can *stress* the vehicle's components [55, 56]. Since the EMs are actuators with a larger frequency response than that of internal combustion engines (ICEs), they can be used to actively damp the drive-shaft oscillations. Moreover, considering that most of the energetic flow on the powertrain is carried by low frequency signals and that drive-shaft oscillations have higher frequencies, it is possible to design a damping controller such that its influence on the energetic behavior of the vehicle is negligible.

Several works in the literature are concerned with active damping of the drive-shaft oscillations for conventional [85–90], hybrid [91–98], and electric vehicles [54, 56, 99, 100]. PID-based controllers were designed to actively damp the oscillations for a conventional

vehicle as well as an HEV in [90]. There, it is found that due to the fast response of the electric machine, an HEV allows for a more effective damping than a conventional ICE vehicle. A PID controller was also compared to a linear-quadratic-guassian (LQG) controller for a conventional heavy-duty truck in [86]. The LQG controller was found to be superior and it was implemented in real-time. This work was extended to a parallel HEV in [91], contrary to [90], there the ICE torque is also considered a control signal, i.e., the problem formulation contains two inputs and control allocation is use to split the damping torque between the two actuators. In [92], active damping was used in a power-split HEV to suppress the torque oscillations at the wheels below 100 N·m (the minimum value perceived by the driver on the 1820-kg vehicle studied there). This study included experimental validation. A powersplit HEV is also studied in [98], where model reference adaptive control is combined with linear state feedback to produce a controller that can overcome the uncertainty generated by the changing transmission ratio. The controller is tested in a hardware-in-the-loop experiment

In [99], a nonlinear observer is combined with a controller designed on the frequency domain to actively damp the drive-shafts of an electric vehicle. A discrete Kalman filter is the chosen observer. The observer dynamics includes a measurement time-delay for the speed at the wheels, induced by the controller area network (CAN) bus, and a nonlinearity introduced by the backlash phenomenon. Oscillations are damped for a powersplit HEV in [95], via a linear quadratic regulator with loop transfer recovery LQR/LTR and integral action. The integral action is based on the assumption that the actual driveshaft torque and the desired driveshaft torque, commanded by the EMS, are available. In [56], a damping controller including time-varying delays compensation induced by the CAN bus is designed with a guaranteed H_∞ performance. The effect of the controller under braking conditions is studied by the modeling of the hydraulic braking system and a cooperative braking control algorithm. The desired damping effect is corroborated by HIL simulations. In [100], the proposed control scheme relies on a dual Kalman filter to estimate the vehicle mass and the driveshaft torsion. As in [99], nonlinear phenomena induced by backlash is included in the problem formulation. The estimated torsion is used to decide whether the driveline is either in contact mode or in backlash mode. If the driveline is in contact mode, then a LQR controller is in charge of damping the oscillations. If the driveline is in backlash mode, a PID controller is used instead. Model predictive control was considered in [54] to damp the oscillations in an electric bus. Damping is achieved by the minimization of two square error signals: (1) the minimization of the difference between shaft and wheel speeds and their predicted future values, computed as if the shaft was ideally stiff, and (2) the minimization of the difference between the reference shaft torque and the actual shaft torque. If the second error term was not considered in the objective functional, the controller could

still successfully damp the oscillations but at the cost of overriding the torque request from the driver or the EMS.

3.1.1 Motivation

In the case of an HEV, a proper EMS allows to reduce the vehicle total fuel consumption, and thus the pollution and emission of green-house effect gasses, and as such it is the most important feature of this type of vehicle. Nevertheless, most of the works discussed above overlook the energetic cost/effect of their proposed controllers. Motivated by this mostly overlook aspect, the present work is concerned with the design of a damping controller and the study of its influence on the energetic behavior of the powertrain.

3.1.2 Contribution

A damping controller for a parallel HEV with a gear-based transmission. The controller is based on discrete RST compensation. It includes communication delays induced by the CAN bus and it relies only on the hardware already present in the vehicle. More importantly, contrary to the current works found in the literature, in this work it is shown that the damping controller does not compromise the proper operation of the EMS. The effectiveness of the controller is shown in simulation and experimental results.

3.1.3 Organization

The organization for the rest of the Chapter is as follows. Section 3.2 presents the problem formulation and the considered driveline model. Section 3.3 details the proposed damping controller. In Section 3.4, the robustness of the proposed controller to parametric uncertainty is studied. In Section 3.5, it is shown that the controller does not significantly affect the EMS. Experimental validation of the control law is presented in Section 3.6. At last, conclusions and possible future work extensions are discussed in Section 3.7.

3.2 Problem formulation

The system studied in this work is a parallel P_0 HEV, whose powertrain is shown in Fig. 3.1. When the driver requests power through the throttle pedal, the EMS sends torque setpoints to the ICE and the EM to satisfy the power-request according to the optimal powersplit. However, when the driver requests a *brutal/important* acceleration to the

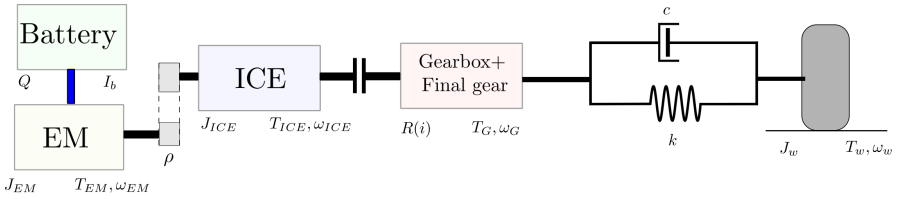

FIGURE 3.1: Pre-transmission ($P0$) parallel HEV. Blue lines represent electric connections and black lines for mechanical connections.

vehicle, the sudden high torque signal sent through the driveline may be high enough to excite its torsional dynamics in such a way that it generates wheel speed oscillations. These oscillations have a negative effect on the driveability and are mainly produced by the sideshaft flexibility. This phenomenon is illustrated in Fig. 3.2 with signals from a physical experiment recorded at the LAMIH UMR CNRS 8201 using a prototype hybrid vehicle BELHYSYMA [2]: a pre-transmission (P0) HEV with a synchronous belt, a 35kW electric machine, and a 12.5Ah-100V Li-ion battery pack. Driveshaft oscillations

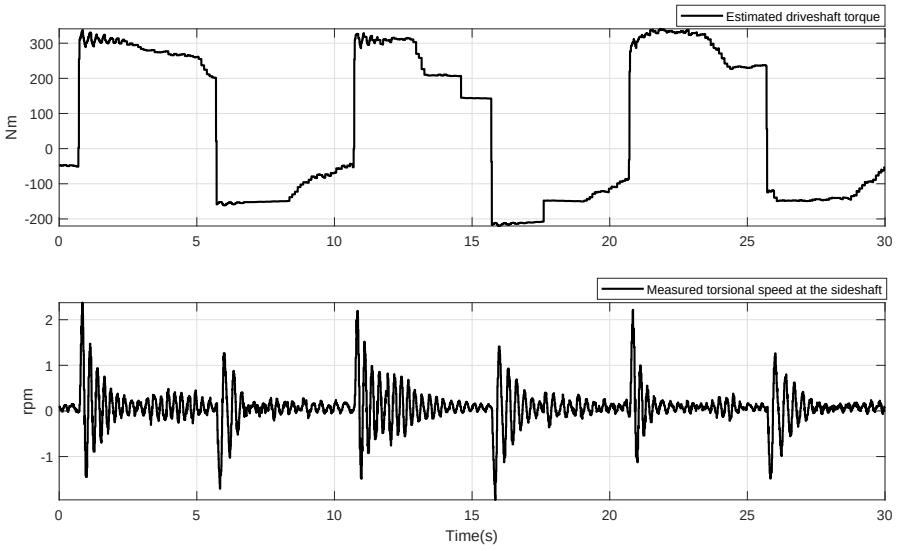

FIGURE 3.2: Results from a physical experiment recorded at the LAMIH UMR CNRS 8201 using a prototype hybrid vehicle BELHYSYMA [2]. Top: estimated driveshaft torque. Bottom: driveline oscillations at the torsional speed. The torsional speed is defined as the difference between the speed at the transmission output and the speed at the wheels.

can be mitigated or damped without any hardware modification by adding a damping torque to the setpoints from the EMS. The design of the controller providing the damping torque signal should affect the energetic behavior of the powertrain as little as possible. In other words, it is constrained to not modifying the setpoints provided by the EMS in a significant way. Since the sideshaft torsion mode is in the 2-10Hz bandwidth, the EM is chosen here as the actuator that provides the damping torque. As a consequence, $T_{EM}(t)$, the EM torque setpoint, is defined as the sum of $T'_{EM}(t)$, the torque setpoint

from the EMS, and $u(t)$ the damping controller:

$$T_{EM}(t) = T'_{EM}(t) + u(t) \tag{3.1}$$

The controller configuration is shown in Fig. 3.3, with T_{ICE} the ICE torque setpoint, Σ the vehicle driveline, and $y(t)$ the vector of measured powertrain signals. The model derived for Σ will be detailed in the next section.

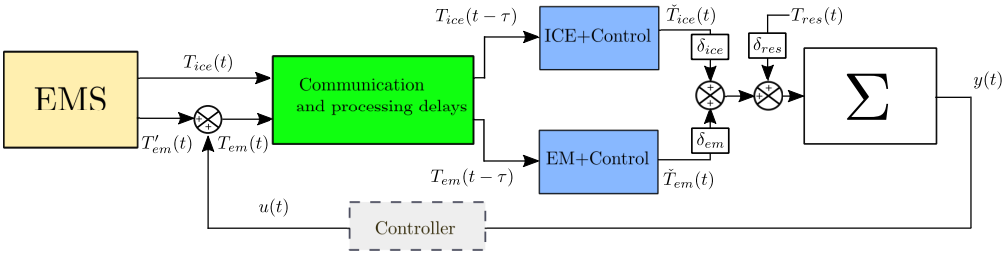

FIGURE 3.3: Configuration of the damping controller.

3.2.1 Model derivation

The driveline model considered in this work is based on Fig. 3.1. It assumes that all the elements of the driveline except the sideshafts have ideal stiffness and that the clutch is always engaged, i.e., there is no gearshifting. Under these assumptions, the torsional dynamics can be computed using the simplified model shown in Fig. 3.4. It consists of a rotational two-mass-spring-damper system whose stiffness is denoted by k and its damping by c. Although simple, it has been widely used in the literature since it can capture the phenomenon of interest, and hence it is suitable for control design [85, 86]. $J_G = R(i)^2 \cdot \left(J_{ICE} + \rho^2 \cdot J_{EM}\right)$, with J_{EM} the electric machine intertia, J_{ICE} the ICE inertia, $R(i)$ the total transmission gear ratio, and ρ the electric machine reductor gear ratio. The equivalent inertia at the wheels, J_w, is equal to $J_w = m \cdot r^2$, with m the total vehicle mass (kg) and r (m) the wheel radius. $T_{tor} = k \cdot \Delta\theta + c \cdot \Delta\dot{\theta}$. $T_{tract} = R(i) \cdot \left(\rho \cdot \check{T}_{EM} + \check{T}_{ICE}\right)$ with $\Delta\theta = \theta_G - \theta_w$, θ_G the angular position of J_G and θ_w the angular position of J_w. Applying Newton's second law at J_G, one gets:

$$\begin{aligned} J_G \cdot \dot{\omega}_G &= T_{tract} - T_{tor}, \\ J_G \cdot \dot{\omega}_G &= R(i) \cdot \left(\rho \cdot \check{T}_{EM} + \check{T}_{ICE}\right) - k \cdot \Delta\theta + c \cdot \Delta\dot{\theta}, \\ \iff \dot{\omega}_G &= \frac{1}{J_G} \cdot \left[R(i) \cdot \left[\rho \cdot \check{T}_{EM} + \check{T}_{ICE}\right) - k \cdot \Delta\theta + c \cdot \Delta\dot{\theta}\right]. \end{aligned} \tag{3.2}$$

Applying Newton's second law at inertia J_w, one gets:

$$\begin{aligned} J_w \cdot \dot{\omega}_w &= T_{tor} - T_{res}, \\ J_w \cdot \dot{\omega}_w &= k \cdot \Delta\theta + c \cdot \Delta\dot{\theta} - T_{res}, \\ \Longleftrightarrow \dot{\omega}_w &= \frac{1}{J_w} \cdot \left[k \cdot \Delta\theta + c \cdot \Delta\dot{\theta} - T_{res} \right]. \end{aligned} \tag{3.3}$$

Considering (3.2), (3.3), and $\Delta\ddot{\theta} = \dot{\omega}_G - \dot{\omega}_w$:

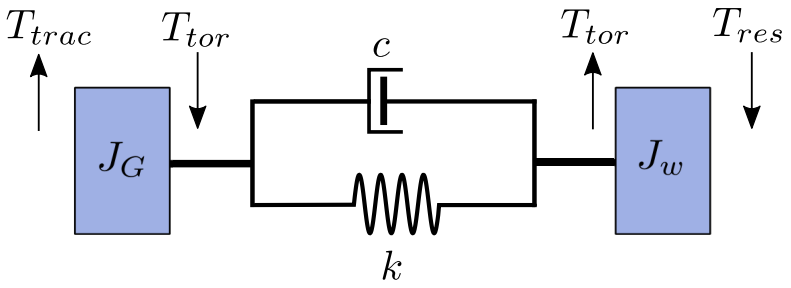

FIGURE 3.4: Equivalent simplified driveline with flexible sideshaft.

$$\begin{aligned} \Delta\ddot{\theta} &= \left(\frac{1}{J_G} \cdot \left[R(i) \cdot \left[\rho \cdot \check{T}_{EM} + \check{T}_{ICE} \right) - k \cdot \Delta\theta + c \cdot \Delta\dot{\theta} \right] \right) - \left(\frac{1}{J_w} \cdot \left[k \cdot \Delta\theta + c \cdot \Delta\dot{\theta} - T_{res} \right] \right), \\ \Delta\ddot{\theta} &= -\left(\frac{1}{J_G} + \frac{1}{J_w} \right) k \cdot \Delta\theta - \left(\frac{1}{J_G} + \frac{1}{J_w} \right) c \cdot \Delta\dot{\theta} + \frac{R(i)}{J_G} \cdot \left(\rho \cdot \check{T}_{EM} + \check{T}_{ICE} \right) + \frac{1}{J_w} T_{res}, \end{aligned} \tag{3.4}$$

Note that even though the system is actually a third-order system, as it requires 3 states to be completely defined, a second-order formulation (3.4) is sufficient to design the controller. The dynamics of the EM together with its built-in controller are modeled with a first-order linear system with time constant τ_{em}:

$$\dot{\check{T}}_{em}(t) = -\frac{1}{\tau_{em}} \check{T}_{em}(t) + T_{em}(t - \tau). \tag{3.5}$$

Assuming zero initial conditions for $\check{T}_{em}(t)$ and considering that a time-delay is a linear operator, yields the following:

$$\dot{\check{T}}'_{em}(t) = -\frac{1}{\tau_{em}} \check{T}'_{em}(t) + T'_{em}(t - \tau), \tag{3.6}$$

$$\dot{\check{u}}_{em}(t) = -\frac{1}{\tau_{em}} \check{u}_{em}(t) + u(t - \tau), \tag{3.7}$$

with $\check{T}_{em} = \check{T}'_{em} + \check{u}_{em}$. Defining $\alpha = \left(\frac{1}{J_G} + \frac{1}{J_w}\right)$, and defining $\beta = \frac{\rho \cdot R(i)}{J_G}$, and considering (3.6), the state-space model is given by:

$$\begin{bmatrix} \Delta\dot{\theta} \\ \Delta\ddot{\theta} \\ \dot{\check{u}} \end{bmatrix} = \underbrace{\begin{bmatrix} 0 & 1 & 0 \\ -\alpha \cdot k & -\alpha \cdot c & \frac{\beta}{\tau_{em}} \\ 0 & 0 & -\frac{1}{\tau_{em}} \end{bmatrix}}_{A} \begin{bmatrix} \Delta\theta \\ \Delta\dot{\theta} \\ \check{u} \end{bmatrix} + \underbrace{\begin{bmatrix} 0 \\ 0 \\ 1 \end{bmatrix}}_{B} u(t-\tau) + \underbrace{\begin{bmatrix} 0 \\ 1 \\ 0 \end{bmatrix}}_{H} \underbrace{\left(\frac{R(i)}{J_G} \cdot \left(\rho \cdot \check{T}'_{EM} + \check{T}_{ICE}\right) + \frac{1}{J_w} T_{res}\right)}_{z}, \tag{3.8a}$$

$$y = \underbrace{\begin{bmatrix} 0 & 1 & 0 \end{bmatrix}}_{C} \begin{bmatrix} \Delta\theta \\ \Delta\dot{\theta} \\ \check{u} \end{bmatrix}, \tag{3.8b}$$

3.3 Controller design

The control objective is to damp the sideshaft oscillations without interfering with the EMS: in steady-state, we should get $T_{em} = T'_{em}$, which is equivalent to u being a vanishing controller:

$$\lim_{\Delta\dot{\theta} \to 0} u(t) = 0. \tag{3.9}$$

Defining $\mathcal{L}\{\cdot\}$ as the Laplace transform operator, $U(s) = \mathcal{L}\{u(t)\}$, $Y(s) = \mathcal{L}\{y(t)\}$, and $Z(s) = \mathcal{L}\{z(t)\}$, the transfer function $Y(s)/U(s)$ is given as follows:

$$\frac{Y(s)}{U(s)} = C\ (s \cdot I - A)^{-1}\ B \cdot e^{-\tau s} = \frac{\beta \cdot s \cdot e^{-\tau s}}{(\tau_{em} \cdot s + 1)\,(s^2 + \alpha\, c \cdot s + \alpha\, k)}, \tag{3.10}$$

and $Y(s)/Z(s)$ is given as follows:

$$\frac{Y(s)}{Z(s)} = C\ (s \cdot I - A)^{-1}\ H = \frac{s}{s^2 + \alpha\, c \cdot s + \alpha}. \tag{3.11}$$

Considering the parameters of Table 3.1, the Bode plot of (3.11) is given in Fig. 3.5: the resonant frequency occurs at 3.76 Hz. Given (3.10) and (3.11), $Y(s)$ is given by:

$$Y(s) = \frac{\beta \cdot s \cdot e^{-\tau s}}{s^2 + \alpha\, c \cdot s + \alpha\, k} \cdot \left(U'(s) + \beta^{-1}\, e^{\tau s} \cdot Z(s)\right), \tag{3.12}$$

with $U'(s) = \frac{1}{\tau_{em} \cdot s + 1} U(s)$. The system will be discretized and an RST approach [101] will be used to design the damping controller. Considering a sampling period T_s, $\tau = N \cdot T_s$ and a zero-order hold discretization method, the system transfer functions are written

Symbol	Value	Units
r_{wheel}	0.3108	(m)
J_{ice}	0.0616	(kg·m^2)
J_{em}	0.0045	(kg·m^2)
c	23.53	(N·m·s/rad)
k	$2.863{\cdot}10^3$	(N·m/rad)
ρ	1	(-)
$R(i)$	$\{16.45, 8.89, 6.15, 4.54, 3.55\}$	(-)
m	1742	(kg)
c_{rr}	0.0068	(-)
A_f	2.3185	(m^2)
c_{air}	0.314	(-)
T_s	20	(ms)

TABLE 3.1: Nominal driveline model parameters.

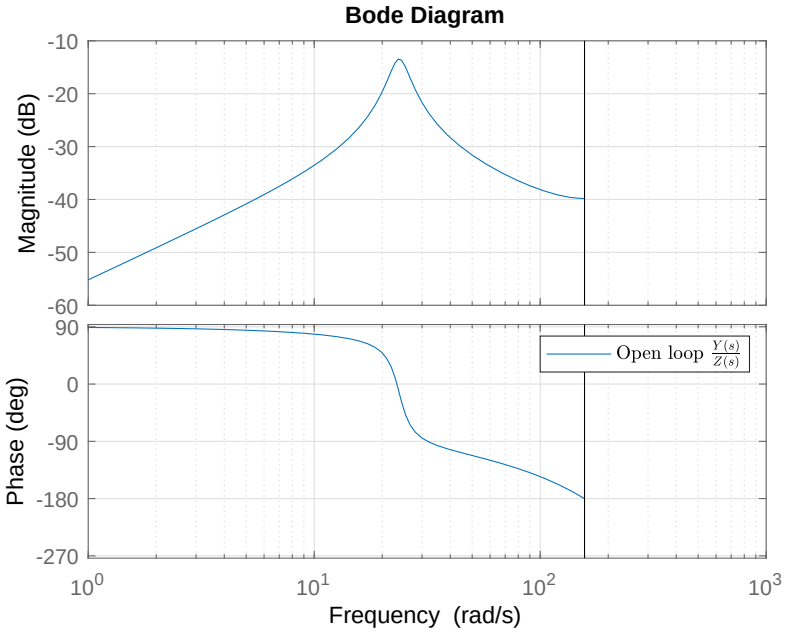

FIGURE 3.5: Open-loop Bode plot of (3.11) for the parameters of Table 3.1 with the second gear engaged: $R(i) = 8.89$.

using the following polynomials:

$$A(z^{-1}) = a_0 + a_1 \cdot z^{-1} + a_2 \cdot z^{-2}, \tag{3.13}$$

$$B(z^{-1}) = a_0 \cdot z^{-N} + a_1 \cdot z^{-(N+1)}, \tag{3.14}$$

$$b_{em}(z^{-1}) = b_{em,0}, \tag{3.15}$$

$$a_{em}(z^{-1}) = a_{em,0} + a_{em,1} \cdot z^{-1}, \tag{3.16}$$

with $R(z^{-1})$ and $S(z^{-1})$ the polynomials in z^{-1} to be designed. The control scheme is depicted in Fig. 3.6. The closed-loop transfer function $Y(z^{-1})/Y_r(z^{-1})$ is given as follows:

$$\frac{Y(z^{-1})}{Y_r(z^{-1})} = \frac{B'(z^{-1}) \cdot R(z^{-1})}{A'(z^{-1}) \cdot S(z^{-1}) + B'(z^{-1}) \cdot R(z^{-1})}, \tag{3.17}$$

with $A' = A \cdot a_{em}$, $B' = B \cdot b_{em}$, and where $R(z^{-1})$ and $S(z^{-1})$ are to be designed such that the system has a desired denominator $C(z^{-1})$:

$$A(z^{-1})' \cdot S(z^{-1}) + B'(z^{-1}) \cdot R(z^{-1}) = C(z^{-1}). \tag{3.18}$$

Given the desired closed-loop plant, there are infinite ways to compute the parameters for an RST controller. In [102], the parameters are computed as a nonlinear optimization problem which is solved through evolutionary algorithms (for example, backtracking search optimization [103] or Particle Swarm Optimization [104]). A unique solution to (3.18) exists if the following identities are satisfied:

$$\deg(C) = \max\{\deg(A') + \deg(S), \deg(B') + \deg(R)\}, \tag{3.19}$$

$$\deg(R) + \deg(S) = \deg(C) - 1, \tag{3.20}$$

with $\deg(\cdot)$ the degree of the polynomial $(\cdot)$. Given (3.9), R should contain the factor $1 - z^{-1}$ in order to obey $Y(1)/Z(1) = 0$, and thus achieve a vanishing controller. The term $\left(1 + z^{-1}\right)^2$ is another predefined term of R, it is required to filter out-high frequency noise. $R(z^{-1}) = \left(1 - z^{-1}\right) \cdot \left(1 + z^{-1}\right)^2 \cdot R'(z^{-1})$:

$$A'(z^{-1}) \cdot S(z^{-1}) + B'(z^{-1}) \cdot \left(1 - z^{-1}\right) R'(z^{-1}) = C(z^{-1}), \tag{3.21}$$

$$A'(z^{-1}) \cdot S(z^{-1}) + B''(z^{-1}) \cdot R'(z^{-1}) = C(z^{-1}), \tag{3.22}$$

Considering $N = 3$ and $\deg(A) = 3$, then $\deg(B'') = 9$ and the identities above can be satisfied by choosing $\deg(S) = \deg(B'') - 1 = 8$, $\deg(R') = \deg(A') - 1 = 2$, and $\deg(C) = \deg(R) + \deg(S) + 1 = 11$:

$$R'(z^{-1}) = r'_0 + r'_1 \cdot z^{-1} + r'_2 \cdot z^{-2}, \tag{3.23}$$

$$S(z^{-1}) = s_0 + s_1 \cdot z^{-1} + \ldots + s_8 \cdot z^{-8}. \tag{3.24}$$

The desired closed loop polynomial is chosen as follows $C = \left(z^{-1} - e^{-T_s \cdot \omega_n}\right)^2 \cdot \left(z^{-1} - d_{aux}\right)^3 \cdot z^{-6}$, with $d_{aux} = e^{-2 \cdot T_s \cdot \omega_n}$, and $\omega_n = \sqrt{\alpha \cdot k}$. The coefficients above

can be computed from the following system of linear equations:

$$\begin{bmatrix} a'_0 & 0 & \cdots & 0 & b''_0 & 0 & \cdots & 0 \\ a'_1 & a'_0 & \cdots & 0 & b''_1 & b''_0 & \cdots & 0 \\ \vdots & \vdots & \vdots & \vdots & \vdots & \vdots & \vdots & \vdots \\ a'_3 & a_2 & \cdots & 0 & b''_9 & b''_8 & \cdots & b''_0 \\ 0 & a_3 & \cdots & 0 & 0 & b''_9 & \cdots & b''_1 \\ \vdots & \vdots & \vdots & \vdots & \vdots & \vdots & \vdots & \vdots \\ 0 & 0 & \cdots & a_3 & 0 & 0 & \cdots & b''_9 \end{bmatrix} \begin{bmatrix} s_0 \\ s_1 \\ \vdots \\ s_8 \\ r'_0 \\ r'_1 \\ r'_2 \end{bmatrix} = \begin{bmatrix} c_0 \\ c_1 \\ \vdots \\ c_5 \\ 0 \\ \vdots \\ 0 \end{bmatrix} \tag{3.25}$$

The poles of the closed-loop system are shown in Fig (3.7). The Bode plots of

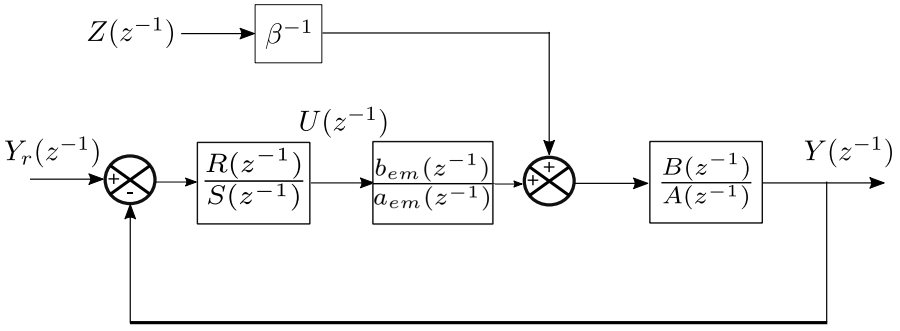

FIGURE 3.6: RST controller structure.

$Y(z^{-1})/Z(z^{-1})$ in closed and open loop are compared in Fig. 3.8. The closed-loop effectively damps the resonant frequency. However, it still presents a magnitude peak. In the following, in order to present a quantitative analysis of the controller performance, the oscillations in the torsional speed ($\Delta\dot{\theta}$) will be assessed using its root mean square (RMS) value:

$$\text{RMS} = \sqrt{\frac{1}{n} \cdot \sum_i \Delta\dot{\theta}[i]}. \tag{3.26}$$

3.3.1 Simulation test

The control law designed in the previous section will be tested in simulation. The control law is given by:

$$U(z^{-1}) = \frac{R(z^{-1})}{S(z^{-1})}. \tag{3.27}$$

The parameters used for the simulation are those given in Table 3.1. These parameters have been validated with real-time experiments. Considering the torque setpoint signals

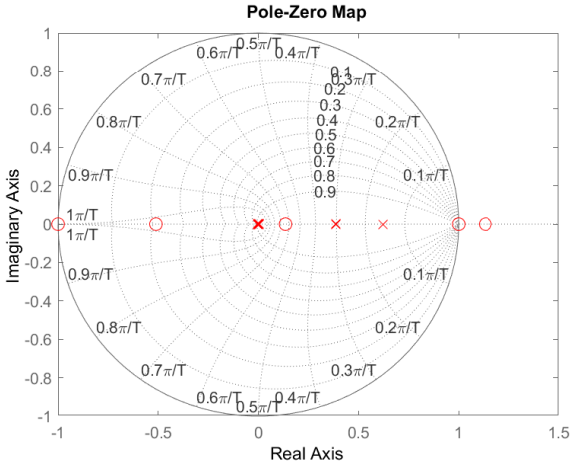

FIGURE 3.7: Closed-loop poles (red ×) and zeros (red ○) for transfer function (3.17).

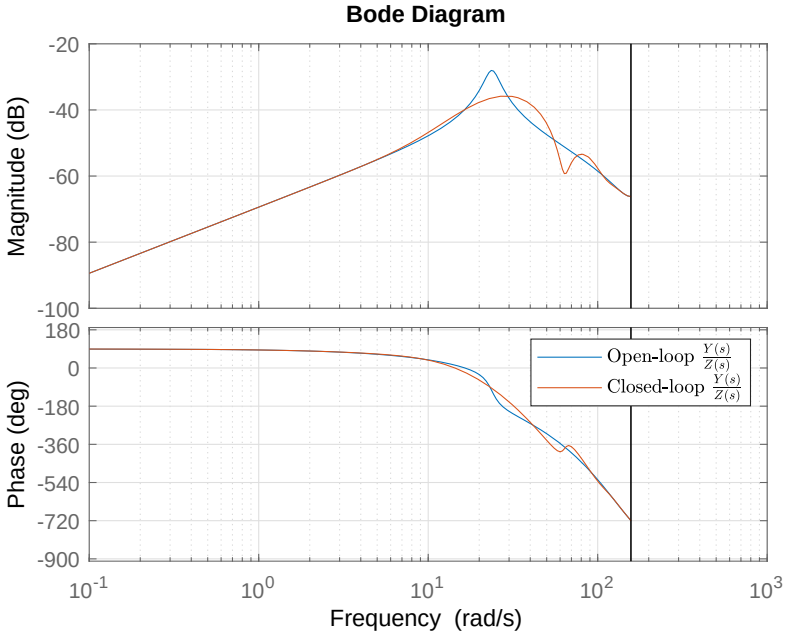

FIGURE 3.8: Bode plot of $Y(z^{-1})/Z(z^{-1})$ in closed-loop (red solid line) and open-loop (blue solid line) with the parameters given in Table 3.1 and the second gear engaged ($R(i) = 8.89$).

from the top subplot of Fig. 3.9, the response of the driveline torsional dynamics is given in the middle top and bottom subplots of the same figure: the control law, see bottom subplot of Fig. 3.9, effectively damps the oscillations: it provides a 24.35% reduction according to the RMS assessment (3.26). Moreover, it vanishes in steady-state, condition (3.9), as it is required for keeping it from interfering with the EMS. One can conclude that the control law is successful. However, in this simulation it is assumed that the system parameters are known exactly. This is is not the case for real control systems. Robustness with respect to parametric uncertainty is studied in the next section.

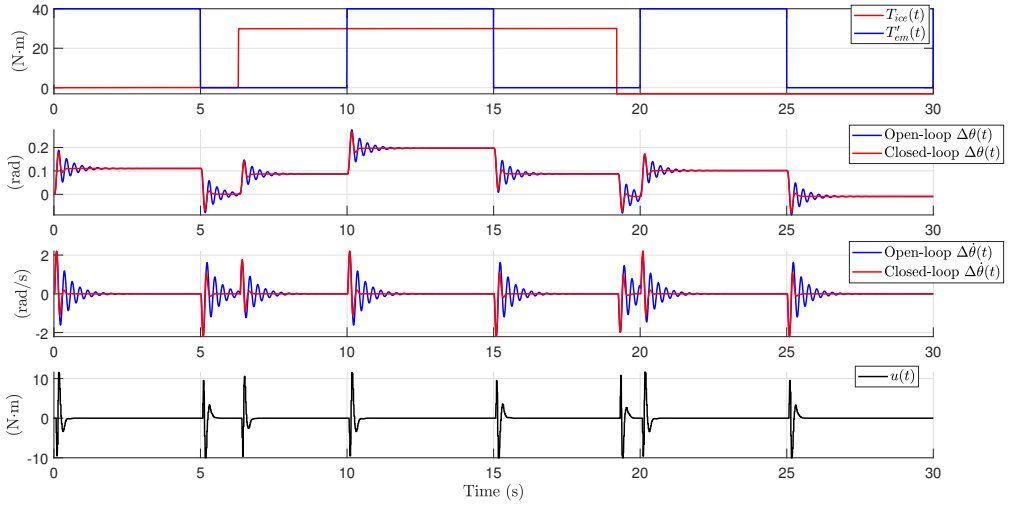

FIGURE 3.9: Torque setpoints T_{ice} and $T_{em} = T'_{em} + u$ (top); driveshaft torsion $\Delta\theta$ (middle up); driveshaft torsional speed $\Delta\dot{\theta}$ (middle bottom); torsional control $u(t)$ (bottom). The RMS values, (3.26), of the open and closed-loop response are 0.409 and 0.309, respectively. Second gear engaged: R(i)=8.89.

3.4 Robustness with respect to parametric uncertainty

The robustness with respect to parametric uncertainty will be tested. The parameters whose uncertainty is studied are the vehicle mass, m, the stiffness, k, and the damping coefficient c. Considering a disturbance signal, denoted as $P(z^{-1})$ at the output, the transfer function $U(z^{-1})/P(z^{-1})$ will be denoted as $S_{(PU)}$:

$$S_{(PU)} = \frac{-A' \cdot R}{A' \cdot S + B' \cdot R}. \tag{3.28}$$

Denoting the open-loop transfer function corresponding to the nominal system model as $G(z^{-1})$:

$$G(z^{-1}) = \frac{A'(z^{-1})}{B'(z^{-1})}, \tag{3.29}$$

and denoting as $G'(z^{-1})$ the real plant to be controlled. Controller (3.27) stabilizes $G'(z^{-1})$ if the following condition is satisfied [101]:

$$\left|G'(z^{-1}) - G(z^{-1})\right| \leq \left|\frac{1}{S_{(PU)}}\right|, \tag{3.30}$$

Condition (3.30) is graphically interpreted in Fig. 3.10. Any plant $G'(z^{-1})$, such that $|G'(z^{-1})|$ is inside the green area, will be stabilized when in closed-loop with (3.27).

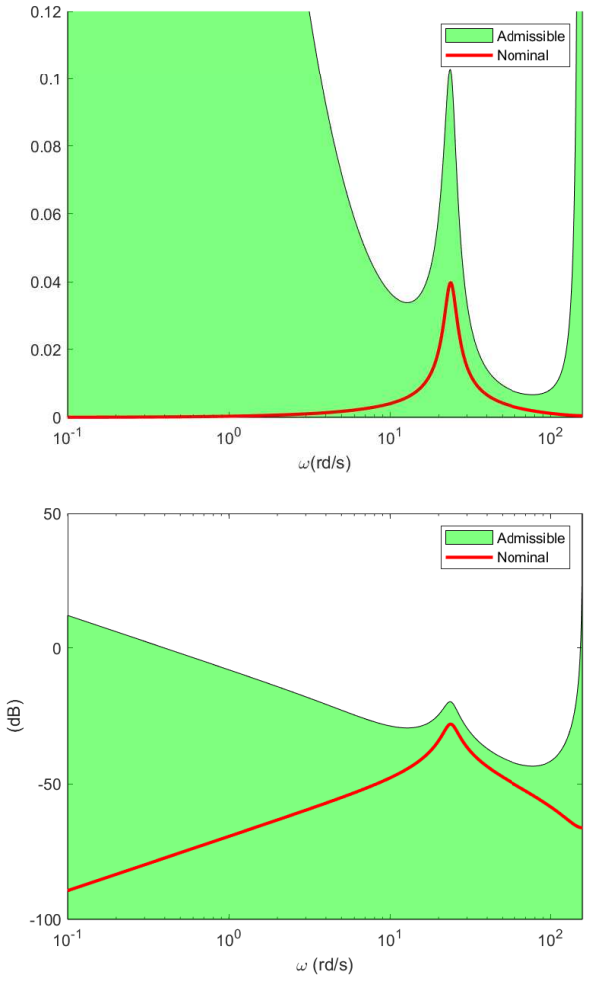

FIGURE 3.10: Nominal system gain $|G(z^{-1})|$ (solid red line) and admissible region for $|G'(z^{-1})|$ to be stabilizable (green area) when in closed-loop with (3.27) in natural scale (top) and dB scale (bottom).

3.4.1 Uncertainty in m

Let us assume that all the parameters except the total mass m of the nominal system $G(z^{-1})$ are equal to those of the real system $G'(z^{-1})$, and that m', the total mass of $G'(z^{-1})$, is an uncertain value bounded as follows $m' \in [0.5\,m, 1.5\,m]$. This is equivalent to a $\pm 50\%$ variation. The admissible region, (3.30), for $G'(z^{-1})$ is displayed in Fig. 3.11. It shows that the controller is highly robust with respect to mass variations.

3.4.2 Uncertainty in c

Let us assume that all the parameters except the total damping c of the nominal system $G(z^{-1})$ are equal to those of the real system $G'(z^{-1})$, and that c', the total damping of $G'(z^{-1})$, is an uncertain value bounded as follows $c' \in [0.75\,c, 1.25\,c]$. This is equivalent

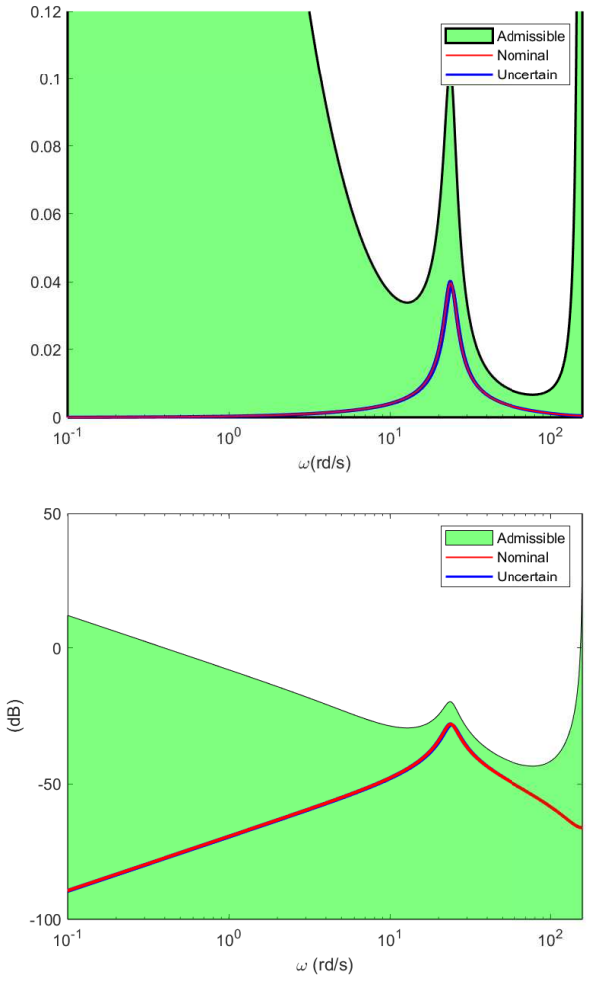

FIGURE 3.11: Nominal system gain $|G(z^{-1})|$ (solid red line), set of open-loop system variations with $m' \in [0.5\,m, 1.5\,m]$ (blue area), and admissible region for $|G'(z^{-1})|$ to be stabilizable (green area) when in closed-loop with (3.27) in natural scale (top) and dB scale (bottom).

to a $\pm 25\%$ variation. The admissible region, (3.30), for $G'(z^{-1})$ is displayed in Fig. 3.12. Under the considered uncertainty levels, the set of open-loop system variations induced by uncertainty in c remains in the admissible region, i.e., the set of systems is stabilizable by the proposed controller. Different from the total mass, the damping coefficient variation does have a noticeable effect on the open-loop system gain: it mainly increases or decreases the resonant gain.

3.4.3 Uncertainty in k

Let us assume that all the parameters except the total damping k in the nominal system $G(z^{-1})$ are equal to those of the real system $G'(z^{-1})$, and that k', the total stiffness of $G'(z^{-1})$, is an uncertain value bounded as follows $k' \in [0.75\,k, 1.25\,k]$. This is equivalent to a $\pm 25\%$ variation. The admissible region, (3.30), for $G'(z^{-1})$ is displayed in Fig. 3.13

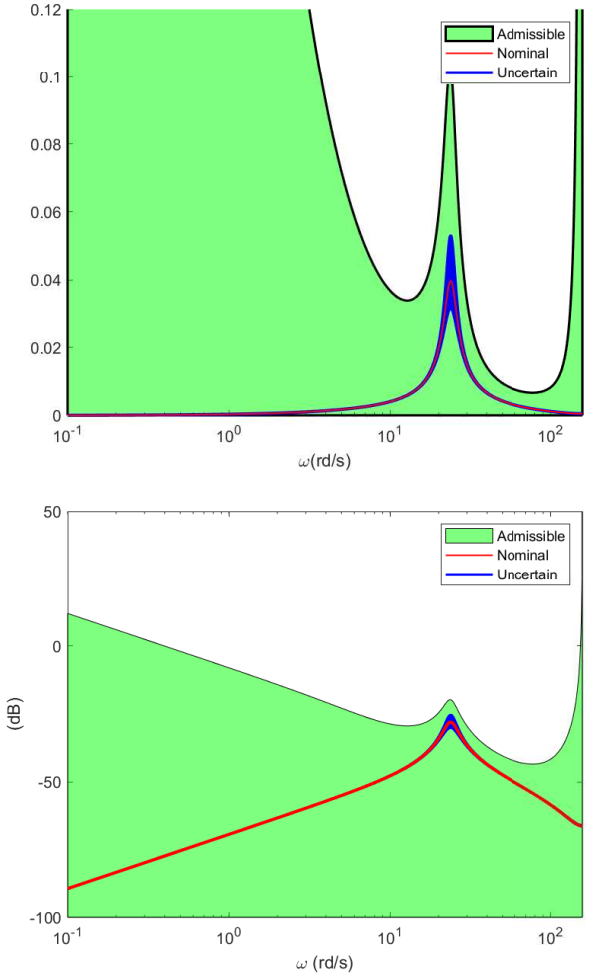

FIGURE 3.12: Nominal system gain $|G(z^{-1})|$ (solid red line), set of open-loop system variations with $c' \in [0.75\,c, 1.25\,c]$ (blue area), and admissible region for $|G'(z^{-1})|$ to be stabilizable (green area) when in closed-loop with (3.27) in natural scale (top) and dB scale (bottom).

[1]. The set of open-loop system variations induced by a 25% of uncertainty in k remains in the admissible region, i.e., the set of systems is stabilizable by the proposed controller. Variations on the total stiffness have a noticeable effect on the open-loop system gain: they push the nominal gain to the sides.

3.4.4 Simultaneous uncertainty in m, c, and k

At last, all three previous parameters will be considered simultaneously uncertain and bounded as follows: $m' \in [0.5\,k, 1.5\,m]$, $c' \in [0.75\,c, 1.25\,c]$, $k' \in [0.75\,k, 1.25\,k]$. This is equivalent to $\pm 50\%$, $\pm 25\%$, and $\pm 25\%$ variations, respectively. The admissible region, (3.30), for $G'(z^{-1})$ is displayed in Fig. 3.14. The set of open-loop system variations

[1]The driveline stiffness can change up to 25% over the total vehicle life cycle [92].

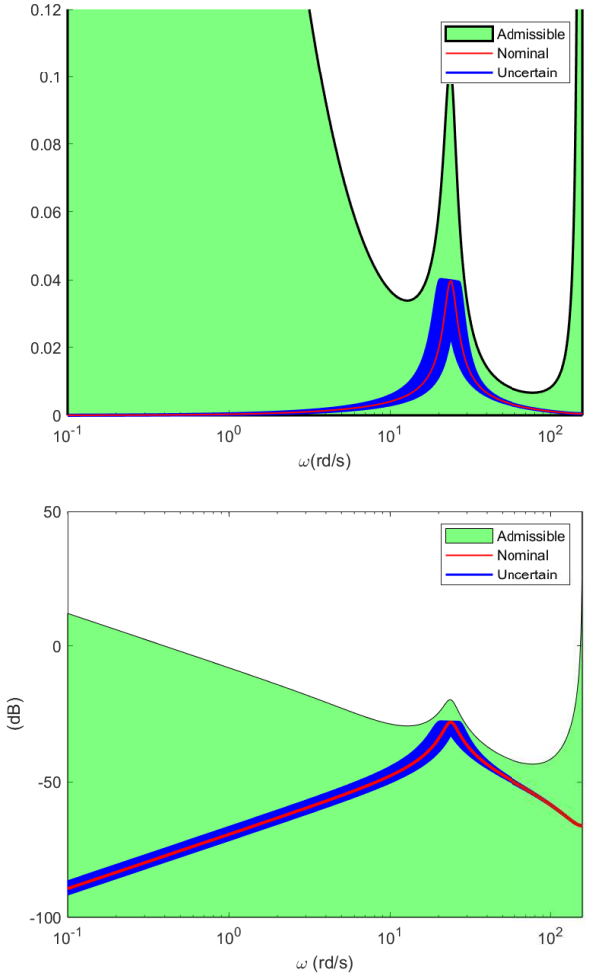

FIGURE 3.13: Nominal system gain $|G(z^{-1})|$ (solid red line), set of open-loop system variations with $k' \in [0.75\,k, 1.25\,k]$ (blue area), and admissible region for $|G'(z^{-1})|$ to be stabilizable (green area) when in closed-loop with (3.27) in natural scale (top) and dB scale (bottom).

induced by the uncertain parameters remains in the admissible region. Nevertheless, there is little space left for further increasing the levels of uncertainty.

3.5 Effect on energy management

The effect on the EMS of the proposed control law is of crucial importance. A proper EMS guarantees that the HEV is able to exploit the extra-degrees-of freedom in order to reduce fuel consumption. Significantly interfering with the EMS is not acceptable for a damping controller. The EMS is derived, as in Chapter 1, from a quasi-static model [23] with a very low bandwidth (typically 0-2 Hz) whereas the oscillations of the side shafts are located above 2 Hz. Coming back to Fig. 1 from Section 3.1. The model parameters, Table 3.1, correspond to the BELHYSYMA prototype [2]. The vehicle uses

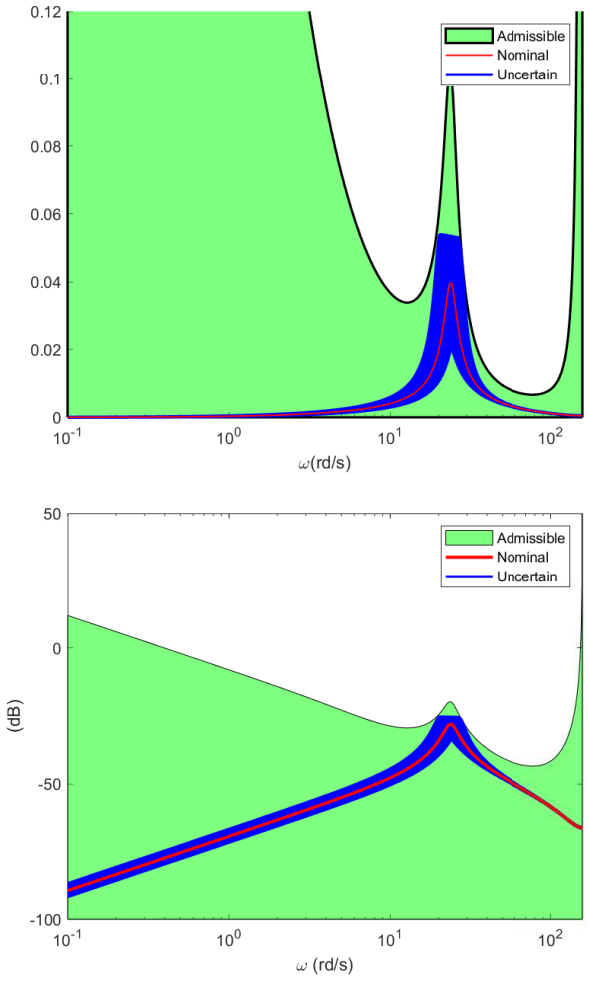

FIGURE 3.14: Nominal system gain $|G(z^{-1})|$ (solid red line), set of open-loop system variations with $m' \in [0.5\,m, 1.5\,m]$, $c' \in [0.75\,c, 1.25\,c]$, and $k' \in [0.75\,k, 1.25\,k]$ (blue area), and admissible region for $|G'(z^{-1})|$ to be stabilizable (green area) when in closed-loop with (3.27) in natural scale (top) and dB scale (bottom).

a 35kW electric machine powered by a 12.5Ah-100V Li-ion battery pack. The electric machine is connected to the ICE in a P0 configuration via a synchronous belt system. The gearbox and the belt system efficiency are assumed to be 1. The clutch control and modeling being out of the scope of this study. The considered driving cycle is chosen to be short and it does not include any gearshift event. This is nevertheless sufficient to evaluate the energetic impact of the damping controller.

3.5.1 EMS formulation

The problem of designing an optimal EMS has been extensively studied over the last decade [105]. The fuel consumption rate $\dot{m}_f\,(T_{ice}, \omega_{ice})$ (g/s) is computed from a lookup

table. The objective functional to be minimized is given by the total fuel consumption:

$$J = \int_0^{t_f} \dot{m}_f \left(T_{ice}\left(t\right), \omega_{ice}\left(t\right)\right) \mathrm{d}t, \tag{3.31}$$

wit t_f (s) the driving cycle length. The battery state of charge dynamics is given by:

$$\dot{x}\left(t\right) = -\frac{1}{Q} I_b\left(T_{em}, \omega_{em}\right), \tag{3.32}$$

with $I_b\left(T_{em}, \omega_{em}\right)$ (A) the battery current and Q the battery capacity (A·s). The EMS is formulated as follows:

$$\min\ J = \int_0^{t_f} \dot{m}_f \left(T_{ice}\left(t\right), \omega_{ice}\left(t\right)\right) \mathrm{d}t, \tag{3.33a}$$

$$\dot{x}\left(t\right) = -\frac{1}{Q} I_b\left(T_{em}, \omega_{em}\right), \tag{3.33b}$$

$$T_{ice} \in \left[T_{ice}^{\min}(\omega_{ice}), T_{ice}^{\max}(\omega_{ice})\right], \tag{3.33c}$$

$$T_{em} \in \left[T_{em}^{\min}(\omega_{em}), T_{em}^{\max}(\omega_{em})\right], \tag{3.33d}$$

$$T_G = R(i) \cdot \left(T_{ice} + \rho \cdot T_{em}\right), \tag{3.33e}$$

$$\omega_G = \frac{\omega_{ice}}{R(i) \cdot \rho} = \frac{\omega_{em}}{\rho} \tag{3.33f}$$

$$x(0) = x_0, \tag{3.33g}$$

$$x(t_f) = x_f. \tag{3.33h}$$

By solving the static inequalities above for T_{ice} and ω_{ice}, respectively, one gets:

$$\min\ J = \int_0^{t_f} \dot{m}_f \left(T_{ice}\left(t\right), \omega_{ice}\left(t\right)\right) \mathrm{d}t, \tag{3.34a}$$

$$\dot{x}\left(t\right) = -\frac{1}{Q} I_b\left(\frac{1}{\rho}\left(\frac{1}{R(i)} \cdot T_G - T_{ice}\right), R(i)\,\rho \cdot \omega_G\right), \tag{3.34b}$$

$$T_{ice} \in \left[T_{ice}^{\min}(\omega_{ice}), T_{ice}^{\max}(\omega_{ice})\right], \tag{3.34c}$$

$$T_{em} \in \left[T_{em}^{\min}(\omega_{em}), T_{em}^{\max}(\omega_{em})\right], \tag{3.34d}$$

$$x(0) = x_0, \tag{3.34e}$$

$$x(t_f) = x_f. \tag{3.34f}$$

Defining the Hamiltonian associated with the optimal control problem above as follows:

$$H\left(T_{ice}, \lambda, t\right) = \dot{m}_f\left(T_{ice}, R(i) \cdot \omega_G\right) - \frac{\lambda}{Q} I_b\left(\frac{1}{\rho}\left(\frac{1}{R(i)} \cdot T_G - T_{ice}\right), R(i)\,\rho \cdot \omega_G\right), \tag{3.35}$$

the solution can be computed via Pontryagin's Minimum Principle as an equivalent boundary value problem [64]:

$$\dot{x}\left(t\right) = -\frac{1}{Q} I_b \left(\frac{1}{\rho} \left(\frac{1}{R(i)} \cdot T_G - T_{ice} \right), R(i)\, \rho \cdot \omega_G \right), \tag{3.36a}$$

$$\dot{\lambda}(t) = 0, \tag{3.36b}$$

$$x(0) = x_0, \tag{3.36c}$$

$$x(t_f) = x_f, \tag{3.36d}$$

with

$$T_{ice} = \arg\min H\left(T_{ice}, \lambda, t\right). \tag{3.37}$$

The EMS responds to the torque requested by the driver through the throttle pedal. Fig. 3.15 shows a synthetic driving mission (top) along with the torque at the output of the transmission, T_G, (bottom) required to complete such mission. In the following, the following notation will be considered:

- A superscript ^{0} refers to a signal computed in the *ideal* case: $k \to \infty$ and $c = 0$.
- A superscript ^{1} refers to a signal computed with k and c as given in Table 3.1 where damping controller (3.27) is kept off during the whole driving mission.
- A superscript ^{2} refers to a signal computed with k and c as given in Table 3.1 where damping controller (3.27) is active.

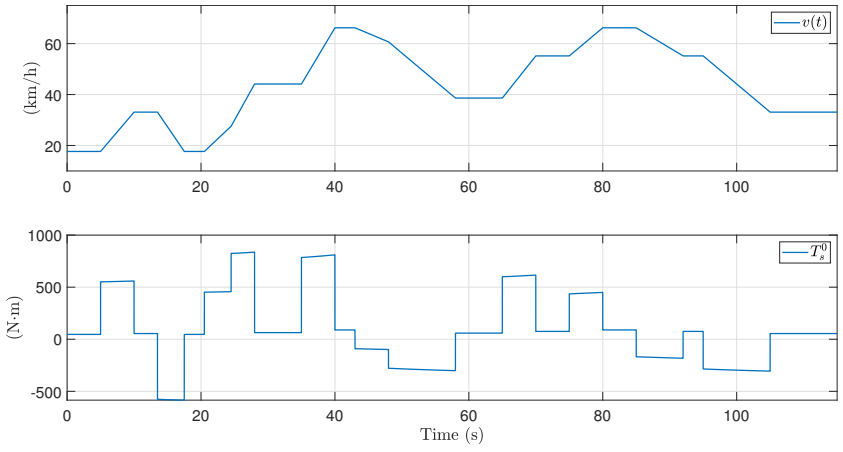

FIGURE 3.15: Top: synthetic driving mission. Bottom: Transmission output shaft torque T_G required to follow the velocity profile under ideal stiffness.

3.5.2 Ideal case

Solving EMS (3.35) under ideal stiffness for $x_0 = x_f = 0.5$ yields a total fuel consumption of 10.3576 l/100km and a state variation of $x(T) - x(0) = -6.32 \cdot 10^{-4}\%$. The state-of-charge trajectory and the power split of this solution are shown in Fig. 3.16.

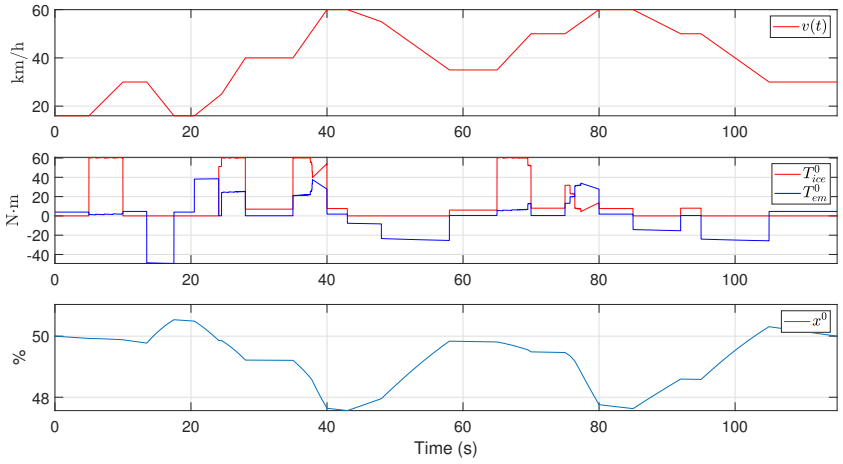

FIGURE 3.16: EMS (3.35) under ideal stiffness. The total fuel consumption is 10.3576 l/100km.

3.5.3 Open-loop case

EMS (3.35) is solved again in open-loop under torsional dynamics for $x_0 = x_f = 0.5$, yielding a total fuel consumption of 10.3657 l/100 km and a state variation of $x(T) - x(0) = 7 \cdot 10^{-3}\%$. The state-of-charge trajectory and the power split are shown in Fig. 3.17.

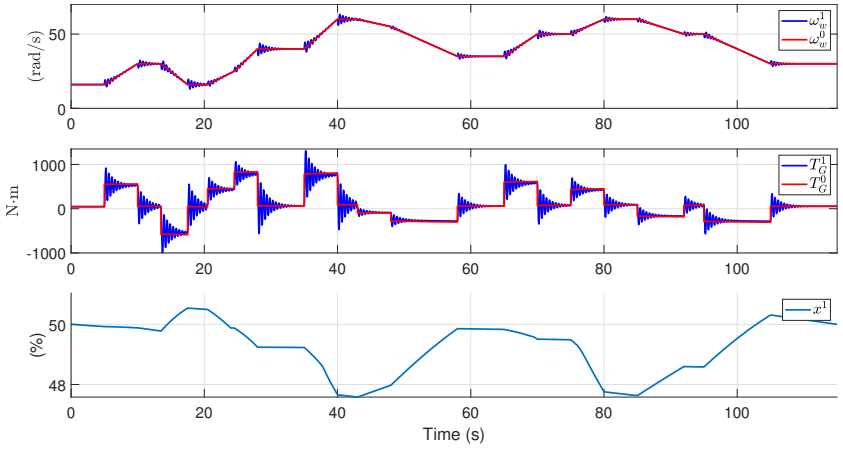

FIGURE 3.17: EMS (3.35) in open-loop and under torsional dynamics. The total fuel consumption is 10.3657 l/100km. RMS value (3.26) equal to 0.734.

3.5.4 Closed-loop case

Now EMS (3.35) is solved under torsional dynamics and the damping feedback controller (3.27) for $x_0 = x_f = 0.5$, yielding a total fuel consumption of 10.3791 l/100 km. The state-of-charge trajectory and the power split are shown in Fig. 3.18.

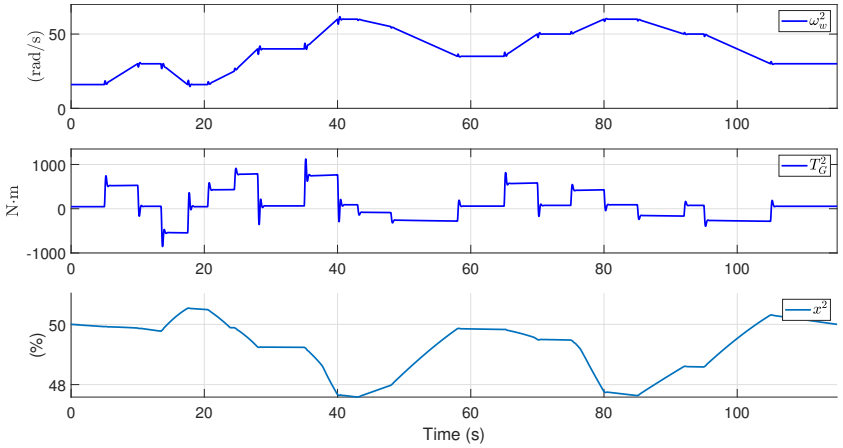

FIGURE 3.18: EMS (3.35) under feedback control law (3.27) and torsional dynamics. The total fuel consumption is 10.3791 l/100km. RMS value (3.26) equal to 0.356.

3.5.5 Fuel-optimal control with active damping

This subsection finds the optimal EMS that achieves the same damping performance of the closed-loop solution. In order to compute this, T_G^2 is used as the reference in a open-loop setting and the optimal power split is found via (3.36a). The solution is given in Fig. 3.19, with a total fuel consumption equal to 10.3757 l/100 km.

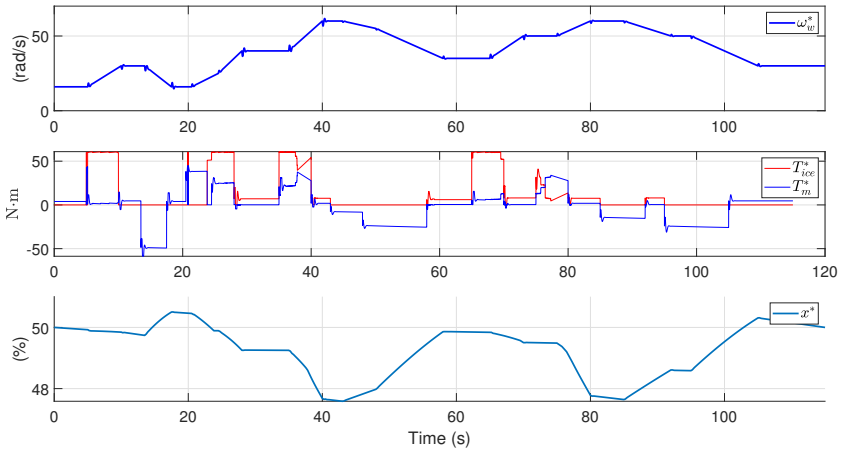

FIGURE 3.19: EMS (3.35) in open-loop with T_G^2 as the torque reference. The total fuel consumption is 10.3757 l/100km. RMS value (3.26) equal to 0.356.

3.5.6 Analysis

	Ideal	Open-loop	Closed-loop	Optimal
Torsional dynamics	No	Yes	Yes	Yes
Torque reference	T_G^0	T_G^0	T_G^0	T_G^2
Controller active	No	No	Yes	No
Fuel consumption (l/100km)	10.3576	10.3657	10.3791	10.3757
Variation with respect to ideal	0%	0.0786%	0.2611%	0.2278%
RMS (3.26)	0	0.734 (100%)	0.356 (48.42%)	0.356 (48.42%)

TABLE 3.2: Summary of the simulation results carried out to study the energetic effect of the damping controller. All the simulations have the same initial and final state-of-charge.

The results for the four previous cases are summarized in Table 3.2. The damping control law significantly reduces the oscillations, up to 51.58%, at the cost of a small fuel consumption increase, 0.26%. Moreover, the optimal EMS with identical damping performance, which is not implementable in real-life, has an increase in total fuel consumption of 0.23 %. It is worth noticing, that in addition to the control law having an insignificant impact on the total fuel consumption, the considered driving mission was been chosen to include several steep edges, 20, over a short period of time: 115s. This is a pessimistic or worst case scenario setting since these conditions are unlikely to happen in real life. In practice, the average fuel consumption increase could be even more limited.

3.6 Experimental results

FIGURE 3.20: BELHYSYMA prototype [2]. The HEV used for experimental validation.

The controller design is now validated on real-time experiments carried out in the BEL-HYSYMA prototype [2]. The vehicle is depicted in Fig. 3.20. Experimental results are shown in Fig. 3.21 with the second gear engaged ($R(i) = 8.89$). The ICE and EM torques are shown at the top. The measured torsional speed $\Delta\dot{\theta}$ is displayed at the middle. The total EM torque setpoint, T_{em}, and the measured torque, $\check{T}_{em}$, are displayed at the bottom. The red and green backgrounds at the middle of the figure indicate when the damping controller remained off and on, respectively. The RMS values, (3.26), are 0.44 and 0.634 with and without the damping controller: a 30.63% reduction. Designing control law (3.27) for $R(i) = 16.45$ (first gear engaged), the experimental results of the control law are displayed in Fig. 3.22. In this case $T_{em}(t)'$ is set to zero and the torque variations are provided solely by T_{ice}. The RMS values, (3.26), are 0.296 and 0.418 with and without the damping controller: a 29.33% reduction. Modifying

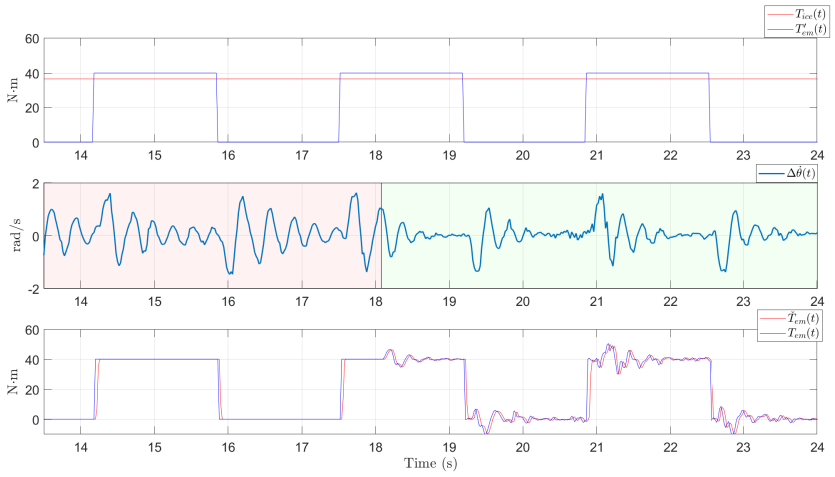

FIGURE 3.21: Top: ICE and EM torque setpoints. Middle: measured torsional speed $\Delta\dot{\theta}$. Bottom: total EM torque setpoint, T_{em}, and the measured torque, $\check{T}_{em}$. The RMS values, (3.26), are 0.44 and 0.634 with and without the damping controller: a 30.63% reduction. The experiment was carried out with the second gear engaged: $R(i) = 8.89$. The red and green backgrounds at the middle of the figure indicate when the damping controller remained off and on, respectively.

control law (3.27) to remove the low-pass filter and considering $R(i) = 8.89$ (second gear engaged), the right subfigure in Fig. 3.23 shows the experimental results of the control law and compares it to the original control law (left subfigure). Although both control laws effectively damp the oscillations, the one without high-frequency noise attenuation is negatively affected by noise: (1) it has a higher frequency and a larger amplitude, this could unnecessarily accelerate the wear down of the EM; (2) it has a worse damping performance: 25.86% against 30.63% achieved when a low-pass filter is included in the controller. From all the experimental results, it can be concluded that the damping controller effectively reduces the driveshaft oscillations and that it tends to vanish when the torsional dynamics tends to its steady state. Therefore, the controller

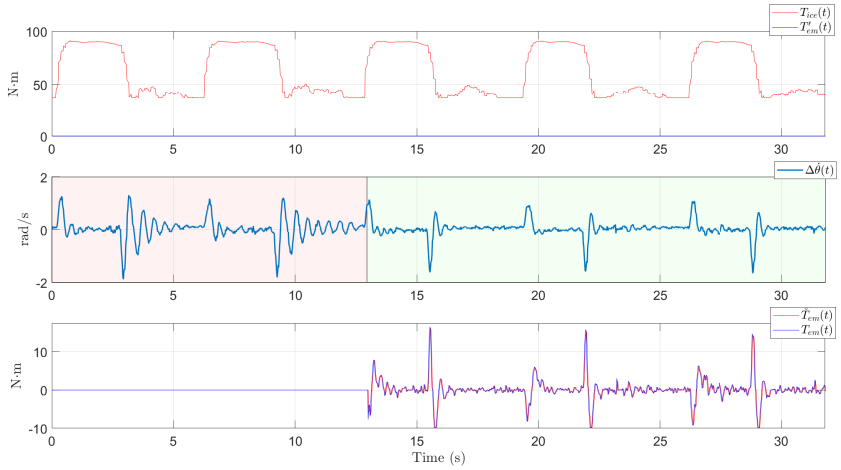

FIGURE 3.22: Top: ICE and EM torque setpoints. Middle: measured torsional speed $\Delta\dot{\theta}$. Bottom: total EM torque setpoint, T_{em}, and the measured torque, $\check{T}_{em}$. The RMS values, (3.26), are 0.296 and 0.418 with and without the damping controller: a 29.33% reduction. The experiment was carried out with the first gear engaged: $R(i) = 16.45$. The red and green backgrounds at the middle of the figure indicate when the damping controller remained off and on, respectively.

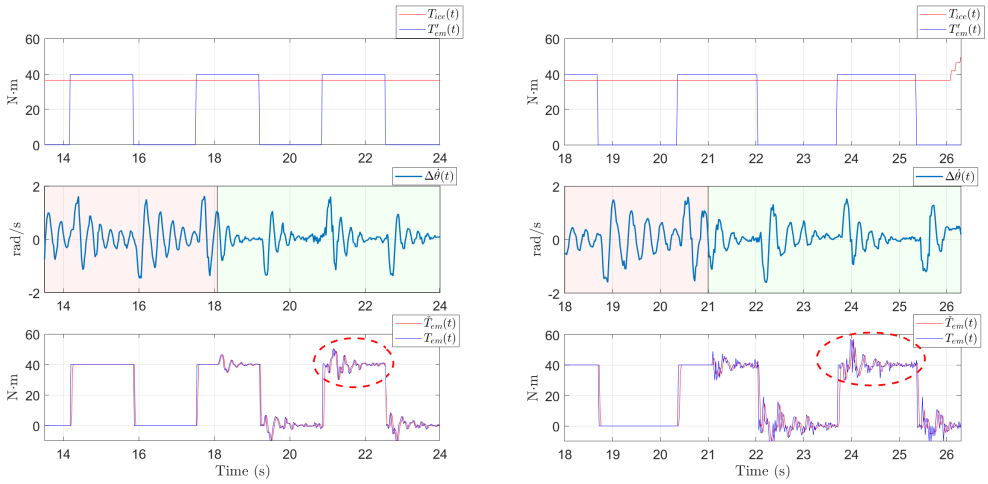

FIGURE 3.23: Left: experimental results with damping controller as designed in Section 3.3, (3.27). Right: experimental results with the damping controller modified such that the low-pass filter is removed from its structure. The experiments were carried out with the second gear engaged: $R(i) = 8.89$. The red and green backgrounds at the middle of the figure indicate when the damping controller remained off and on, respectively.

successfully delivers on the control objectives established in Section 3.3. The difference in performance between the experimental results and those obtained in simulation might be due to several reasons, such as, unmodeled dynamics and the presence of noise and quantization in the measured signals.

3.7 Conclusions

A control law for driveshaft oscillations damping has been designed via a discrete RST approach. The dynamics used for its design are based on a P_0 parallel HEV and includes time-delays induced by the CAN bus. The control law is shown to be robust with respect to parametric uncertainty. Regarding the effect of this control law on the energy management, it is found that its effect on the EMS is very limited: a +0.26% increase in total fuel consumption. This is obtained for a synthetic driving mission designed to have a high number of steep torque changes in a short period of time (an scenario unlikely to occur in real-life). This is achieved by designing the control law with a vanishing behavior whenever the system tends to steady-state. The control law is validated via experimental results where up to 30% of oscillations reduction is achieved. Although these results validate the ability of the designed controller to damp the drivelshaft oscillations, it might be possible to further improve its performance if a more accurate model dynamics is considered and/or if measurement quantization is taken into account. The effect of quantization in the measured signals comes mainly from the measured speed at the wheels since the sensor used for this signal has a very low resolution. By conceiving an appropriate model of the clutch, another possible way to extend the present work is to include oscillations induced during gearshifting.

Chapter 4

Powertrain system architecture design

4.1 Introduction

The increasing interest on hybrid vehicle technology within the automotive sector has lead researchers and engineers into seeking not only a methodical way to solve the energy management strategy (EMS) but also a way to find the optimal powertrain configuration.

When designing hybrid electric vehicles, automakers have to conceive a powertrain configuration able to meet a set of requirements. Among these requirements, there are:

- performance requirements, e.g., maximum acceleration, maximum speed, range,
- government regulation requirements such as fuel consumption, CO_2 emission and pollution,
- maximum cost requirements,
- manufacture requirements,
- technology requirements,
- specific design requirements, e.g., not to use a configuration/architecture patented by a competitor, and
- time requirements.

All these restrictions are inherently linked to each other. Clearly, optimizing under that many complex restrictions in order to compute the best powertrain configuration is a

truly difficult problem. Several approaches have been proposed in the literature to help solve this task.

In [5], a fixed library of 15 elements, with 8 unique components (see Table 4.1), is build and each possible architecture is defined as an undirected graph (each component is represented by a node and each connection is represented by an edge). The total number of possible undirected graphs (architectures) is equal to $5.7 \cdot 10^{45}$. However, this number includes architectures that lack any practical meaning or that are simply not hybrid powertrains. The problem of generating *feasible* hybrid topologies under this undirected graph formulation is solved by imposing 57 constraints implemented via constraint logic programming (CLP). A total of 4779 are obtained in this manner. By means of automatic model generation, optimization over the set of feasible architectures is carried out via nonlinear optimization algorithms, such as, SQP, Particle Swarm Optimization, and Genetic Algorithms [106].

Number	Name	Number of instances
1	ICE	1
2	Electric machine	2
3	Gearbox	1
4	Planetary gear set	2
5	Differential/wheels	1
6	Clutch	3
7	Brake	3
8	Mechanical node	3

TABLE 4.1: Library of components considered in [5].

In [4], a similar graph representation and CLP, with a set of only 9 constraints, is applied to generate feasible topologies from a library of 14 elements with 6 unique components (see Table 4.2). One important difference between this approach and the one presented in [5] is that instead of Planetary Gear Sets (PGS), synchronizer units (gearboxes) are used to build series-parallel architectures as is done in [107]. Another important difference is that once the set of architectures that satisfy the 9 constraints has been solved via CLP, filtering steps are applied to further discard architectures that are either *functionally* identical among each other or that do not comply with basic performance constraints. These filtering steps are taken before analyzing the energetic performance of the architectures and, thus, they provide the advantage of reducing the computation time of the optimization routine but they can also reduce the effort of designing and programming tens of constraints. The sizing of the ICE and the EMs is linearly scaled from their reference models; this includes the minimum and maximum torques, the loss maps and the weights. The inertia of the rotating components is computed by taking

the scale factor to the power of 5/3. One limitation of this approach is that the bi-level optimization (the optimization of the sizing and the EMS) of a single architecture takes around 8-10 hours.

Number	Name	Number of instances
1	ICE	1
2	Electric machine	2
3	Final drive	1
4	Shaft	4
5	Clutch	3
6	Synchronizer unit	3

TABLE 4.2: Library of components considered in [4].

Yet another recent work that relies on fixing a library of components and imposing restrictions via CLP to obtain feasible architectures can be found in [108]. There, 174 constraints are implemented in around 4,600 lines of code. Additional filtering steps are also performed, allowing to reduce the total design space from $2.5 \cdot 10^{27}$ to 635 topologies. The generation of the topologies using Prolog takes 5 hours. The filtering steps needed to further reduce the design space down to 635 topologies takes 20 hours. One important difference with respect to the previously discussed works is that the transmission elements are belt continuously variable transmissions (CVTs).

The same tendency of analyzing the set of topologies directly on terms of its functionality instead of their topological structure has been followed in other recent works. For instance, in [57], the space design is reduced from 10^8 down to a 10^5 possible designs by means of an approach that looks directly into the modes before building topologies. In fact, there it is concluded that only 3476 unique modes can be obtained from the library of components. The library includes, as fixed elements, 3 PGS, 1 ICE, and 2 EMs. The topology design problem consists in placing up to 3 clutches and up to 3 permanent connections among the sun and ring gears of the 3 PGS. In order to improve the computation time of the approach, the EMS is computed by a sub-optimal technique called PEARS [109]. No sizing or parametrization is included in the approach. After 15 hours of computation, the *mode combination* approach is able to find 173 topologies that comply with a given set of performance requirements.

At the cost of a reduced accuracy, convex models can be computed from the static maps. With this, standard convex problem formulations of the EMS are possible, such as linear programming (LP), quadratic programming (QP), second-order cone programming (SOC), or semi-definite programming (SDP). The advantages of a convex problem formulation are a guarantee of global optimality and the existence of algorithms able to solve the problem in polynomial time. The main disadvantage of their use for solving the EMS is that the introduction of integer variables transforms them into mixed-integer problems, which are non-convex NP-hard problems in general. Nonetheless, convex optimization has allowed computing the Complete Vehicle Energy Management (CVEM) of a hybrid truck under a driving mission of 55795 seconds by means of a distributed convex optimization approach [42]. There, the powertrain together with the auxiliaries or hotel load components are seen as a power network whose components interact under conservation of power principles, giving place to a 5-state EMS formulation. When integer variables such as the on/off signal of the engine or the gearshifting are included in the convex EMS formulation, one possible solution explored in the literature is to consider a heuristic sub-optimal approach for the on/off command of the ICE [110]. The heuristic consists in solving the EMS with a relaxed binary signal and then to set the binary signal to zero whenever the ICE output power is below a threshold value (also done in [111] and [112], where it is shown to be optimal according to PMP). This routine is embedded in a bisection algorithm that seeks the feasible EMS with the higher threshold value, i.e., the aim is to maintain the ICE off as much as possible. The convex formulation is based on linear programming. Another solution that, in addition to the on/off signal, also optimizes the gearshifting signal was presented in [59]. Its proposal consists in optimizing the discrete variables iteratively in an outer loop that has as input the solution of the EMS with fixed discrete signals. One important remark on this work is that the optimality of the discrete EMS can be established, at least with a certain level of accuracy.

Moreover, convex optimization, SOCP, has been successfully used to compute the **EMS** and the **optimal sizing** of the **main components** for different plug-in hybrid powertrain architectures, i.e., series [111, 113], parallel [45], and fuel-cell [114, 115]. The same technique has been also applied to non plug-in HEVs [116, 117]. The germinal paper that preceded these works only considered sizing the battery pack [113]. This was later extended to including sizing of EMs, ICEs, APUs, supercapacitor stacks [116, 117], and fuel-cells. For instance, in [115], the total ownership cost is minimized for a fuel-cell plug-in HEV propelled by a single EM by assuming a given lifetime. All the latter results rely on the assumption that the most relevant characteristics of the main powertrain components can be linearly scaled from their baseline models. Contrary to [4], in these works, the moment of inertia is not scaled (it is neglected altogether).

4.1.1 Motivation

The flexibility of the modeling framework presented in [42], together with the short computation times achieved by state-of-the-art convex solvers, and the tendencies of studying HEV architectures directly on terms of their functionality, as seen in [57] and [4], have inspired us to conceive a convex architecture optimization approach that can compute the optimal architecture and solve the EMS simultaneously. The approach is based on Mixed-Integer Linear Programming (MILP). The main hypothesis taken when formulating this approach is that cutting-edge Mixed-Integer solvers such as Mosek [118] and Gurobi [119] are able to solve, relatively quickly, problem formulations big enough to be of practical interest for architecture optimization of HEV.

4.1.2 Contribution

The topology optimization methodology presented here is a novel simultaneous approach based on (1) the modeling framework from [42]: the objective function to be minimized is the total power loss across the power network, the components have piecewise linear loss models [43], the connection among the components is done through nodes that are subject to power conservation constraints; (2) connectivity constraints based on graph theory, similarly to [4, 5] , which determine how many edges (connections) each component has: either it is present in the network and thus all its edges are connected or it is not present and thus none of its edges is connected, and whether the edges can be connected at the same node: electrical edges and mechanical edges cannot be connected to the same node; and (3) linearization constraints which relax the product of binary and continuous variables, as it is done in [58]. The contribution of the our proposal can be summarized in the following two observations:

- By applying basic principles, the simultaneous approach is able to optimize over the space design of functional topologies without requiring the expert knowledge and the programming effort done in previous works such as [108], where up to 174 constraints were written in about 4,600 lines of code.
- Thanks to the capabilities of cutting-edge convex solvers, such as GUROBI and Mosek, the methodology presented here is able to solve the simultaneous optimization problem relatively quickly despite the constraint of having an NP-hard problem formulation (MILP).

The developed technique can be applied or extended to other energy network design problems as well (e.g. smart city grid network optimizing, local energy storage, and the

connection of plug-in vehicles whose state dynamics vary while being connected to the grid). This work is focused on HEVs as a proof of concept. As it has been previously done in the literature, the first step taken was to define a library of components. In this case, all the components are single-input single-output and have piecewise linear loss models computed, for example, from the brake-specific fuel consumption (bsfc) for the case of the ICE or from the efficiency maps for the case of the EM. The interaction among the components of the network is carried out by nodes, which are constrained to obey basic principles:

- *the conservation of power*: the sum of all the power signals going to a node is equal to zero at all time instant.
- *the separation of layers*: a mechanical and a electrical edge cannot be connected to the same edge, i.e., the interaction of power signals of different nature requires the presence of a conversion component.

4.1.3 Organization

The rest of the chapter is organized as follows: Section *Convex Models*, details how the piecewise linear models are computed for each of the components in the library; Section *Model Validation* shows that the accuracy lost by using convex models is not considerable when compared to the original nonlinear maps; Section *Simultaneous Optimization Framework* contains the main results of the chapter; Section *Case Study* presents an application of the methodology; Section *Conclusions* closes the chapter with important observations and possible future-work extensions on the proposed approach.

4.2 Convex Modeling

The set of elements modeled in the proposed approach are ICEs, EMs, and battery packs. They are modeled as single-input single-output power storage/conversion/transmission elements subject to piecewise linear loss models. The rest of the components on the powertrain are considered ideal: they allow the main powertrain components to operate in their most efficient region.

4.2.1 Internal combustion engine

In a internal combustion engine, the efficiency depends on the torque and angular velocity, (T_{ICE}, ω_{ICE}) pair. The efficiency map for an ICE is shown in figure 4.1.

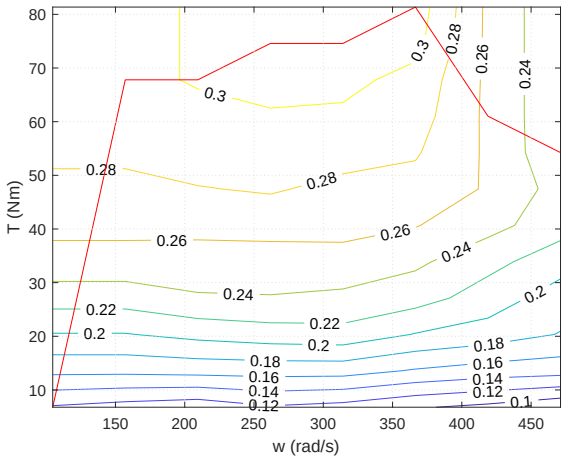

FIGURE 4.1: Contour curves for the efficiency map of an ICE.

In this research, we would like to focus in the analysis of power flows. Thus, we are not interested in the torques and velocities of the ICE: an optimal efficiency model will be used instead. The optimal efficiency model is computed by finding the best efficiency achievable for each admissible output power, $\eta^*\left(P_{ice,out}\right)$. Namely, it is computed as the solution of the following optimization problem parametrized by $P_{ice,out}$:

$$\min_{T_{ICE},\omega_{ICE}} \; -\eta\left(T_{ICE},\omega_{ICE}\right) \tag{4.1a}$$

subject to:

$$T_{ICE}\omega_{ICE} = P_{ice,out}, \tag{4.1b}$$

$$T^{min}(\omega_{ICE}) \leq T_{ICE} \leq T^{Max}\left(\omega_{ICE}\right) \tag{4.1c}$$

$$\omega_{ICE}^{min} \leq \omega_{ICE} \leq \omega_{ICE}^{max} \tag{4.1d}$$

This is solved for several values of $P_{ice,out} \in \left[P_{ice,out}^{min} P_{ice,out}^{max}\right]$. Once $\eta^*(P_{ice,out})$ has been computed, an affine approximation of $P_{ice,inp}$-$P_{ice,out}$ can be computed:

$$P_{ice,out} = \eta^*(P_{ice,out}) \cdot P_{ice,inp} \approx a_{ICE} P_{ice,inp} + b_{ICE}. \tag{4.2}$$

The affine approximation and the measured values for $P_{ice,inp}$-$P_{ice,out}$ are shown in figure 4.2. A more detailed perspective on the accuracy of the approximation can be obtained by plotting the $P_{ice,inp}$-η^* curve. The approximation of η^* can be computed from (4.2):

$$\eta^*(P_{ice,out}) \approx \frac{a_{ICE} P_{ice,inp} + b_{ICE}}{P_{ice,out}} = a_{ICE} + b_{ICE}/P_{ice,inp} \tag{4.3}$$

The $P_{ice,inp}$-η^* curve is shown in figure 4.3. The approximation fails to predict an efficiency peak after $P_{ice,out} = 60$ (kW). The convex region used to model the ICE losses is shown in Fig. 4.4.

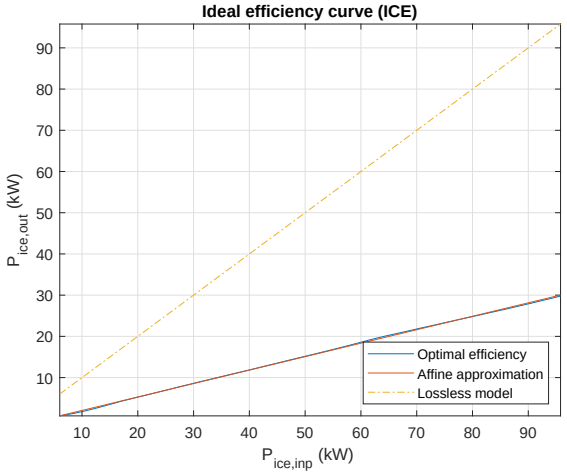

FIGURE 4.2: Optimal $P_{ice,\,inp}$-$P_{ice,\,out}$ curve; its affine approximation, (4.2), with $a_{ICE} = 0.3264$ (-), $b_{ICE} = -1.2364 \cdot 10^3$ (W); and the ideal curve.

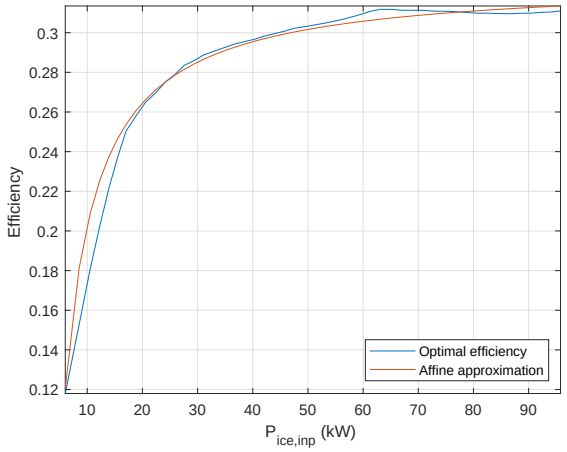

FIGURE 4.3: Optimal curve $P_{ice,\,inp} - \eta^*$ and its affine approximation.

4.2.2 Electric machine

The efficiency of an electric machine depends on its torque and angular speed, (T_{EM}, ω_{EM}) pair. The efficiency map of an electric machine is shown in figure 4.5. As it was done for the ICE, an optimal efficiency model will be computed via solving the following optimization problem parametrized by $P_{EM,\,out}$:

$$\min_{T_{EM},\omega_{EM}} \quad -\eta\left(T_{EM}, \omega_{EM}\right) \tag{4.4a}$$

subject to:

$$T_{EM}\omega_{EM} = P_{EM,\,out}, \tag{4.4b}$$

$$0 \leq T_{EM} \leq T^{Max}\left(\omega_{EM}\right), \tag{4.4c}$$

$$\omega^{min} \leq \omega_{EM} \leq \omega^{Max}. \tag{4.4d}$$

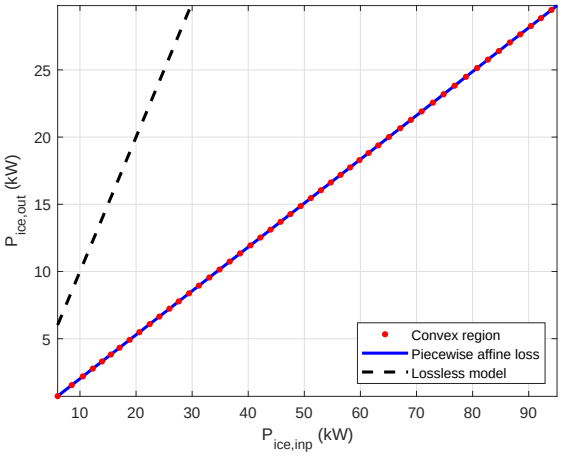

FIGURE 4.4: Affine approximation (4.2) (blue line); convex region described by (4.2) (red dots); the optimal curve $P_{ice,\,inp} - P_{ice,\,out}$ (dashed lines).

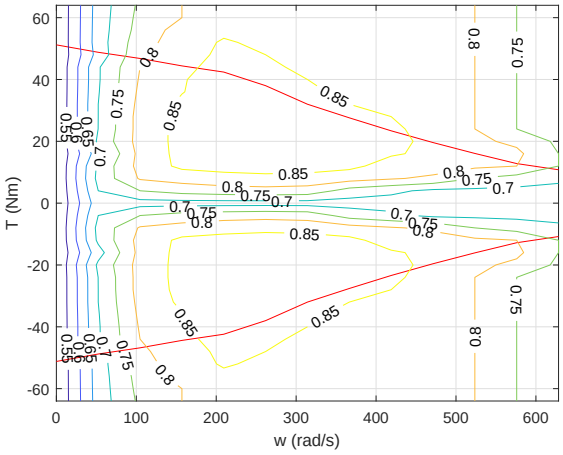

FIGURE 4.5: Contour curves for the efficiency map of an EM ($\eta_{EM}(T_{EM}, \omega_{EM})$).

This is solve for several values of $P_{EM,\,out} \in \left[P^{min}_{EM,\,out}, P^{max}_{EM,\,out}\right]$. The optimal $P_{EM,\,inp}$-$P_{EM,\,out}$ relationship can be approximated on the interval $P^{+}_{EM,\,out} = \left[0, P^{\max}_{EM,\,inp}\right]$ with an affine function as follows:

$$P_{EM,\,out} = \eta^*(P_{EM,out}) \cdot P_{EM,inp} \approx a_{EM} P_{EM,\,inp} + b_{EM}. \tag{4.5}$$

For the EM studied above, the measured optimal efficiency relation $P_{EM,\,inp} - P_{EM,\,out}$ is shown in figure 4.6. The affine approximation of the optimal $P_{EM,\,inp} - P_{EM,\,out}$, (4.5), curve is shown in the same figure. More details about the approximation are noticeable if we look at the $P_{EM,\,inp} - \eta^*$ curve: from the efficiency map, described as follows:

$$\eta^*\left(P_{EM,\,out}\right) \approx \frac{a_{EM} P_{EM,\,inp} + b_{EM}}{P_{EM,\,inp}} = a_{EM} + b_{EM}/P_{EM,\,inp}. \tag{4.6}$$

The optimal $P_{EM,\,inp} - \eta^*$ curve and its linear approximation are displayed in figure 4.7. The approximation is close to the measured data curve. However, it does not capture

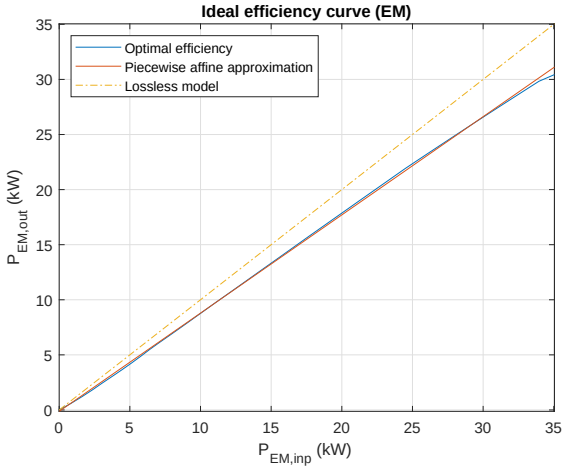

FIGURE 4.6: Optimal $P_{EM,\,inp}$-$P_{EM,\,out}$ curve for $P_{EM,\,inp} \geq 0$; its affine approximation, (4.5), with $a_{EM} = 0.892$, $b_{EM} = -46.7012$; and the ideal curve.

the fact that the efficiency starts to drop when the input power goes beyond 25 kW. Although (4.6) is only fitted for $P_{EM,\,inp} \in P^{+}_{EM,\,inp}$, the symmetry of $\eta^*(P_{EM,\,out})$ can be used to build an affine piecewise approximation for $P_{EM,\,out}$ on its whole range as follows:

$$P_{EM,\,out} = \begin{cases} a_{EM}\, P_{EM,\,inp} + b_{EM}, & P_{EM,\,inp} \geq 0 \\ \frac{1}{a_{EM}} P_{EM,\,inp} + b_{EM}/a_{EM} & P_{EM,\,inp} < 0 \end{cases} \tag{4.7}$$

Piecewise affine model (4.7) has a discontinuity at $P_{EM,\,inp} = 0$ and is not convex. If

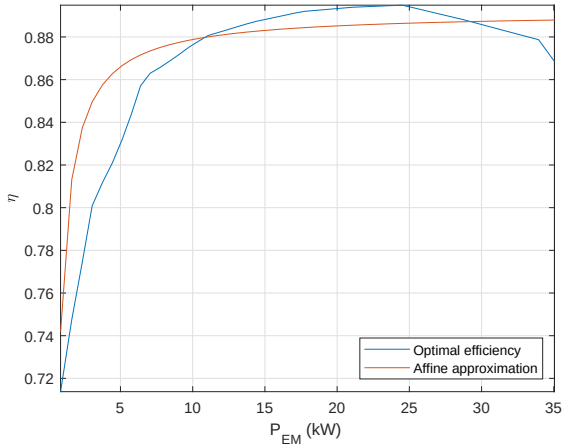

FIGURE 4.7: Optimal curve $P_{EM,\,inp}$–η^* and its affine approximation for $P_{EM,\,inp} \geq 0$.

affine approximation (4.5) on $P_{EM,\,inp} \in P^{+}_{EM,\,inp}$ is replaced by a linear approximation:

$$P_{EM,\,out} = \eta^*\left(P_{EM,\,out}\right) \cdot P_{EM,\,inp} \approx a_{EM} P_{EM,\,inp}, \tag{4.8}$$

a piecewise linear approximation can be computed for the whole range of $P_{EM,\,inp}$ as follows:

$$P_{EM,\,out} = \begin{cases} a_{EM}\, P_{EM,\,inp}, & P_{EM,\,inp} \geq 0 \\ \frac{1}{a_{EM}} P_{EM,\,inp} & P_{EM,\,inp} < 0 \end{cases} \tag{4.9}$$

(4.9) is convex. Therefore, it can be used in a convex optimization approach with inequality constraint relaxations. Nevertheless, a more accurate model is sought. Let us consider the minimum loss curve, computed as:

$$Loss^*_{EM} = P_{EM,inp} - P_{EM,out} = P_{EM,inp} - \eta^* \left(P_{EM,out}\right) \cdot P_{EM,inp}. \tag{4.10}$$

The minimum loss curve is shown in Fig. 4.8a (blue dashed line) along with its quadratic approximation computed as (green solid line):

$$Loss^*_{EM} = P_{EM,inp} - \eta^* \left(P_{EM,out}\right) \cdot P_{EM,inp} \approx a'_{EM} \cdot P^2_{EM,inp} + b'_{EM} \cdot P_{EM,inp} + c'_{EM}, \tag{4.11}$$

then defining:

$$Loss_{EM} = P_{EM,inp} - P_{EM,out} = a'_{EM} \cdot P^2_{EM,inp} + b'_{EM} \cdot P_{EM,inp} + c'_{EM}, \tag{4.12}$$

we get the following:

$$P_{EM,out} = a_{EM} \cdot P^2_{EM,inp} + b_{EM} \cdot P_{EM,inp} + c_{EM}, \tag{4.13}$$

with $a_{EM} = -a'_{EM}$, $b_{EM} = 1 - b'_{EM}$, and $c_{EM} = -c'_{EM}$. The expression above can be relaxed to an inequality in order to include the EM model in an SOCP. Alternatively, piecewise affine functions can be used to approximate the original quadratic convex function with an arbitrary accuracy, see red solid line in Fig. 4.8a. The convex region contained below the affine piecewise model is given as follows:

$$P_{EM,out} \leq a_i P_{EM,inp} + b_i, \qquad i \in \{1, 2, \ldots, n\} \tag{4.14}$$

For the EM considered in this section, the convex region enclosed by (4.14) is shown in Fig. 4.8b with $n = 4$.

4.2.3 Battery pack

Let us consider the zero-order equivalent circuit battery model displayed in Fig. 4.9, with E (V) the open-circuit voltage, R (Ω) the equivalent internal series resistor, and U_{batt} (V) the actual voltage at the battery terminals. The battery is discharging when I_{batt} flows in a clockwise sense and is charging when I_{batt} flows in the opposite sense,

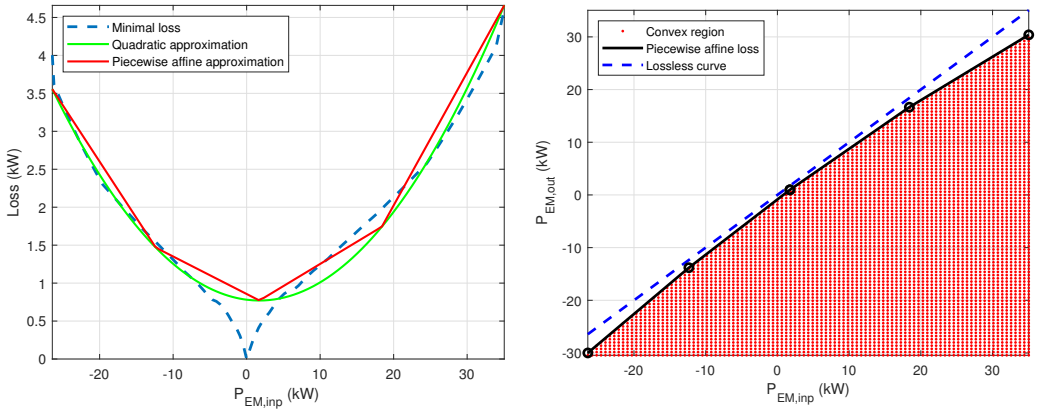

(A) (B)

FIGURE 4.8: A: Minimal loss (4.11) (blue dashed line), quadratic approximation (4.13) (green solid line), and piecewise affine approximation with $n = 4$ affine models (red solid line). B: Piecewise model (4.9) (black solid curve); convex region described by (4.14) with $n = 4$ (red dots); the lossless curve (blue dashed line).

thus, we have the following convention:

$$P_{batt,out} \geq 0 \text{ (when the battery is discharging)},$$
$$P_{batt,out} < 0 \text{ (when the battery is charging)},$$

with $P_{batt,out} = I_{batt} \cdot U_{batt}$, and where I_{batt} is positive when it goes in a clockwise sense. Applying Kirchhoff's voltage law in a clockwise sense on the battery circuit we have:

$$-E + R \cdot I_{batt} + U_{batt} = 0,$$

multiplying both sides of the equation by I_{batt} one gets:

$$-I_{batt} \cdot E + R \cdot I_{batt}^2 + I_{batt} \cdot U_{batt} = 0,$$

defining $P_{batt,inp} = I_{batt} \cdot E$:

$$-P_{batt,inp} + \left(\frac{R}{E^2}\right)\left(E^2 \cdot I_{batt}^2\right) + P_{batt,out} = 0,$$
$$-P_{batt,inp} + \frac{R}{E^2} P_{batt,inp}^2 + P_{batt,inp} = 0,$$

thus:

$$P_{batt,out} = P_{batt,inp} - \frac{R}{E^2} P_{batt,inp}^2, \tag{4.15}$$

The convex region enclosed by

$$P_{batt,out} \leq P_{batt,inp} - \frac{R}{E^2} P_{batt,inp}^2, \tag{4.16}$$

is displayed on Fig. 4.10 (left). This quadratic convex region is approximated by they region below a set of n piecewise affine functions,

$$P_{batt,out} \leq a_i P_{batt,inp} + b_i, \qquad i \in \{1, 2, \ldots, n\}, \tag{4.17}$$

as it is shown in Fig. 4.10 (right). Using the piecewise affine functions, it is possible to approximate the original quadratic convex region with arbitrary accuracy, see Fig. 4.11.

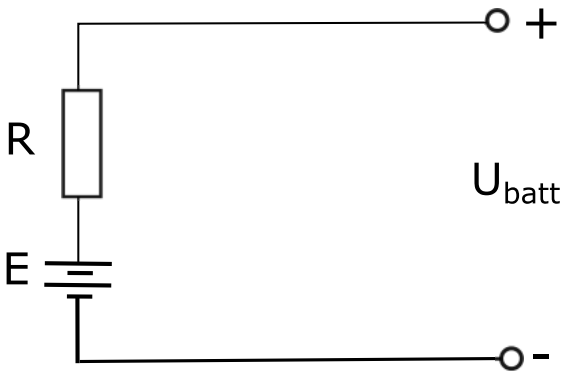

FIGURE 4.9: Diagram of the zero-order equivalent circuit model of the battery pack.

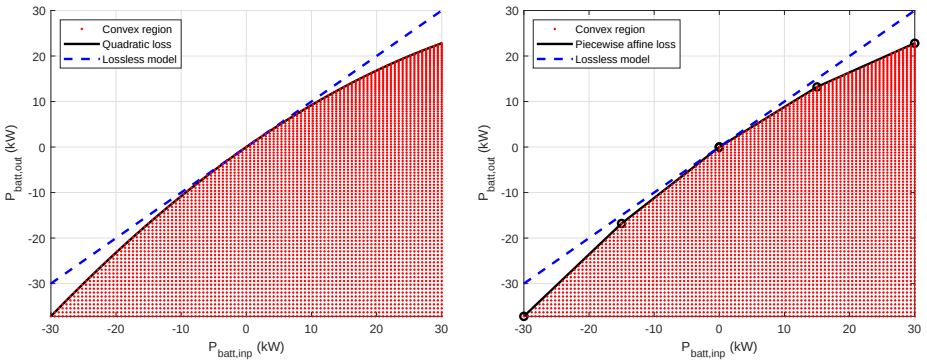

FIGURE 4.10: Quadratic (left) and piecewise (right) input-output models for the battery pack (black lines); the convex regions (red dots); the lossless input-output curve (dashed blue line).

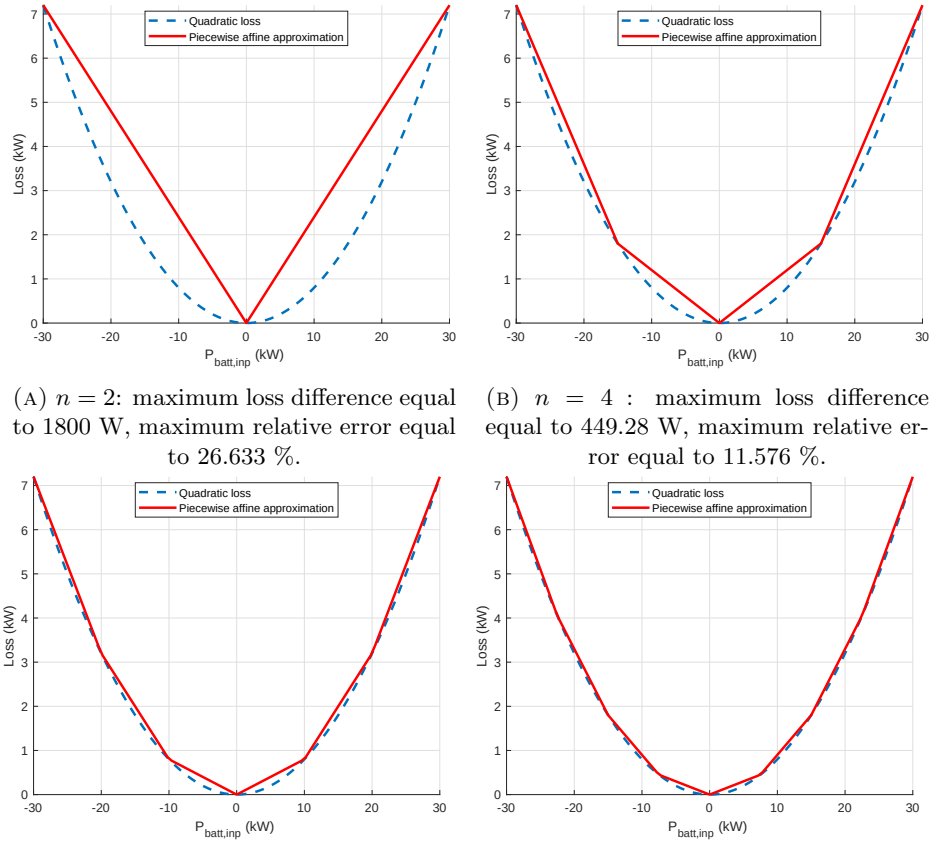

(A) $n = 2$: maximum loss difference equal to 1800 W, maximum relative error equal to 26.633 %.

(B) $n = 4$: maximum loss difference equal to 449.28 W, maximum relative error equal to 11.576 %.

(C) $n = 6$: maximum loss difference equal to 200 W, maximum relative error equal to 7.556 %.

(D) $n = 8$: maximum loss difference equal to 112.32 W, maximum relative error equal to 5.546 %.

FIGURE 4.11: Piecewise approximations for the battery loss model.

4.3 Main Results

This section presents the mathematical framework of the power network modeling. A validation of these modeling by comparing it a more common speed and torque traditional approach in Section 4.3.2 and the main result: a simultaneous EMS and topology optimization approach via MILP in Section 4.3.3.

4.3.1 Mathematical framework

The mathematical framework for the convex optimization problems to be solved will be defined and after that the convex modeling will be validated by comparing it against the DP solution based on the original nonlinear static maps. In order to model the vehicle's powertrain as a power network, let us consider the following assumptions:

Assumption 1. All the electrical and mechanical power transmission elements that are not modeled in the problem formulation are replaced by ideal power transmission elements. We define an ideal power transmission element as a device that

1. transmits power in a lossless way and that
2. allows all the elements that are connected to it to operate in their optimal efficiency regions regardless of their voltage, current, torque, and speed values.

The assumption above allow us to focus on the energetic behavior of the components and to ignore the relation between the efficiency and the speed, torque, current, and voltage. Moreover, the assumption above means that the optimal solution that we compute in this work will be a lower ultimate bound on the optimal energetic performance that can be obtained in the real HEV. Other than the vehicle's ideal power transmission elements, the network is composed of the following elements:

1. an ICE engine (modeled as a power source element),
2. a battery pack (modeled as a power sink/source element),
3. an electric machine (modeled as a electric/mechanical power converter element),
4. the gearbox (modeled as a mechanical element with a constant efficiency),
5. the wheels (modeled as a power sink/source element) that provides the power demand signal to the network.

In the following, the ideal transmission elements will be referred to as nodes.

The objective is operate the network in order to satisfy the power demand (exogenous signal) introduced to the network by the wheels element while minimizing the power losses on the whole network. The objective function takes the following form:

$$J = \sum_{j=1}^{n} \sum_{k=1}^{N_f - 1} P_{m_j,inp}(k) - P_{m_j,out}(k) \tag{4.18}$$

with n the number of elements, N_f the length of the power demand signal, $j = \{1, 2, \ldots, n\}$, and m_j the name of the $j-th$ component of the network. In our case, $n = 3$, $m_j \in \{\text{ice, batt, em, T}\}$. The components are modeled using piecewise loss models of the form:

$$P_{m_j,out}(k) = \min\{a_{m_j,1} \cdot P_{m_j,inp}(k) + b_{m_j,1}, a_{m_j,2} \cdot P_{m_j,inp}(k) + b_{m_j,2}, \ldots, a_{m_j,q_j} \cdot P_{m_j,inp}(k) + b_{m_j,q_j}\}, \tag{4.19}$$

with q_j the number of piecewise linear equations used to model the losses of the j-th element. The convex region enclosed by the convex function above is described by:

$$P_{m_j,out}(k) \leq a_{m_j,i} \cdot P_{m_j,inp}(k) + b_{m_j,i}, \qquad i \in \{1, 2, \ldots, q_j\}. \tag{4.20}$$

for all $k \in \{1, 2, \ldots, N_f\}$, whenever $q_j > 1$ [1]. This relaxation is necessary in order to integrate the pieceiwise affine losses in the convex optimization problem. Although these inequalities include values outside of the loss models, in the optimal solution they are guaranteed to satisfy the inequality constraints since going below these constraints would lead to extra power waste. Inequality constraints are also used to constraint the inputs or outputs of each component:

$$P_{m_j,t}^{\min} \leq P_{m_j,t}(k) \leq P_{m_j,t}^{\max} \tag{4.21}$$

with $t \in \{\text{inp, out}\}$, for all $k \in \{1, 2, \ldots, N_f\}$. Equality constraints represent the connection of the components at a given node. All the nodes observe conservation of power. For instance, the connection between the battery pack and the electric machine at node 3, n_3, will be enforced through the following constraint:

$$P_{batt,inp}(k) - P_{em,inp}(k) = 0, \tag{4.22}$$

for all $k \in \{1, 2, \ldots, N_f\}$, under the convention that $P_{em,inp}$ is extracting power from n_3 and that $P_{batt,inp}$ is providing that power; the presence of a power demand signal or an input or output variable $P_{(.)}$ at the $i-th$ node is

⟨i⟩ 1 if $P_{(.)}$ provides power to the $i-th$ node whenever $P_{(.)} > 0$,

⟨ii⟩ -1 if $P_{(.)}$ extracts power from the node whenever $P_{(.)} > 0$, and

⟨iii⟩ 0 if $P_{(.)}$ has no relation with the node.

In general, for a network with r nodes, the latter is represented by the following equality constraints:

$$\sum_{j=1}^{n} \left[P_{m_j,out}(k) \cdot R_{m_j,out} - P_{m_j,inp}(k) \cdot R_{m_j,inp} \right] + \sum_{l=1}^{p} P_{w_l}(k) \cdot R_{w_l} = 0. \tag{4.23}$$

with $R_{m_j,t}, R_{w_1} \in \mathbb{R}^{r \times 1}$, p the total number of power demand signals in the network, and where the $i-th$ entry of $R_{m_j,t}$ (respectively R_{w_1}) is equal to 1 if and only if $P_{m_j,t}$ (respectively P_{w_l}) is present at the $i-th$ node and zero otherwise; the rest of its entries are equal to zero. In our case, the network only has 3 nodes, $r = 3$, and one power

[1] If $q_j = 1$, the inequality relaxation is not required since a single line is a convex region.

demand signal, $p = 1$, thus, $R_{m_j,t}$ and R_{w_l} are given as follows:

$$R_{ice,inp} = \begin{bmatrix} 0 \\ 0 \\ 0 \end{bmatrix}, R_{em,inp} = \begin{bmatrix} 0 \\ 0 \\ 1 \end{bmatrix}, R_{batt,inp} = \begin{bmatrix} 0 \\ 0 \\ 0 \end{bmatrix}, R_{w_1} = \begin{bmatrix} 0 \\ 1 \\ 0 \end{bmatrix},$$

$$R_{ice,out} = \begin{bmatrix} 1 \\ 0 \\ 0 \end{bmatrix}, R_{em,out} = \begin{bmatrix} 0 \\ 1 \\ 0 \end{bmatrix}, R_{batt,out} = \begin{bmatrix} 0 \\ 0 \\ 1 \end{bmatrix},$$

In addition to input and output power variables, the elements with buffer capabilities have linear dynamics to determine their state-of-energy. The linear dynamics is given as follows:

$$x_{m_s}(k+1) = (\Delta t \cdot A_{m_s} + 1)\, x_{m_s}(k) + \Delta t \cdot B_{m_s,inp} P_{m_s,inp}(k) + \Delta t \cdot B_{m_s,out} P_{m_s,out}(k), \tag{4.24}$$

with m_s the name of the $s-th$ element in the network which posses buffer capabilities, $s \subseteq j$. The states of energy can be subject to path:

$$x_{m_s}^{\min}(k) \leq x_{m_s}(k) \leq x_{m_s}^{\max}(k), \tag{4.25}$$

and boundary constraints:

$$x_{m_s}(1) = x_{m_s}^{0} \tag{4.26a}$$

$$x_{m_s}(N_f) = x_{m_s}^{N_f}. \tag{4.26b}$$

Finally, the optimal control problem for the HEV is formulated as the following Linear Programming (LP) problem:

$$\min_{\mathbf{P}_{m_j,t}} \quad J = \Delta t \cdot \sum_j \sum_k \mathbf{P}_{m_j,inp}(k) - \mathbf{P}_{m_j,out}(k), \tag{4.27a}$$

subject to:

$$\mathbf{P}_{ice,out}(k) \leq a_{ice,i} \cdot \mathbf{P}_{ice,inp}(k) + b_{ice,i}, \qquad i \in \{1, 2, \ldots, q_1\} \tag{4.27b}$$

$$\mathbf{P}_{em,out}(k) \leq a_{em,i} \cdot \mathbf{P}_{em,inp}(k) + b_{em,i}, \qquad i \in \{1, 2, \ldots, q_2\} \tag{4.27c}$$

$$\mathbf{P}_{batt,out}(k) \leq a_{batt,i} \cdot \mathbf{P}_{batt,inp}(k) + b_{batt,i}, \qquad i \in \{1, 2, \ldots, q_3\} \tag{4.27d}$$

$$\mathbf{P}_{T,out}(k) \leq a_{T,i} \cdot \mathbf{P}_{T,inp}(k) + b_{T,i}, \qquad i \in \{1, 2, \ldots, q_4\} \tag{4.27e}$$

$$\mathbf{P}^{\min}_{ice,out} \leq \mathbf{P}_{ice,out}(k) \leq \mathbf{P}^{\max}_{ice,out}, \tag{4.27f}$$

$$\mathbf{P}^{\min}_{em,out} \leq \mathbf{P}_{batt,out}(k) \leq \mathbf{P}^{\max}_{batt,out}, \tag{4.27g}$$

$$\mathbf{P}^{\min}_{batt,out} \leq \mathbf{P}_{batt,out}(k) \leq \mathbf{P}^{\max}_{batt,out}, \tag{4.27h}$$

$$\sum_{j=1}^{n} \left[P_{m_j,out}(k) \cdot R_{m_j,out} - P_{m_j,inp}(k) \cdot R_{m_j,inp}\right] + \sum_{l=1}^{p} P_{w_l}(k) \cdot R_{w_l} = 0, \tag{4.27i}$$

$$\mathbf{x}_{batt}(k+1) = (\Delta t \cdot A_{batt} + 1)\, \mathbf{x}_{batt}(k) + \Delta t \cdot B_{batt,inp} \mathbf{P}_{batt,inp}(k) + \Delta t \cdot B_{batt,out} \mathbf{P}_{batt,out}(k), \tag{4.27j}$$

$$\mathbf{x}^{\min}_{batt}(k) \leq \mathbf{x}_{batt}(k) \leq \mathbf{x}^{\max}_{batt}(k), \tag{4.27k}$$

$$\mathbf{x}_{batt}(1) = x^{0}_{batt}, \tag{4.27l}$$

$$\mathbf{x}_{batt}(N_f) = x^{N_f}_{batt}. \tag{4.27m}$$

for all $k \in \{1, 2, \ldots, N_f - 1\}$, $n = 4$, $j = \{1, 2, 3, 4\}$, $s \subseteq j = \{3\}$, $m_j \in \{\text{ice, em, batt, T}\}$, $m_s \in \{\text{batt}\}$, $t \in \{\text{inp, out}\}$, with $\Delta t = 1$, $A_{batt} = 0$, $B_{batt,inp} = 0$, $B_{batt,out} = -1/Q \cdot E$.

Remark 4.1. An idea of the computational complexity of (4.27) can be obtained from the number of variables and constraints in the problem formulation; it has $(2n + S) \cdot (N_f - 1)$ continuous variables; $\left(2n + \sum_{j=1}^{n} q_j + 2S\right) \cdot (N_f - 1)$ inequality constraints ($2n\,(N_f - 1)$ from the constraints on the power variables, $\sum_{j=1}^{n} q_j \cdot (N_f - 1)$ from the piecewise affine loss models, and $2S \cdot (N_f - 1)$ from the state path constraints); and $(r + S) \cdot (N_f - 1) + S$ equality constraints ($r \cdot (N_f - 1)$ from the conservation of power constraints, $S \cdot (N_f - 1)$ from the state dynamics constraints, and S from the final value constraints). With $N_f = 1023$, $n = 4$, $q_j = \{1, 2, 8, 2\}$, $S = 1$, $r = 3$, we have 9198 continuous variables, 23506 inequality constraints, and 4089 equality constraints.

4.3.2 Model validation

The topology optimization is performed using power signal whereas the component models depend on speed and torque signals. In order to assess the validity of such models, a

comparison is carried out using DP, which guarantees a globally optimal solution. This approach requires the quantization of all the variables in the problem formulation: the independent variable, all the inputs, all the state variables, and all the power demand variables.

Assumption 2. *(DP)* The EMS formulation explored here will take a step further in the modeling of the mechanical transmission elements. That is, the assumption on the ideal (mechanical and electrical) power transmission element will be strengthen for the mechanical power transmission elements. Namely, the following three elements: (i) the final drive, (ii) the gearbox, and (iii) the reduction gear. These three elements will remain lossless and will be modeled only through their gear ratios: γ_{FG}, $\gamma_{GB}(i_{GB}(k))$, and γ_{EM}, respectively.

The EMS considered for the DP approach replaces the power demand signal at the wheels by the following corresponding torque demand signal:

$$T_w(i_{GB}(k)\,|\,a_{\mathrm{v}}(k)) = (m_{\mathrm{v}}(i_{GB}(k)) \cdot a_{\mathrm{v}}(k) + F_{rr} + F_{slope} + F_{air}) \cdot r \tag{4.28}$$

$$m_{\mathrm{v}} = m + I_{\mathrm{v}}(i_{GB}(k))/r^2, \tag{4.29}$$

$$I_{\mathrm{v}}(i_{GB}(k)) = \left(I_{EM} \cdot \gamma_{EM}^2 + I_{ICE} \cdot \gamma_{GB}^2\,(i)\right) \cdot \gamma_{FG}^2.$$

The equation enforcing the conservation of mechanical power will be replaced by a conservation of torque equation applied at the main shaft:

$$\gamma_{GB}(i_{GB}(k)) \cdot T_{ice} + \gamma_{EM} \cdot T_{em} - \frac{1}{\gamma_{FG}} \cdot T_w(i_{GB}(k)\,|\,a_{\mathrm{v}}(k)) = 0 \tag{4.30}$$

The objective function will be replaced by the following speed-dependent one:

$$J_{\text{fuel}} = \Delta t \cdot \sum_k \dot{m}_f\left(T_{ice}(k), w_{ice}(u_{GB}(k))\right), \tag{4.31}$$

with $\dot{m}_f(.)$ (g/s) the fuel consumption rate, and T_{ice} (N) the engine torque. Adapting the notation of the previous subsection, the DP problem formulation is described as

follows:

$$\min_{T_{ice}(k)\,,\,u_{GB}(k)} \; J_{\text{fuel}} = \Delta t \cdot \sum_{k} \; \dot{m}_f \left(T_{ice}(k), w_{ice}(u_{GB}(k))\right), \tag{4.32a}$$

subject to:

$$P_{em,inp}(k) = T_{em}(k) \cdot \omega_{em}(k) \cdot \eta^{-sign(T_{em}(k))} \left(T_{em}(k) \mid \omega_{em}(k)\right) \tag{4.32b}$$

$$P_{batt,inp}(k) = \frac{E^2}{2\,R}\left[1 - \sqrt{1 - 4\frac{R}{E^2}P_{batt,out}}\right] \tag{4.32c}$$

$$T_{ice}^{\min}(\omega_{ice}(k)) \leq T_{ice}(k) \leq T_{ice}^{\max}(\omega_{ice}(k)), \tag{4.32d}$$

$$T_{em}^{\min}(\omega_{em}(k)) \leq T_{em}(k) \leq T_{em}^{\max}(\omega_{em}(k)), \tag{4.32e}$$

$$P_{batt,out}^{\min} \leq P_{batt,out}(k) \leq P_{batt,out}^{\max}, \tag{4.32f}$$

$$u_{GB}(k) \in \{-1, 0, 1\}, \tag{4.32g}$$

$$\omega_{ice}(k) = \frac{v(k)}{r} \cdot \gamma_{FG} \cdot \gamma_{GB}(i_{GB}(k)) \tag{4.32h}$$

$$\omega_{em}(k) = \frac{v(k)}{r} \cdot \gamma_{FG} \cdot \gamma_{EM} \tag{4.32i}$$

$$\omega_{ice}^{\min} \leq \omega_{ice}(k) \leq \omega_{ice}^{\max}, \tag{4.32j}$$

$$\omega_{em}^{\min} \leq \omega_{em}(k) \leq \omega_{em}^{\max}, \tag{4.32k}$$

$$P_{batt,out}(k) - P_{em,inp}(k) = 0, \tag{4.32l}$$

$$\gamma_{GB}(i_{GB}(k)) \cdot T_{ice}(k) + \gamma_{EM} \cdot T_{em}(k) - \frac{1}{\gamma_{FG}} \cdot T_w(i_{GB}(k) \mid a_{\text{v}}(k)) = 0, \tag{4.32m}$$

$$x_{batt}(k+1) = (\Delta t \cdot A_{batt} + 1)\, x_{batt}(k) + \Delta t \cdot B_{batt,inp} P_{batt,inp}(k), \tag{4.32n}$$

$$i_{GB}(k+1) = i_{GB}(k) + u_{GB}(k), \tag{4.32o}$$

$$i_{GB}(k) \in \{1, 2, \ldots, 5\}, \tag{4.32p}$$

$$x_{batt}^{\min} \leq x_{batt}(k) \leq x_{batt}^{\max}, \tag{4.32q}$$

$$x_{batt}(1) = x_{batt}^{0} \tag{4.32r}$$

$$x_{batt}(N_f) = x_{batt}^{N_f}, \tag{4.32s}$$

with $A_{batt} = 0$, and $B_{batt,inp} = -1/Q \cdot E$. The problem can be simplified by combining (4.32b), (4.32c), and (4.32l) as follows:

$$\min_{T_{ice}(k)\,,\,u_{GB}(k)} \; J_{\text{fuel}} = \Delta t \cdot \sum_{k} \dot{m}_f \left(T_{ice}(k), w_{ice}(u_{GB}(k))\right), \tag{4.33a}$$

subject to:

$$P_{batt,inp}(k) = \frac{E^2}{2\,R}\left[1 - \sqrt{1 - 4\frac{R}{E^2}\left(T_{em}(k)\cdot\omega_{em}(k)\cdot\eta^{-sign(T_{em}(k))}\left(T_{em}(k)\,|\,\omega_{em}(k)\right)\right)}\right] \tag{4.33b}$$

$$T_{ice}^{\min}(\omega_{ice}(k)) \le T_{ice}(k) \le T_{ice}^{\max}(\omega_{ice}(k)), \tag{4.33c}$$

$$T_{em}^{\min}(\omega_{em}(k)) \le T_{em}(k) \le T_{em}^{\max}(\omega_{em}(k)), \tag{4.33d}$$

$$P_{batt,out}^{\min} \le P_{batt,out}(k) \le P_{batt,out}^{\max}, \tag{4.33e}$$

$$u_{GB}(k) \in \{-1, 0, 1\}, \tag{4.33f}$$

$$\omega_{ice}(k) = \frac{v(k)}{r} \cdot \gamma_{FG} \cdot \gamma_{GB}(i_{GB}(k)) \tag{4.33g}$$

$$\omega_{em}(k) = \frac{v(k)}{r} \cdot \gamma_{FG} \cdot \gamma_{EM} \tag{4.33h}$$

$$\omega_{ice}^{\min} \le \omega_{ice}(k) \le \omega_{ice}^{\max}, \tag{4.33i}$$

$$\omega_{em}^{\min} \le \omega_{em}(k) \le \omega_{em}^{\max}, \tag{4.33j}$$

$$\gamma_{GB}(i_{GB}(k)) \cdot T_{ice}(k) + \gamma_{EM} \cdot T_{em}(k) - \frac{1}{\gamma_{FG}} \cdot T_w(i_{GB}(k)\,|\,a_{\text{v}}(k)) = 0, \tag{4.33k}$$

$$x_{batt}(k+1) = (\Delta t \cdot A_{batt} + 1)\, x_{batt}(k) + \Delta t \cdot B_{batt,inp} P_{batt,inp}(k), \tag{4.33l}$$

$$i_{GB}(k+1) = i_{GB}(k) + u_{GB}(k), \tag{4.33m}$$

$$i_{GB}(k) \in \{1, 2, \ldots, 5\}, \tag{4.33n}$$

$$x_{batt}^{\min} \le x_{batt}(k) \le x_{batt}^{\max}, \tag{4.33o}$$

$$x_{batt}(1) = x_{batt}^{0} \tag{4.33p}$$

$$x_{batt}(N_f) = x_{batt}^{N_f}. \tag{4.33q}$$

At last, if we solve the conservation of torque equation for T_{em},

$$T_{em}(k) = \frac{1}{\gamma_{EM}}\left(\frac{1}{\gamma_{FG}} \cdot T_w(i_{GB}(k)\,|\,a_{\text{v}}(k)) - \gamma_{GB}(i_{GB}(k)) \cdot T_{ice}(k)\right), \tag{4.34}$$

and replace this expression in the rest of the problem formulation we can simplify the problem to one having one continuous input variable $T_{ice}(k)$, one discrete input variable $u_{GB}(k)$, one continuous state $x_{batt}(k)$, and one discrete state $i_{GB}(k)$. Additionally,

quantization constraints should be added to the continuous input and state variables:

$$T_{ice}(k) \in U_{ice,\text{grid}},$$
$$x_{batt}(k) \in X_{batt,\text{grid}},$$

For the sake of completeness, the convex (solved via LP) and the non-convex (solved via DP) techniques will be compared in three different cases:

(a) **Fixed total moment of inertia**: For this first comparison, the total moment of inertia will be fixed to the following average value:

$$I_{\text{v},avg} = \frac{1}{5}\sum_{i=1}^{5}\left(I_{EM}\cdot\gamma_{EM}^2 + I_{ICE}\cdot\gamma_{GB}^2(i)\right)\cdot\gamma_{FG}^2. \tag{4.35}$$

Although a constant moment of inertia is used to compute the power demand, gear shifting is kept as a control variable for the DP formulation and thus optimized. Fixing the total moment of inertia is done with the aim of having the same power demand signal in both, the speed dependent and the speed independent formulation. The power signals computed for the speed-dependent DP problem formulation and the speed-independent LP formulation are displayed on Fig. 4.12. Their difference in relative fuel consumption is summarized on Table 4.3. As expected, the LP speed-independent approach achieves a lower fuel consumption. This was expected since that formulation is based on more idealistic assumptions: compare Assumption 1 against Assumption 2. One can even argue that the fuel consumption computed with the LP speed-independent approach is not as small as expected. A possible explanation could be the fact that the speed-independent model of the EM has significant losses (around 800 W) even when it is not being used ($P_{em,out}(k) = 0$).

(b) **Varying total moment of inertia**: This time I_{v} will depend on gearshifting, i_{GB} (4.30). In other words, the equivalent mass can be optimized in the DP formulation through u_{GB}, which could lead to a better fuel consumption. Once the DP formulation has been computed, the total moment of inertia signal is used to compute the power demand signal for the LP formulation. The relevant signals computed from both approaches are displayed on Fig. 4.13. As can be seen in the first subplot, the power demand is higher than for a fixed total moment of inertia when $P_w(k) > 0$, reducing the effort required by the engine, and a higher absolute value for $P_w < 0$, increasing the amount of regenerative braking power.

(c) **Varying total moment of inertia as function of a rule-based gearshifting strategy**: Consider the gearshifting strategy shown in Fig. 4.14. It is a ruled-based

strategy that solely depends on the speed. This gearshifting strategy will be used to compute the total moment of inertia for both the LP speed-independent approach and the DP-speed dependent approach. The power signal results are displayed on Fig. 4.15. The fuel consumption is presented on Table 4.3: there is an important increase in fuel consumption for the DP speed-dependent approach and a very small increase for the LP speed-independent approach despite both approaches having the same power demand signal. This highlights the importance of the gearshifting strategy and shows that the proposed one, based only on the longitudinal speed, may lead to poor fuel consumption results. Previous works have found that optimizing over a set of architectures with different sub-optimal EMS might lead to different optimal architectures. Moreover, as it is illustrated in Appendix B, using a poor sub-optimal EMS may lead a designer to underestimate the potential of the optimal solution with respect to other candidate architectures.

Case	Approach	Fuel consumption	Units	Computation time (s)
(a)	LP speed-independent	4.181	l/100km	2.295
	DP speed-dependent	4.423	l/100km	$4.680 \cdot 10^3$
(b)	LP speed-independent	3.121	l/100km	1.866
	DP speed-dependent	3.294	l/100km	$4.817 \cdot 10^3$
(c)	LP speed-independent	3.472	l/100km	1.659
	DP speed-dependent	6.356	l/100km	$2.410 \cdot 10^3$

TABLE 4.3: Fuel consumption comparison for the convex modeling validation.

Based on the results obtained in the comparisons above, it can be concluded that the LP convex formulation of the EMS does not imply a considerable loss of accuracy: for cases (a) and (b), it provides a tight lower bound for the optimal fuel consumption. When the optimality is not guaranteed, significant differences may arise, see case (c). Nonetheless, when optimality is indeed guaranteed, the main limitation seems to be given by the total moment of inertia: since the LP convex approach is based on a power network modeling, the moment of inertia is neglected. The assumption of a negligible moment of inertia has been taken in several previous convex modeling works [41, 113]. Moreover, as it will be shown later, in this work, under these assumptions we will be able to perform a simultaneous computation of the optimal architecture and EMS.

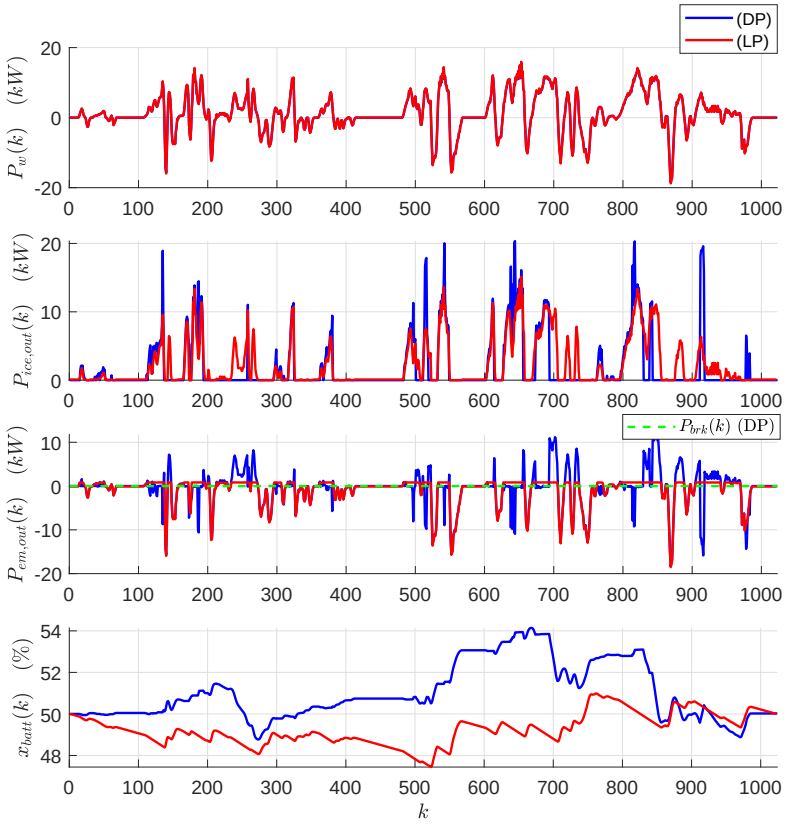

FIGURE 4.12: Comparison between the DP speed-dependent approach and the LP speed-independent approach. $I_v(k)$ has been fixed as (4.35). The final state-of-energy is identical for both methods.

4.3.3 Simultaneous architecture design

Before presenting the MILP formulation of the architecture design, let us recall that the topological structure of the power network is defined by the following equation:

$$\sum_{j=1}^{n} \left[P_{m_j,out}(k) \cdot R_{m_j,out} - P_{m_j,inp}(k) \cdot R_{m_j,inp} \right] + \sum_{l=1}^{p} P_{w_l}(k) \cdot R_{w_l} = 0. \tag{4.36}$$

with r the total number of nodes, $R_{m_j,t}, R_{w_1} \in \mathbb{R}^{r \times 1}$, p the total number of power demand signals in the network, and where the $i-th$ entry of $R_{m_j,t}$ (respectively R_{w_1}) is equal to 1 if and only if $P_{m_j,t}$ (respectively P_{w_l}) is present at the $i-th$ node and zero otherwise; the rest of its entries are equal to zero. For the parallel HEV studied in Subsection Model Validation 4.3.2, the network only has 3 nodes, $r = 3$, and one power

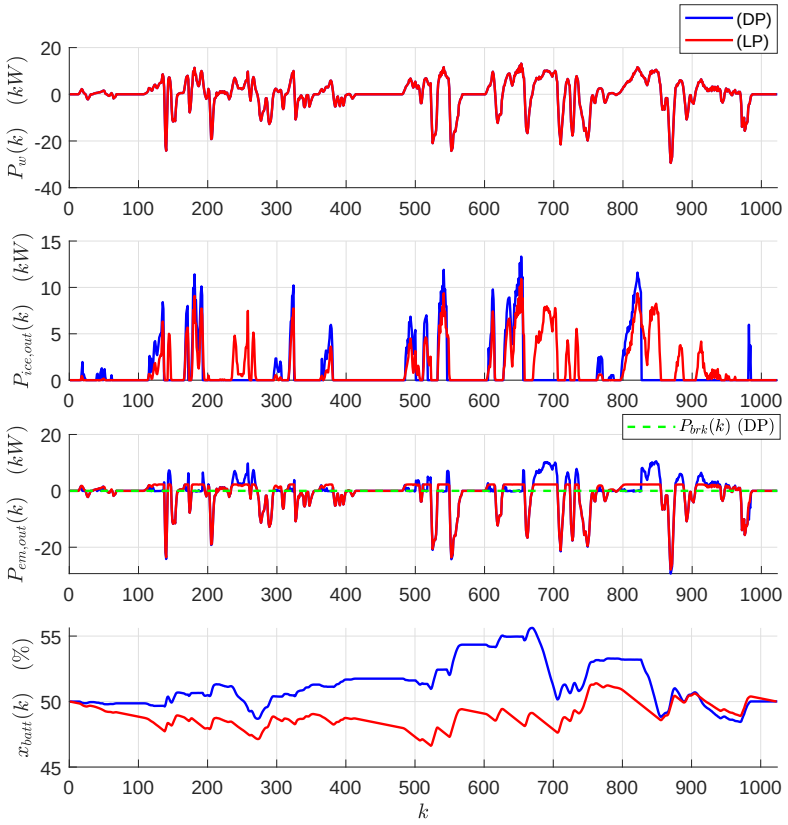

FIGURE 4.13: Comparison between the DP speed-dependent approach and the LP speed-independent approach. A varying total moment of inertia, $I_v(k)$, is considered and computed by optimizing gearshifting. The final state-of-energy is identical for both methods.

demand signal, $p = 1$, thus, $R_{m_j,t}$ and R_{w_l} are given as follows:

$$R_{ice,inp} = \begin{bmatrix} 0 \\ 0 \\ 0 \end{bmatrix}, R_{em,inp} = \begin{bmatrix} 0 \\ 0 \\ 1 \end{bmatrix}, R_{batt,inp} = \begin{bmatrix} 0 \\ 0 \\ 0 \end{bmatrix}, R_{w_1} = \begin{bmatrix} 0 \\ 1 \\ 0 \end{bmatrix},$$

$$R_{ice,out} = \begin{bmatrix} 1 \\ 0 \\ 0 \end{bmatrix}, R_{em,out} = \begin{bmatrix} 0 \\ 1 \\ 0 \end{bmatrix}, R_{batt,out} = \begin{bmatrix} 0 \\ 0 \\ 1 \end{bmatrix},$$

Therefore, if we would like to include the architecture design as a part of the optimization problem, it should suffice to replace the parameter vectors $R_{m_j,t}$ by vectors of binary variables $\mathbf{R}_{m_j,t} \in \mathbb{B}^r$. Additionally, we would like to let the program optimizing the element connections also decide which elements should be part of the topology and which ones should be discarded. To this end, let us define $z_{m_j} \in \mathbb{B}$ as the binary variable that is equal to one only if the m_j has been chosen to be connected to the

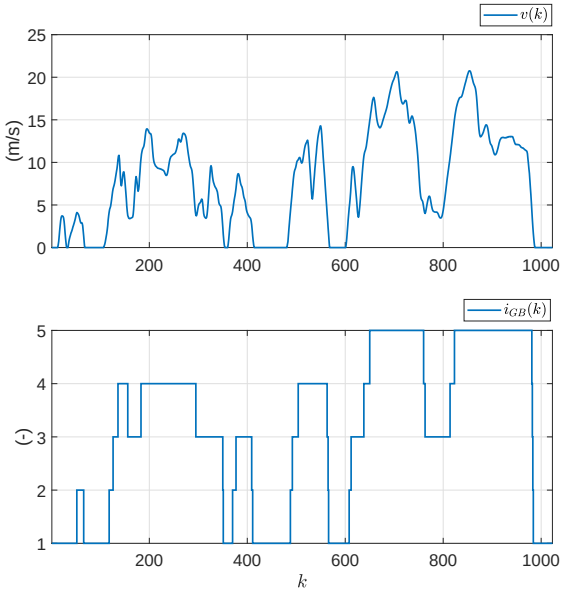

FIGURE 4.14: Top: velocity profile; bottom: rule-based gearshifting strategy.

network. If $z_{m_j} = 1$, then the input and the output (respectively, only the input if the element is a sink/source, e.g., an ICE or a battery pack) should be connected to the network, i.e., $R_{m_j,inp}$ and $R_{m_j,out}$ (respectively, only $R_{m_j,out}$) must have one entry equal to 1. If $z_{m_j} = 0$, all the entries of $R_{m_j,out}$ and $R_{m_j,out}$ must be equal to zero. The latter can be imposed through the following equality constraints:

$$\begin{bmatrix} R^T_{m_j,inp} \\ R^T_{m_j,out} \end{bmatrix} \mathbf{I}_r = \mathbf{I}_{m_j} z_{m_j}, \tag{4.37}$$

with $\mathbf{I}_r = [1] \in \mathbb{R}^r$ an $\mathbf{I}_{m_j} = [1] \in \mathbb{R}^2$ if m_j is a transmission element, and through

$$\left[R^T_{m_j,inp}\right] \mathbf{I}_r = \mathbf{I_{m_j}}, z_{m_j} \text{ or } \left[R^T_{m_j,out}\right] \mathbf{I}_{m_j} = \mathbf{I_1}, z_{m_j} \tag{4.38}$$

with $\mathbf{I}_{m_j} = [1] \in \mathbb{R}^1$ if m_j is a source/sink element. Note that an additional constraint has to be imposed on $R_{m_j,t}$ to avoid having power variables of different nature (electrical and mechanical) interacting at the same node. The convention that will be followed in this work is that the mechanical nodes of the network will be represented by the first r_{mech} entries of $R_{m_j,t}$ and the electrical nodes will correspond to the last r_{elect} entries of $R_{m_j,t}$. If $R_{m_j,out}$ ($R_{m_j,inp}$) corresponds to a mechanical power variable, then the last r_{elect} elements of $R_{m_j,out}$ ($R_{m_j,inp}$) will be forced to zero. Conversely, If $R_{m_j,out}$ ($R_{m_j,inp}$) corresponds to an electrical power variable, then the first r_{mech} elements of $R_{m_j,out}$ ($R_{m_j,inp}$) will be forced to zero. For instance, let us consider a network with $r = 3$ nodes, where r_{mech}, the number of mechanical nodes, is equal to 2, and r_{elect} the number of electric nodes, is equal to 1. (4.37) for a mechanical transmission element

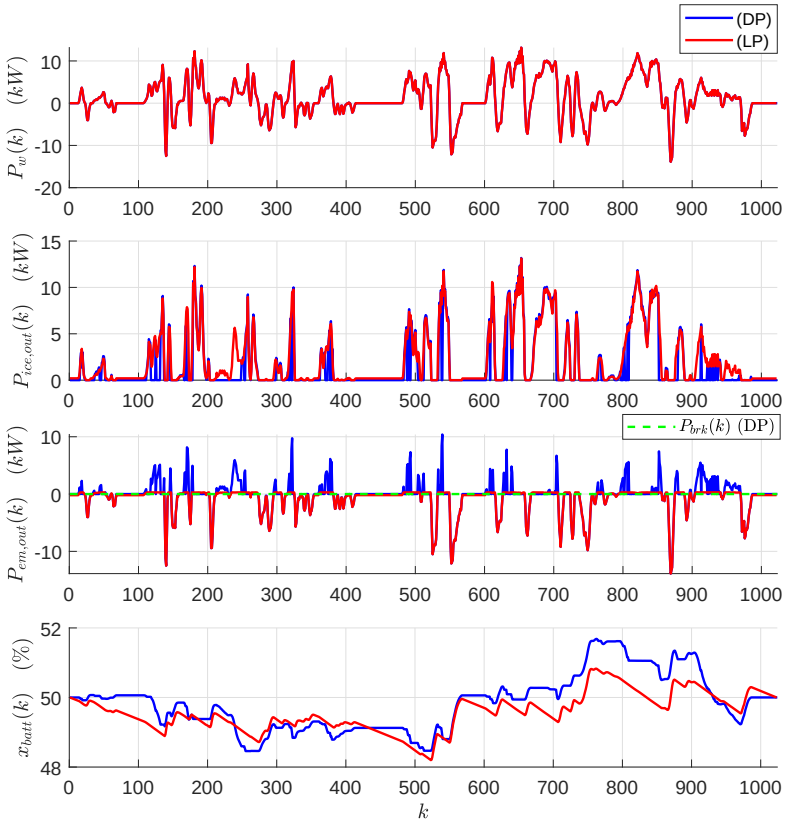

FIGURE 4.15: Comparison between the DP speed-dependent approach and the LP speed-independent approach subject to the gearshifting strategy shown in Fig. 4.14. The final state-of-energy is identical for both methods

will be equal to:

$$\begin{bmatrix} r_{T,inp}^{(1)} & r_{T,inp}^{(2)} & r_{T,inp}^{(3)} \\ r_{T,out}^{(1)} & r_{T,out}^{(2)} & r_{T,out}^{(3)} \end{bmatrix} \begin{bmatrix} 1 \\ 1 \\ 1 \end{bmatrix} = \begin{bmatrix} 1 \\ 1 \end{bmatrix} z_T,$$

but since the third node is an electrical node $r_{T,inp}^{(3)}$ and $r_{T,out}^{(3)}$ are equal to zero, thus:

$$\begin{aligned} r_{T,inp}^{(1)} + r_{T,inp}^{(2)} &= z_T, \\ r_{T,out}^{(1)} + r_{T,out}^{(2)} &= z_T. \end{aligned}$$

Defining $R_{m_j} = \begin{bmatrix} R^T_{m_j,inp} \\ R^T_{m_j,out} \end{bmatrix}$, $R_{m_j} = \begin{bmatrix} R^T_{m_j,inp} \end{bmatrix}$ or $R_{m_j} = \begin{bmatrix} R^T_{m_j,out} \end{bmatrix}$, if m_j is a transmission element, if m_j is sink/source element, and $R = \begin{bmatrix} R_{m_1} \\ R_{m_2} \\ \vdots \\ R_{m_n} \end{bmatrix}$, (4.37) and (4.38) can be expressed in the following more compact form:

$$R\, I_r = \mathbf{I}_m\, z \tag{4.39}$$

with

$$\mathbf{I}_m = \mathrm{diag}[I_{m_j}] = \begin{bmatrix} I_{m_1} & & & 0 \\ & I_{m_2} & & \\ 0 & & \ddots & \\ & & & I_{m_n} \end{bmatrix}, \text{ and } z = \begin{bmatrix} z_{m_1} \\ z_{m_2} \\ \vdots \\ z_{m_n} \end{bmatrix}.$$

By adding (4.39) to the previous problem formulation, (4.27), we can finally obtain a simultaneous architecture design and EMS mixed-integer programming formulation. However, note the conservation of power constraint, includes the nonlinear term $P_{m_j,t} \cdot R_{m_j,t}$, which corresponds to the product of a continuous variable and a binary variable. Fortunately, this product can be linearized by replacing it by an additional continuous variable, thus, obtaining the sought MILP formulation. The variable replacing the product $P_{m_j,t} \cdot R_{m_j,t}$ will be denoted as $Y_{m_j,t} \in \mathbb{R}^r$. To ensure that $Y_{m_j,t}$ is equal to the product $P_{m_j,t} \cdot R_{m_j,t}$, the following four inequality constraints are imposed for each triple $\{Y_{m_j,t}, R_{m_j,t}, P_{m_j,t}\}$ [58]:

$$Y_{m_j,t} - P_{m_j,t} - P^{\min}_{m_j,t} \cdot R_{m_j,t} \preceq -I_r \cdot P^{\min}_{m_j,t}, \tag{4.40a}$$

$$-Y_{m_j,t} + P_{m_j,t} + P^{\max}_{m_j,t} \cdot R_{m_j,t} \preceq I_r \cdot P^{\max}_{m_j,t}, \tag{4.40b}$$

$$Y_{m_j,t} - P^{\max}_{m_j,t} \cdot R_{m_j,t} \preceq 0, \tag{4.40c}$$

$$-Y_{m_j,t} + P^{\min}_{m_j,t} \cdot R_{m_j,t} \preceq 0, \tag{4.40d}$$

with $\preceq$ denoting an element-wise inequality. In order to show that the four constraints above actually impose $Y_{m_j,t} = P_{m_j,t} \cdot R_{m_j,t}$, we will use an scalar version of them. Namely, we will analyze the product $P_{m_j,t} \cdot r^{(1)}_{m_j,t}$ and its equivalence to $y^{(1)}_{m_j,t}$:

- Case 1: $r^{(1)}_{m_j,t} = 0$: regardless of the value taken by $P_{m_j,t}$, the last two constraints imposed the following

$$y^{(1)}_{m_j,t} \leq 0,$$
$$y^{(1)}_{m_j,t} \geq 0,$$

  which can only be simultaneously satisfied if $y^{(1)}_{m_j,t} = 0$, validating that $y^{(1)}_{m_j,t} = P_{m_j,t} \cdot r^{(1)}_{m_j,t} = 0$ when $r^{(1)}_{m_j,t} = 0$.

- Case 2: $r^{(1)}_{m_j,t} = 1$ and $P_{m_j,t} = 0$: the first two constrains imposed the following

$$y^{1}_{m_j,t} \leq 0,$$
$$y^{1}_{m_j,t} \geq 0,$$

  which can only be simultaneously satisfied if $y^{(1)}_{m_j,t} = 0$, validating that $y^{(1)}_{m_j,t} = P_{m_j,t} \cdot r^{(1)}_{m_j,t} = 0$ when $P_{m_j,t} = 0$.

- Case 3: $r^{(1)}_{m_j,t} = 1$ and $P_{m_j,t} \neq 0$: the first two constraints take the following form

$$y^{1}_{m_j,t} \leq P_{m_j,t},$$
$$y^{1}_{m_j,t} \geq P_{m_j,t},$$

  which can only be simultaneously satisfied if $y^{(1)}_{m_j,t} = P_{m_j,t}$, proving that $y^{(1)}_{m_j,t} = P_{m_j,t} \cdot r^{(1)}_{m_j,t} = P_{m_j,t}$ when $r^{(1)}_{m_j,t} = 1$.

Remark 4.2. For an EMS with N_s source/sink elements, N_T transmission elements and r nodes, linearization constraints (4.40) add $(N_s + 2 \cdot N_T) \cdot r \cdot N_f$ continuous variables to the convex problem formulation. For instance, for the simple parallel topology studied in Subsection Model validation, $N_s = 2$, $N_T = 2$, $r = 2$ and $N_f = 1100$. Therefore, $(N_s + 2 \cdot N_T) \cdot r \cdot N_f = (2 + 2 \cdot 2) \cdot 3 \cdot 1100 = 19800$ extra variables would be required. As for the discrete variables, connectivity constraints (4.39) require $(N_s + 2 \cdot N_s) \cdot r + (N_s + 2 \cdot N_s) = (2 + 2 \cdot 2) \cdot 3 + (2 + 2) = 20$ binary variables.

Once the linearization constraints have been imposed, the nonlinear terms have replaced by $Y_{m_j,t}(k)$ in the conservation of power equation:

$$\sum_{j=1}^{n} \left[\mathbf{Y}_{m_j,out}(k) - \mathbf{Y}_{m_j,inp}(k) \right] + \sum_{l=1}^{p} P_{w_l}(k) \cdot R_{w_l} = 0, \tag{4.41}$$

Finally, the simultaneous architecture optimization and EMS is formulated as the following MILP:

$$\min_{\mathbf{P}_{m_j,t}} \quad J = \Delta t \cdot \sum_j \sum_k \mathbf{P}_{m_j,inp}(k) - \mathbf{P}_{m_j,out}(k), \tag{4.42a}$$

subject to:

$$\mathbf{P}_{m_j,out}(k) \leq a_{m_j,i} \cdot \mathbf{P}_{m_j,inp}(k) + b_{m_j,i}, \qquad i \in \{1, 2, \ldots, q_j\} \tag{4.42b}$$

$$\mathbf{P}^{\min}_{m_j,out} \leq \mathbf{P}_{m_j,out}(k) \leq \mathbf{P}^{\max}_{m_j,out}, \tag{4.42c}$$

$$\sum_{j=1}^{n} \left[\mathbf{Y}_{m_j,out}(k) - \mathbf{Y}_{m_j,inp}(k)\right] + \sum_{l=1}^{p} P_{w_l}(k) \cdot R_{w_l} = 0, \tag{4.42d}$$

$$\mathbf{x}_{m_s}(k+1) = (\Delta t \cdot A_{m_s} + 1)\, \mathbf{x}_{m_s}(k) + \Delta t \cdot B_{m_s,inp} \mathbf{P}_{m_s,inp}(k) + \Delta t \cdot B_{m_s,out} \mathbf{P}_{m_s,out}(k), \tag{4.42e}$$

$$x^{\min}_{m_s}(k) \leq \mathbf{x}_{m_s}(k) \leq x^{\max}_{m_s}(k), \tag{4.42f}$$

$$\mathbf{x}_{m_s}(1) = x^{0}_{m_s} \tag{4.42g}$$

$$\mathbf{x}_{m_s}(N_f) = x^{N_f}_{m_s}, \tag{4.42h}$$

$$\mathbf{R}(\mathbf{R}_{m_j,t})\, I_r = I_m\, \mathbf{z}, \tag{4.42i}$$

$$\mathbf{Y}_{m_j,t}(k) - \mathbf{P}_{m_j,t}(k) - P^{\min}_{m_j,t} \cdot \mathbf{R}_{m_j,t} \preceq -I_r \cdot P^{\min}_{m_j,t}, \tag{4.42j}$$

$$-\mathbf{Y}_{m_j,t}(k) + \mathbf{P}_{m_j,t}(k) + P^{\max}_{m_j,t} \cdot \mathbf{R}_{m_j,t} \preceq I_r \cdot P^{\max}_{m_j,t}, \tag{4.42k}$$

$$\mathbf{Y}_{m_j,t}(k) - P^{\max}_{m_j,t} \cdot \mathbf{R}_{m_j,t} \preceq 0, \tag{4.42l}$$

$$-\mathbf{Y}_{m_j,t}(k) + P^{\min}_{m_j,t} \cdot \mathbf{R}_{m_j,t} \preceq 0, \tag{4.42m}$$

for all $k \in \{1, 2, \ldots, N_f - 1\}$, $j = \{1, 2, \ldots, n\}$, $s \subseteq j$, m_j, $m_s \in \{\text{batt}\}$, $t \in \{\text{inp, out}\}$, with $\Delta t = 1$.

Remark 4.3. Note that for the definition of J given above, if there is an element that has non-zero losses at the minimum value of its loss model, even if the element is not in the topology, it will affect the value of J. To correct this modeling error, we will modify the objective functional as follows:

$$J' = J - (N_f - 1) \cdot c_{m_f} \cdot \left(1 - z_{m_j}\right), \tag{4.43}$$

with $c_{m_j} > 0$ the minimum loss value for the loss model of the m_j component.

4.3.4 Architectures as graphs

As done in several other works [4, 5], the representation of the architectures as power networks used here can be seen from a graph theory perspective. More concretely, the network representation is equivalent to a bipartite graph (see Fig. 4.16), since all the

connections between the components are done through the nodes of the network. In this bipartite graph, the transmission elements are represented by two vertexes (input and output power connection) and the sinks/sources are represented by only one vertex (input or output power connection). Representing the topology as a directed graph, we get the following adjacency matrix:

$$\begin{bmatrix} ICE \\ EM \\ T \\ Batt \\ n_1 \\ n_2 \\ n_3 \end{bmatrix} \overbrace{\left\{ \begin{bmatrix} 0 & 0 & 0 & 0 & r^{(1)}_{ice,out} & r^{(2)}_{ice,out} & r^{(3)}_{ice,out} \\ 0 & 0 & 0 & 0 & r^{(1)}_{em,out} & r^{(2)}_{em,out} & r^{(3)}_{em,out} \\ 0 & 0 & 0 & 0 & r^{(1)}_{T,out} & r^{(2)}_{T,out} & r^{(3)}_{T,out} \\ 0 & 0 & 0 & 0 & r^{(1)}_{batt,out} & r^{(2)}_{batt,out} & r^{(3)}_{batt,out} \\ r^{(1)}_{ice,inp} & r^{(1)}_{em,inp} & r^{(1)}_{T,inp} & r^{(1)}_{batt,inp} & 0 & 0 & 0 \\ r^{(2)}_{ice,inp} & r^{(2)}_{em,inp} & r^{(2)}_{T,inp} & r^{(2)}_{batt,inp} & 0 & 0 & 0 \\ r^{(3)}_{ice,inp} & r^{(3)}_{em,inp} & r^{(3)}_{T,inp} & r^{(3)}_{batt,inp} & 0 & 0 & 0 \end{bmatrix} \right\}}^{\begin{bmatrix} ICE & EM & T & Batt & n_1 & n_2 & n_3 \end{bmatrix}\cdot} \tag{4.44}$$

For the particular case of Fig. 4.16 we have:

$$\begin{bmatrix} ICE \\ EM \\ T \\ Batt \\ n_1 \\ n_2 \\ n_3 \end{bmatrix} \overbrace{\left\{ \begin{bmatrix} 0 & 0 & 0 & 0 & 1 & 0 & 0 \\ 0 & 0 & 0 & 0 & 1 & 0 & 0 \\ 0 & 0 & 0 & 0 & 0 & 0 & 1 \\ 0 & 0 & 0 & 0 & 0 & 1 & 0 \\ 0 & 0 & 1 & 0 & 0 & 0 & 0 \\ 0 & 1 & 0 & 0 & 0 & 0 & 0 \\ 0 & 0 & 0 & 0 & 0 & 0 & 0 \end{bmatrix} \right\}}^{\begin{bmatrix} ICE & EM & T & Batt & n_1 & n_2 & n_3 \end{bmatrix}} . \tag{4.45}$$

4.4 Case Study: topology and control optimization

In order to illustrate the the approach, let us consider a network with 2 mechanical nodes, 1 electric node, 1 ICE, 2 identical EMs, a battery pack and 1 mechanical transmission. The ICE will be fixed at node 1 and the power demand will be placed at node 2. The rest of the components are free, see Fig. 4.17. (4.42) takes the following form:

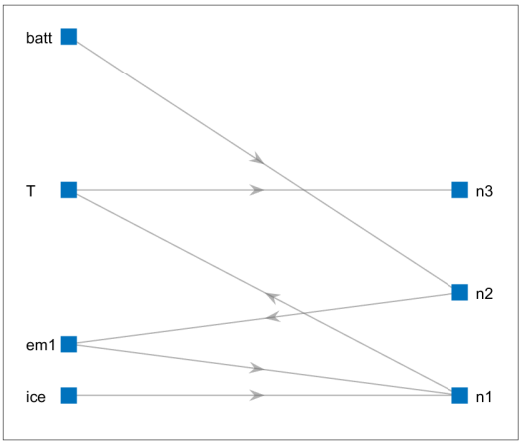

FIGURE 4.16: Bipartite arrangement of a pre-transmission parallel HEV represented as a power network.

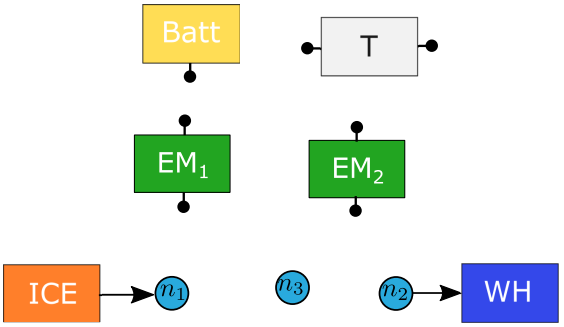

FIGURE 4.17: Topology design corresponding to simultaneous MILP (4.46).

$$\min_{\mathbf{P}_{m_j,t}} \quad J = \Delta t \cdot \sum_j \sum_k \mathbf{P}_{m_j,inp}(k) - \mathbf{P}_{m_j,out}(k), \tag{4.46a}$$

subject to:

$$\mathbf{P}_{ice,out}(k) = a_{ice,1} \cdot \mathbf{P}_{ice,inp}(k) + b_{ice,1}, \tag{4.46b}$$

$$\mathbf{P}_{em_1,out}(k) \leq a_{em_1,i} \cdot \mathbf{P}_{em_1,inp}(k) + b_{em_1,i}, \qquad i \in \{1, 2, \ldots, 16\} \tag{4.46c}$$

$$\mathbf{P}_{em_2,out}(k) \leq a_{em_2,i} \cdot \mathbf{P}_{em_2,inp}(k) + b_{em_2,i}, \qquad i \in \{1, 2, \ldots, 16\} \tag{4.46d}$$

$$\mathbf{P}_{batt,out}(k) \leq a_{batt,i} \cdot \mathbf{P}_{batt,inp}(k) + b_{batt,i}, \qquad i \in \{1, 2, \ldots, 16\} \tag{4.46e}$$

$$\mathbf{P}_{T,out}(k) \leq a_{T,i} \cdot \mathbf{P}_{T,inp}(k) + b_{T,i}, \qquad i \in \{1, 2\} \tag{4.46f}$$

$$\mathbf{P}^{\min}_{ice,out} \leq \mathbf{P}_{ice,out}(k) \leq \mathbf{P}^{\max}_{ice,out}, \tag{4.46g}$$

$$\mathbf{P}^{\min}_{em_1,out} \leq \mathbf{P}_{em_1,out}(k) \leq \mathbf{P}^{\max}_{em_1,out}, \tag{4.46h}$$

$$\mathbf{P}^{\min}_{em_2,out} \leq \mathbf{P}_{em_2,out}(k) \leq \mathbf{P}^{\max}_{em_2,out}, \tag{4.46i}$$

$$\mathbf{P}^{\min}_{batt,out} \leq \mathbf{P}_{batt,out}(k) \leq \mathbf{P}^{\max}_{batt,out}, \tag{4.46j}$$

$$\sum_{j=1}^{n} \left[\mathbf{Y}_{m_j,out}(k) - \mathbf{Y}_{m_j,inp}(k)\right] + \sum_{l=1}^{p} P_{w_l}(k) \cdot R_{w_l} = 0, \tag{4.46k}$$

$$\mathbf{x}_{batt}(k+1) = \mathbf{x}_{batt}(k) + \Delta t \cdot B_{batt,inp} \mathbf{P}_{batt,inp}(k), \tag{4.46l}$$

$$x^{\min}_{batt}(k) \leq \mathbf{x}_{batt}(k) \leq x^{\max}_{batt}(k), \tag{4.46m}$$

$$\mathbf{x}_{batt}(1) = 0 \tag{4.46n}$$

$$\mathbf{R}(\mathbf{R}_{m_j,t})\, I_r = I_m\, \mathbf{z}, \tag{4.46o}$$

$$\mathbf{Y}_{m_j,t}(k) - \mathbf{P}_{m_j,t}(k) - P^{\min}_{m_j,t} \cdot \mathbf{R}_{m_j,t} \preceq -I_r \cdot P^{\min}_{m_j,t}, \tag{4.46p}$$

$$-\mathbf{Y}_{m_j,t}(k) + \mathbf{P}_{m_j,t}(k) + P^{\max}_{m_j,t} \cdot \mathbf{R}_{m_j,t} \preceq I_r \cdot P^{\max}_{m_j,t}, \tag{4.46q}$$

$$\mathbf{Y}_{m_j,t}(k) - P^{\max}_{m_j,t} \cdot \mathbf{R}_{m_j,t} \preceq 0, \tag{4.46r}$$

$$-\mathbf{Y}_{m_j,t}(k) + P^{\min}_{m_j,t} \cdot \mathbf{R}_{m_j,t} \preceq 0, \tag{4.46s}$$

for all $k \in \{1, 2, \ldots, N_f - 1\}$, $j = \{1, 2, \ldots, n\}$, $s \subseteq j$, m_j, $m_s \in \{\text{batt}\}$, $t \in \{\text{inp}, \text{out}\}$, with $\Delta t = 1$, and $B_{batt,inp} = -1/Q \cdot E$. The battery pack and the EMs use 16 affine models, the ICE uses one, and the transmission uses 2 (it is based on a constant efficiency of 95%). The battery is empty at the beginning of the driving cycle. Given the parameters of Table C.1, using the WLTC-C1 as driving mission, and assuming that the moment of the inertia of the rotating parts can be neglected, the optimal topology found by the approach is given in Fig. 4.18, the EMS in Fig. 4.19, and the fuel consumption and computation time in Table 4.4. The optimal topology is a parallel post-transmission topology. As expected, the program was able to figure out that connecting a buffer would be advantageous, even if the buffer is initially empty.

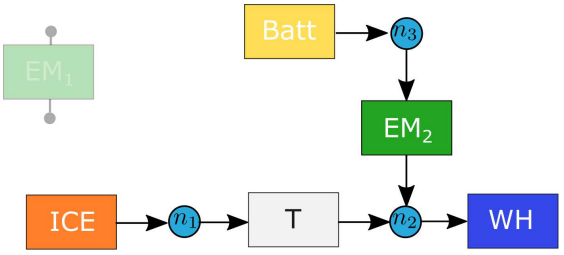

FIGURE 4.18: Topology design computed as solution to simultaneous MILP (4.46).

Case	Approach	Fuel consumption	Units	Computation time (s)
-	MILP	4.515	l/100km	279.031

TABLE 4.4: Fuel consumption and computation time for simultaneous MILP approach (4.46).

4.5 Limitations and possible extensions

The assumptions considered in the presented MILP simultaneous approach have important limitations when studying the design of HEV powertrains. Being an approach based on a power network modeling, the importance of the transmission components is underestimated. Moreover, since most HEV powertrains have only one ICE, at most two electric machines and at most 2 storage systems, the design space of this methodology

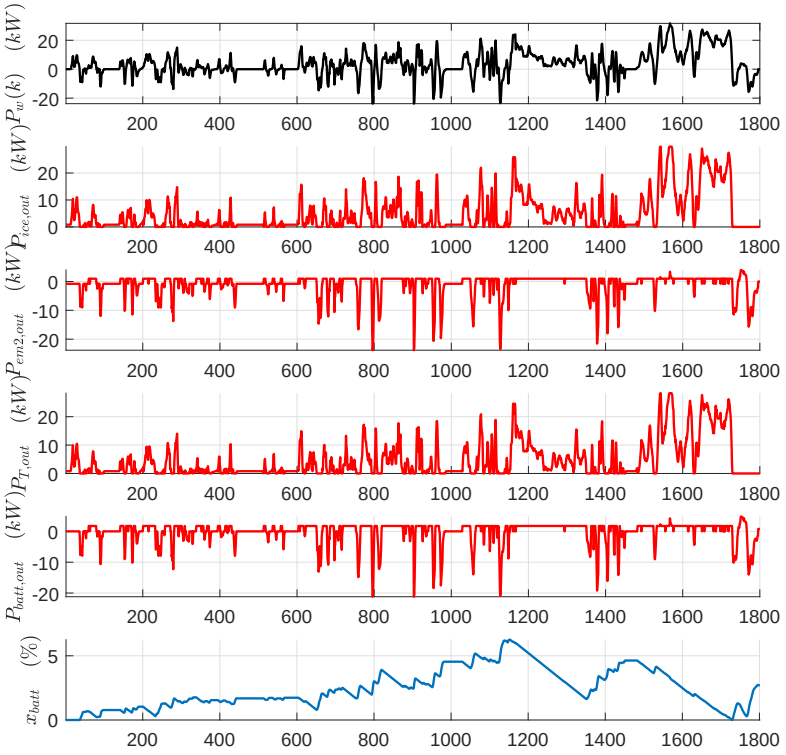

FIGURE 4.19: EMS computed solution to (4.46).

is limited. In fact, the richness of the topology design problems studied in the literature comes from the presence of mechanical transmission elements, such as PGS [5, 57] or sycrhonizer units [4, 107].

Nevertheless, beyond the systems usually encountered in the automotive sector, in the maritime industry hybrid powertrains may possess several ICEs, EMs, and storage systems. For instance, let us consider the hybrid maritime power system shown in Fig. 4.20: it includes 3 generator sets (thus, 3 ICEs and 3 EM used as generators), 3 EMs used as traction motors/generators, 1 storage system, and 2 power demand signals, resulting in a more complex power network than what can be found in typical HEVs.

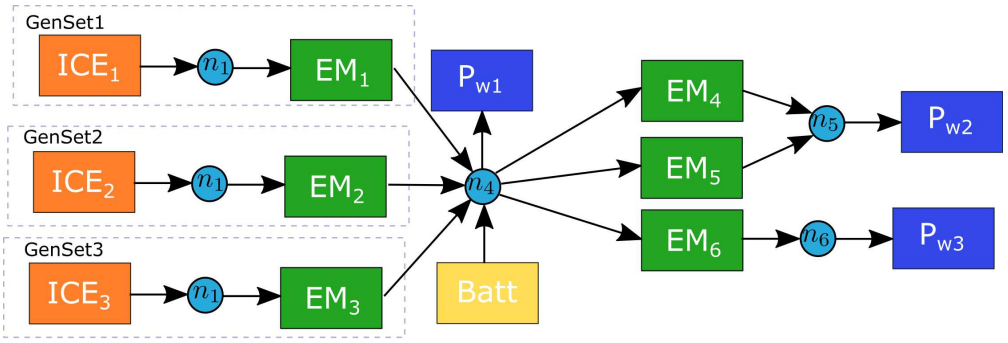

FIGURE 4.20: Example of a maritime hybrid powertrain [3].

4.5.1 Possible extension 1: optimal convex models

Using affine piecewise functions one can go beyond approximating a quadratic loss model with arbitrary accuracy. Given a set of d data points $\left(P_{inp}^{(i)}, L^{(i)}\right)$ representing the original nonlinear and nonconvex loss model, we can compute the *optimal* affine piecewise approximation as a quadratic programming problem [120]:

$$\min \quad \left\| L - \hat{\mathbf{L}} \right\|^2, \tag{4.47a}$$

$$\hat{\mathbf{L}}^{(j)} \geq \hat{\mathbf{L}}^{(i)} + \mathbf{g_i} \cdot \left(P_{inp}^{(j)} - P_{inp}^{(i)} \right), \qquad i, j \in \{1, 2, \ldots, d\}, \tag{4.47b}$$

where the affine models are recovered as $a_i = \mathbf{g_i}$ and $b_i = \hat{\mathbf{L}} - \mathbf{g_i} \cdot P_{inp}^{(i)}$, $i \in \{1, 2, \ldots, d-1\}$. Considering the EM minimal loss data from Fig. 4.14, the piecewise convex model computed via (4.47a) is shown in Fig. 4.21. The model shown there is a more accurate representation of the original data points than the quadratic model. In this approach the number of piecewise affine functions of the convex model cannot be chosen beforehand and it could go up to $d - 1$. Alternatively, we can fix the number of piecewise models

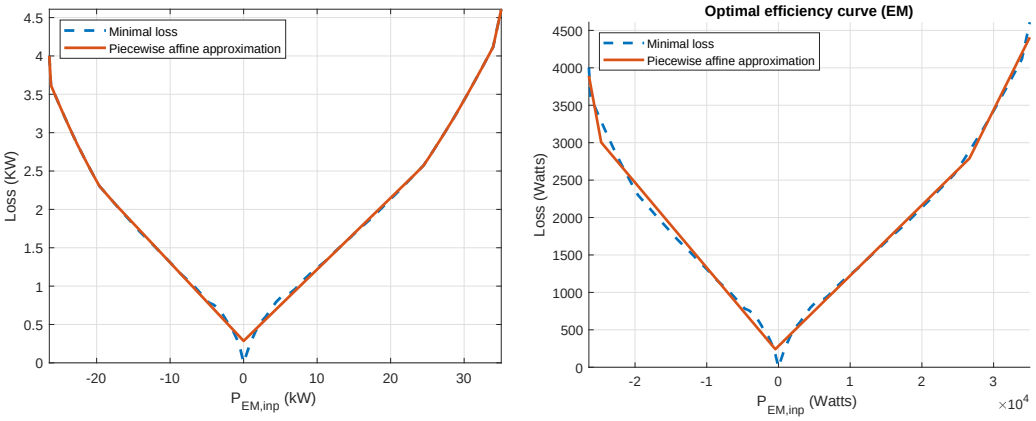

FIGURE 4.21: Optimal affine piecewise convex model computed from d data points $\left(P_{inp}^{(i)}, L^{(i)}\right)$ with $d-1$ linear functions (left) and with $q = 4$ models (right), computed via (4.47a) and (4.48), respectively.

equatl to q and find the optimal fitting by solving the following MILP problem [121]:

$$\min \quad \left\| L - \hat{\mathbf{L}} \right\|^2, \tag{4.48a}$$

$$\hat{\mathbf{L}}^{(i)} \geq a_j \cdot P_{inp}^{i} + b_j, i \in \{1, 2, \ldots, d\}, j \in \{1, 2, \ldots, q\} \tag{4.48b}$$

$$\hat{\mathbf{L}}^{(i)} \leq a_j \cdot P_{inp}^{i} + b_j + M \cdot (1 - z_{ij}), i \in \{1, 2, \ldots, d\}, j \in \{1, 2, \ldots, q\} \tag{4.48c}$$

$$\sum_j z_{ij} = 1, i \in \{1, 2, \ldots, d\}, \tag{4.48d}$$

$$z_{ij} \in \{0, 1\}, i \in \{1, 2, \ldots, d\}, j \in \{1, 2, \ldots, q\}, \tag{4.48e}$$

with M a constant large enough to make constraint (4.48c) innocuous. Considering $q = 4$, $M = 3 \cdot 10^6$, and the EM minimal loss data from Fig. 4.14, the piecewise convex model computed via (4.48) is shown in Fig. 4.21 (right).

4.5.2 Possible extension 2: main components parametrization

Convex optimization has been used to compute the optimal sizing or parametrization of the main powertrain components and the EMS simultaneously [41, 113]. The parametrization is based on the assumption that the main characteristics of the power losses models can be linearly scaled by a continuous scalar s. For instance, for EMs and ICEs, s scales the torque. For battery packs, s scales the number of cells connected in series or parallel. This sizing methodology can be adapted to our affine piecewise models as follows. Given a base loss model $P_{out} = f(P_{inp})$ with $P_{out} \in \left[P_{out}^{min}, P_{out}^{max}\right]$, the model can be linearly scaled by a factor s as follows:

$$\check{P}_{out} = s \cdot f\left(P_{inp}\right), \tag{4.49}$$

$$\check{P}_{out} \in s \cdot \left[P_{out}^{min}, P_{out}^{max}\right], \tag{4.50}$$

with $\check{P}_{inp} = s \cdot P_{inp}$, which yields:

$$\check{P}_{out} = s \cdot f\left(\frac{\check{P}_{inp}}{s}\right), \tag{4.51}$$

$$\check{P}_{out} \in s \cdot \left[P_{out}^{min}, P_{out}^{max}\right]. \tag{4.52}$$

Since in this case $f\left(P_{inp}\right) = a_i \cdot P_{inp} + b_i$, $i \in \{1, 2, \ldots, q\}$:

$$\check{P}_{out} = a_i \cdot P_{inp} + s \cdot b_i, \qquad i \in \{1, 2, \ldots, q\}, \tag{4.53}$$

$$\check{P}_{out} \in s \cdot \left[P_{out}^{min}, P_{out}^{max}\right]. \tag{4.54}$$

One important limitation of the existing convex approaches with able to optimize the size of the components is that moment of inertia of the rotational parts is neglected. This limitation can be lifted/overcome with the piecewise affine modeling and the assumption that the base rotational inertia of the main components can be scaled by $s^{5/3}$. This assumption is presented in [4]. Since $s^{5/3}$ is a convex function, we can approximate it with arbitrary accuracy, see Fig. 4.22, and thus extend the results of [41, 113] to include the moment of inertia of the main components with rotating parts in the problem formulation.

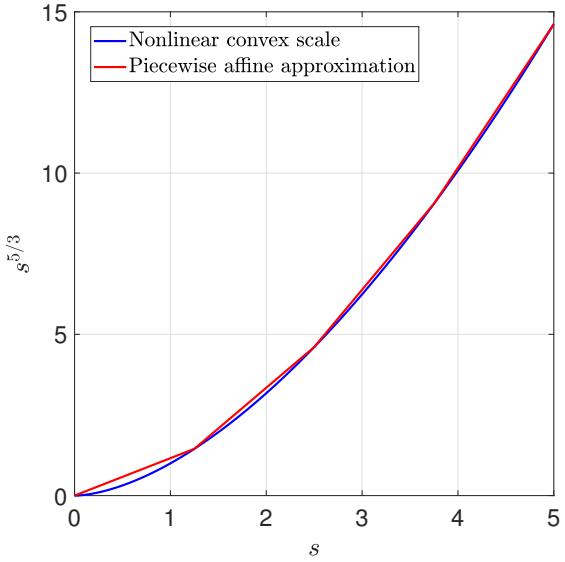

FIGURE 4.22: Nonlinear convex moment of inertia scale [4] and its piecewise affine approximation with 4 line segments.

4.6 Conclusions

A simultaneous approach for architecture design and EMS of HEV has been presented. The problem formulation is based on MILP. The main assumption taken is that despite the NP-hard nature of MILP, cutting-edge solvers are capable of solving big enough problems to be of practical use in a relatively short time. One of the main limitations is that it underestimates the importance of the transmission components. There are several possible ways of extending the presented results. One of them is to extend the results to the design of maritime hybrid powertrains where the number of energy storage and energy converter components is bigger than in a HEV. Another possible extension is to consider optimally fitted piecewise loss models in order to improve the accuracy of the approach. Piecewise affine models could also be exploited to extend the results of [41, 113] to no longer neglect the moment of inertia of the main components. The semidefinite programming convex formulation of a power-split HEV recently presented in [122] might also be approximated by a LP formulation in order to optimally parametrize its main components. Having a LP formulation is more convenient than a SOCP or a SDP formulation due to the fact that LP is a more mature technology and as such its solvers are expected to be more widely available, to be faster, and to produce more reliable solutions.

Chapter 5

Conclusions

More than two decades after it began to be widely studied, hybrid vehicle technology is still a highly active field of research. Three important topics inside this field of research have been considered in this work:

- Regarding EMS, a methodology based on the Pontryagin minimum principle, penalty functions, and an implicit Hamiltonian representation has been proposed in order to compute the offline EMS under mixed input-state constraints. The methodology is illustrated via two application examples. This approach might be extended to conceive a real-time EMS. The most straightforward way to do so is to conceive a model predictive control (MPC) approach [84]. Nevertheless, an approach similar to ECMS would be more convenient as it requires much less computation resources to be implemented.

- Regarding how to use the extra degrees-of-freedom in the powertrain beyond the EMS, a damping control law has been designed and implemented to mitigate the driveline oscillations. The control law achieves the objective of not interfering with the EMS in a significant way: it is found that it increases fuel consumption only in a +0.26% for a synthetic driving mission designed to have a high number of steep torque changes in a short period of time (an scenario unlikely to occur in real-life). This is achieved by designing the control law with a vanishing behavior whenever the system tends to steady-state. The dynamics used for its design are based on a P_0 parallel HEV and it includes (CAN bus induced) time-delays. A robustness analysis with respect to parametric uncertainty is presented. The control law is validated via experimental results achieving up to a 30% of oscillations reduction. Future work on this topic will include a model of the clutch in the control problem formulation. By doing this, gearshifting phases could be taken into account, further increasing the usefulness of the control law.

- At last, regarding how to optimally conceive a powertrain architecture, a simultaneous approach for architecture design and EMS of HEVs is presented. The problem formulation is based on MILP. The main assumption taken is that despite the NP-hard nature of MILP, cutting-edge solvers are capable of solving big enough problems to be of practical use in a relatively short period of time. One of the main limitations of the approach is that it underestimates the importance of the transmission components. There are several possible ways of extending the presented results. One of them is to extend the results to the design of maritime hybrid powertrains, where the number of energy storage and energy converter components is bigger than in a HEV. Another possible extension is to consider optimally fitted piecewise loss models in order to improve the accuracy of the approach. Piecewise affine models could also be exploited to extend the results of [41, 113] to no longer neglect the moment of inertia of the main components. The semidefinite programming (SDP) convex formulation of a power-split HEV recently presented in [122] might also be approximated by a LP formulation in order to include optimal parametrization of its main components. Having a LP formulation is more convenient than a SOCP or a SDP formulation due to the fact that LP is a more mature technology and as such its solvers are expected to be more widely available, faster, and produce more reliable solutions.

Appendix A

A.1 Function extension with multiple variables

Let us consider $f_i \in X_i \subset \mathbb{R}^{n_i}$, where X_i is a convex region and f_i is C^∞. The Taylor series expansion of f_i around of $\tilde{x}$ is defined as follows:

$$\begin{aligned} f_i(x) =& f_i(\tilde{x}) + (x-\tilde{x})^T \nabla f_i(\tilde{x}) + \\ &+ \frac{1}{2}(x-\tilde{x})^T \nabla^2 f_i(\tilde{x})(x-\tilde{x}) + \dots \end{aligned}$$

With ∇f_i and $\nabla^2 f_i$ defined as the gradient and Hessian matrix of f_i, respectively. Given $\tilde{x} \in \partial X_i$, and $y \notin X$, the domain of f_i is extended outside X_i by the following function:

$$g_i(y) = f_i(\tilde{x}) + (y-\tilde{x})^T \nabla f_i(\tilde{x}) + \frac{1}{2}(y-\tilde{x})^T \nabla^2 f_i(\tilde{x})(y-\tilde{x}), \tag{A.1}$$

where $\tilde{x}$ is defined as the closest point on the boundary of X_i, ∂X_i, with respect to y.

A.2 Piecewise polynomial approximation of the the power demand and the On/Off signal command

The time derivatives of the power demand, $\dot{w}(t)$, and the On/Off command of the APU, $\dot{\vartheta}(t)$, are necessary to compute the optimal control dynamics $\dot{u}^*(t)$, see (2.32). Since these signals are not available, a monotone piecewise cubic interpolation [123] is applied to $w(t)$ and $\vartheta(t)$ in order to approximate them. The interpolating polynomials of $w(t)$ and $\vartheta(t)$, denoted as $p_w(t)$ and $p_\vartheta(t)$, respectively, are guaranteed to be at least once continuously differential. The difference between the signals and its piecewise cubic approximations can be arbitrarily reduced by increasing the number of interpolating points at the cost of a greater computational effort.

The computation of the interpolating polynomials is carried out using a predefined Matlab function: *pchip*. Once $p_w(t)$ and $p_\vartheta(t)$ have been computed, $\dot{p}_w(t)$ and $\dot{p}_\vartheta(t)$ are used to approximate $\dot{w}(t)$ and $\dot{\vartheta}(t)$, respectively.

A.3 Efficiency and BSFC maps

The APU model computed using a static efficiency map for the generator and a BSFC map for the engine [80, 124], see Fig. A.1. The traction motor is modeled using a static efficiency map $\eta_{tm}(T_{tm}, \omega_{tm})$, see Fig. A.2.

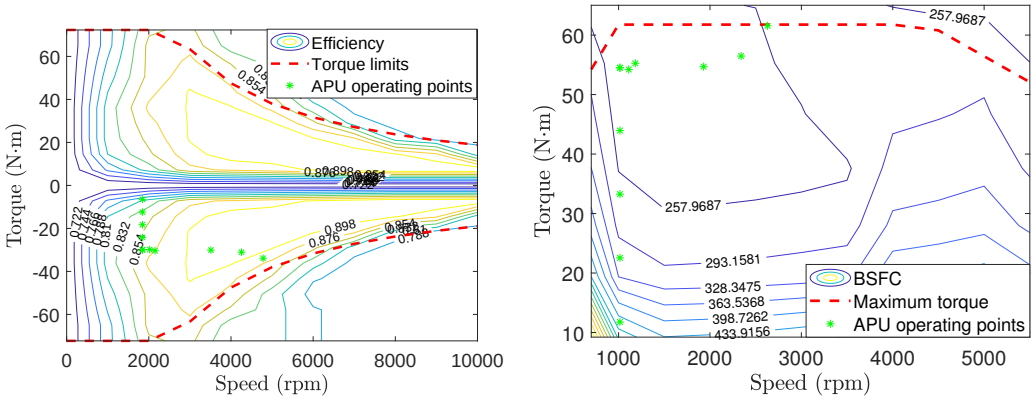

FIGURE A.1: Efficiency map of the generator (left). Brake specific fuel consumption (BSFC) map (g/kWh) of the ICE (right).

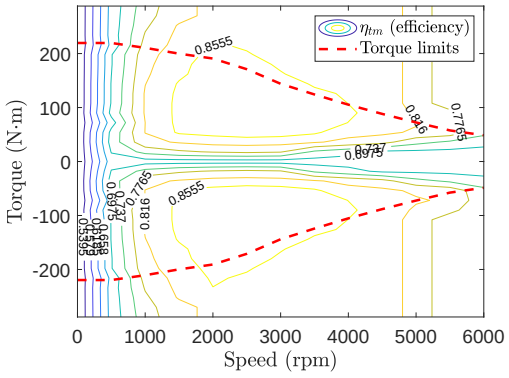

FIGURE A.2: Efficiency map of the traction motor η_{tm}.

Fuel consumption model (2.47) is computed using a quadratic fitting for a set of optimal pairs $\left\{\dot{m}_f^k(T_{ice}^k, \omega_{ice}^k), u^k\right\}$, where T_{ice}^k and ω_{ice}^k are the ICE operating conditions necessary to generate u^k electric power with minimum fuel consumption. The optimal pairs correspond to the APU operating conditions shown in Fig. A.1. $\dot{m}_f^k$ is computed

by solving the following optimization problem for each u^k:

$$\min_{T_{ice},\omega_{ice}} \quad \dot{m}_f(T_{ice},\omega_{ice}), \tag{A.2}$$

$$\text{subject to:} \tag{A.3}$$

$$\eta_{gen}(T_{gen},\omega_{gen}) \cdot T_{gen} \cdot \omega_{gen} = u^k, \tag{A.4}$$

$$T_{ice} = T_{gen} \cdot \rho, \tag{A.5}$$

$$\omega_{ice} = \frac{\omega_{ice}}{\rho}, \tag{A.6}$$

$$\underline{\omega}_{gen} \geq \omega_{gen}(t) \geq \bar{\omega}_{gen}, \tag{A.7}$$

$$\underline{\omega}_{ice} \geq \omega_{ice}(t) \geq \bar{\omega}_{ice}, \tag{A.8}$$

$$\underline{T}_{gen}(\omega_{gen}(t)) \geq T_{gen}(t) \geq \bar{T}_{gen}(\omega_{gen}(t)), \tag{A.9}$$

$$\underline{T}_{ice}(\omega_{ice}(t)) \geq T_{ice}(t) \geq \bar{T}_{ice}(\omega_{ice}(t)), \tag{A.10}$$

$$\tag{A.11}$$

with T_{gen} and ω_{gen} the torque and speed of the generator, respectively, and ρ the gear ratio between the ICE and the generator.

Appendix B

Optimal vs suboptimal EMS architecture design

Consider the pre- vs post-transmission architecture design problem for a parallel HEV shown in Fig. B.1. The fuel consumption of both topologies will be compared using an optimal and a sub-optimal rule-based gearshifting strategy:

(a) **Sub-optimal EMS**: Considering the driving mission and gearshifting strategy of Fig. B.2 the EMS for both architectures are compared in Fig. B.3. Their total fuel consumption values achieved are compared in Table B.1.

(b) **Optimal EMS**: Optimizing the gearshifting signal and considering the velocity profile of Fig. B.2, the EMS for both topologies is shown in Fig. B.4. The total fuel consumption values achieved are compared in Table B.1.

Case	Architecture	Fuel consumption	Difference	Computation time
(a)	Pre-transmission	6.382 l/100km	-	59.563 seconds
	Post-transmission	6.356 l/100km	-0.407 %	59.218 seconds
(b)	Pre-transmission	4.505 l/100km	-	$2.481 \cdot 10^3$ seconds
	Post-transmission	3.294 l/100km	-26.881 %	$2.338 \cdot 10^3$ seconds

TABLE B.1: Fuel consumption comparison for both cases and both architectures.

In both cases it can be concluded that the post-transmission architecture is the best topology. However, when a sub-optimal EMS is considered, the difference in total fuel consumption is less than 0.5 %, whereas, when a optimal EMS is used, the difference goes up to 26.881 %. Therefore, using suboptimals EMS could lead to the designer

underestimating the true potential of the optimal architecture with respect to the rest of the candidates.

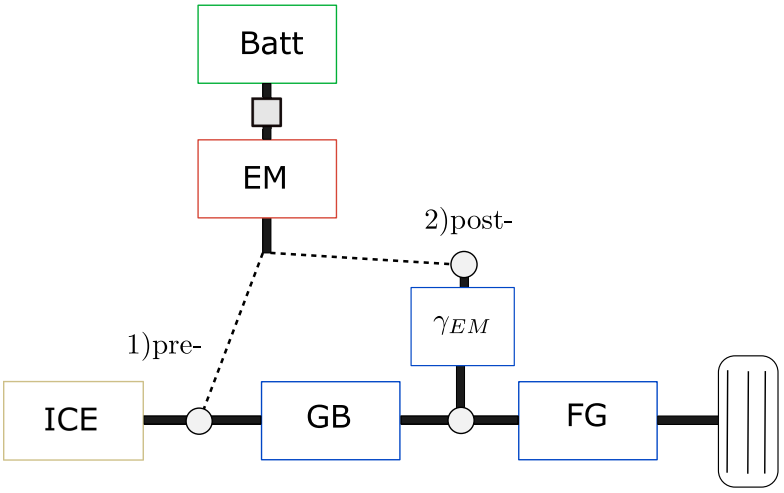

FIGURE B.1: Diagram explaining the architecture design problem.

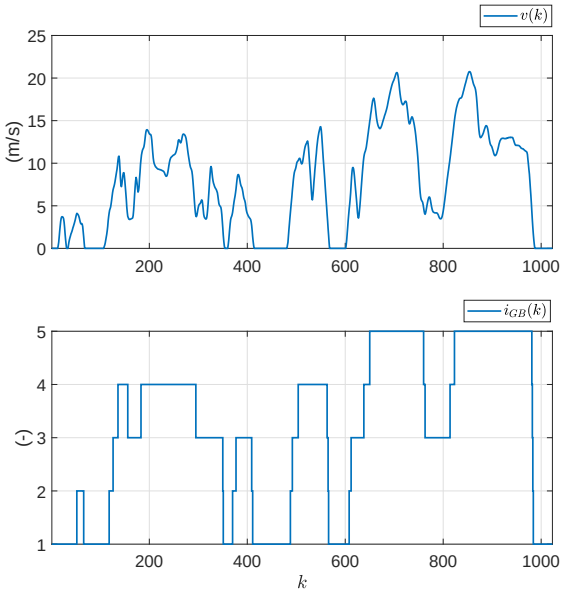

FIGURE B.2: Top: velocity profile; bottom: rule-based gearshifting strategy.

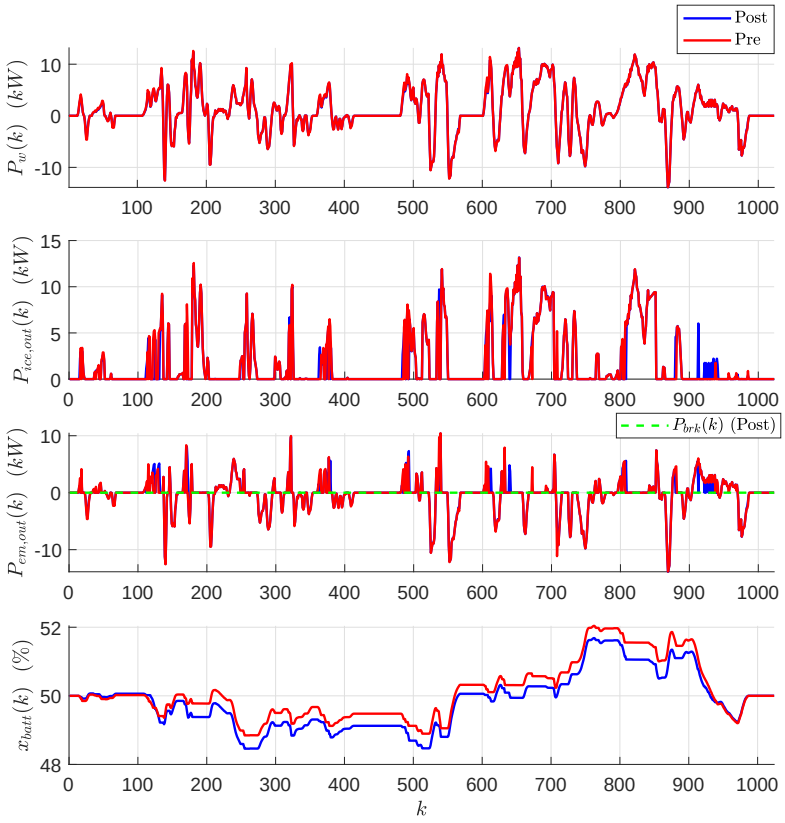

FIGURE B.3: Comparison between architecture (1) and architecture (2) subject to the gearshifting strategy shown in Fig. B.2.

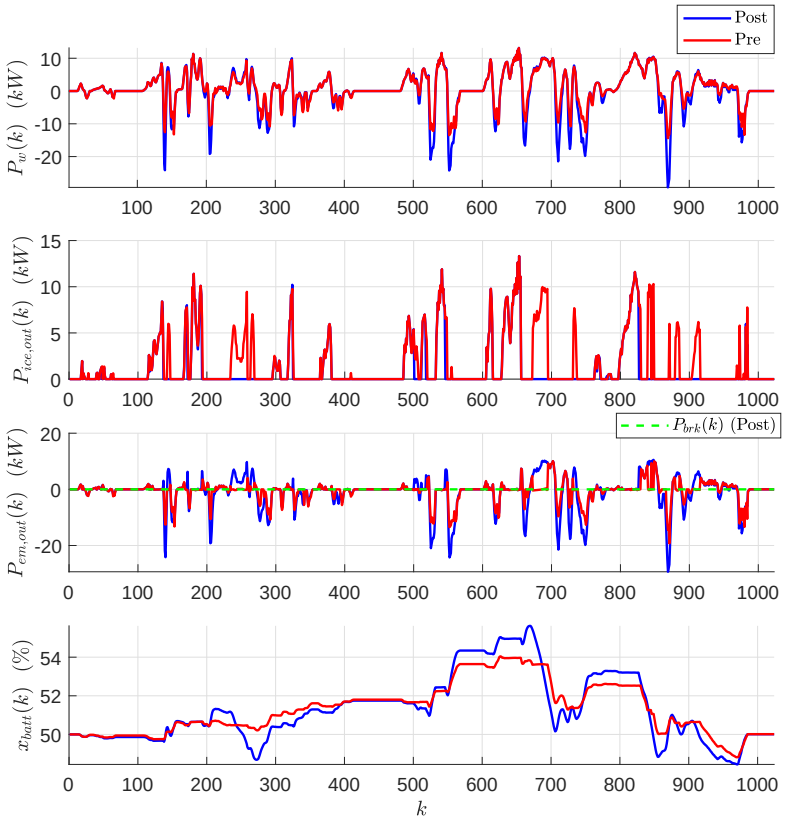

FIGURE B.4: Comparison between EMS for architecture (1) and architecture (2) with an optimized gearshifting.

Appendix C

Parameters of the case study problem

The table below contains the parameters considered in the case study from Chapter 4.

Component	Parameter	Value	Units
ICE	a_{ice}	0.3264	1/W
	b_{ice}	$-1.238 \cdot 10^3$	(W)
	$P^{\min}_{ice,out}$	0	W
	$P^{\max}_{ice,out}$	$2.9786 \cdot 10^4$	W
EM_1	$a_{em_1,i}$	$\{0.985, 0.956, 0.927, 0.898$ $0.869, 0.839, 0.810, 0.781$ $1.185, 1.160, 1.136, 1.111$ $1.086, 1.062, 1.037, 1.012\}$	1/W
	$b_{em_1,i}$	$\{-0.745, -0.573, -0.279, 0.137$ $0.674, 1.332, 2.112, 3.014$ $1.342, 0.776, 0.297, -0.094$ $-0.399, -0.617, -0.748, -0.792\}$	(kW)
	$P^{\min}_{em_1,out}$	$-3.0438 \cdot 10^4$	W
	$P^{\max}_{em_1,out}$	$3.0438 \cdot 10^4$	W
EM_2	$a_{em_2,i}$	$\{0.985, 0.956, 0.927, 0.898$ $0.869, 0.839, 0.810, 0.781$ $1.185, 1.160, 1.136, 1.111$ $1.086, 1.062, 1.037, 1.012\}$	1/W

	$b_{em_2,i}$	$\{-0.745, -0.573, -0.279, 0.137$ $0.674, 1.332, 2.112, 3.014$ $1.342, 0.776, 0.297, -0.094$ $-0.399, -0.617, -0.748, -0.792\}$	(kW)
	$P^{\min}_{em_1,out}$	$-3.0438 \cdot 10^4$	W
	$P^{\max}_{em_1,out}$	$3.0438 \cdot 10^4$	W
Batt	$a_{batt,i}$	$\{0.985, 0.955, 0.925, 0.895$ $0.865, 0.835, 0.805, 0.775$ $1.225, 1.195, 1.165, 1.135$ $1.105, 1.075, 1.045, 1.015\}$	1/W
	b_{batt_i}	$\{0.0, 56.25, 168.75, 337.5$ $562.5, 843.75, 1181.25, 1575.0$ $1575.0, 1181.25, 843.75, 562.5$ $337.5, 168.75, 56.25, 0.0\}$	(W)
	$P^{\min}_{batt,out}$	$-15 \cdot 10^3$	W
	$P^{\max}_{batt,out}$	$15 \cdot 10^3$	W
	A_{batt}	0	(-)
	$B_{batt,inp}$	$-1/E \cdot Q$	1/J
	R	0.5	(Ω)
	E	250	(V)
	Q	$3 \cdot 10^4$	(A·s)
T	$a_{T,i}$	$\{0.95, 1.526\}$	1/W
	$b_{T,i}$	$\{0, 0\}$	(kW)

TABLE C.1: Parameter values for the parallel HEV powertrain power network.

Bibliography

[1] Joris Jaguemont, Loïc Boulon, and Yves Dubé. Characterization and modeling of a hybrid-electric-vehicle lithium-ion battery pack at low temperatures. *IEEE Transactions on Vehicular Technology*, 65(1):1–14, 2016.

[2] Clément Fontaine, Sébastien Delprat, Sébastien Paganelli, and Jérome Bodelle. Automotive fuel economy improvement by micro hybridization. In *Transport Research Arena 2014*, 2014.

[3] R.D. Geertsma, R.R. Negenborn, K. Visser, and J.J. Hopman. Design and control of hybrid power and propulsion systems for smart ships: A review of developments. *Applied Energy*, 194:30–54, 2017.

[4] Bilal Kabalan. *Systematic methodology for generation and design of hybrid vehicle powertrains*. Theses, Université de Lyon, March 2020. URL https://tel.archives-ouvertes.fr/tel-02863337.

[5] Emilia Silvas, Theo Hofman, Alexander Serebrenik, and Maarten Steinbuch. Functional and cost-based automatic generator for hybrid vehicles topologies. *IEEE/ASME Transactions on Mechatronics*, 20(4):1561–1572, 2015.

[6] Conor K. Gately, Lucy R. Hutyra, Scott Peterson, and Ian Sue Wing. Urban emissions hotspots: Quantifying vehicle congestion and air pollution using mobile phone gps data. *Environmental Pollution*, 229:496–504, 2017.

[7] Leonard M. Zwack, Christopher J. Paciorek, John D. Spengler, and Jonathan I. Levy. Modeling spatial patterns of traffic-related air pollutants in complex urban terrain. *Environmental Health Perspectives*, 119(6):852–859, 2011.

[8] John F.B. Mitchell. The "greenhouse" effect and climate change. *Reviews of Geophysics*, 27(1):115–139, 1989.

[9] Thomas R. Karl and Kevin E. Trenberth. Modern global climate change. *Science*, 302(5651):1719–1723, 2003.

[10] European Environmental Agency. Greenhouse gas emissions from transport in europe. https://www.eea.europa.eu/data-and-maps/indicators/transport-emissions-of-greenhouse-gases/transport-emissions-of-greenhouse-gases-12/, 2019. [Online; accessed 23-04-2020].

[11] Zifei Yang and Anup Bandivadekar. Light-duty vehicle greenhouse gas and fuel economy standards. *ICCT report*, 2017.

[12] ICCT. EU: Light-duty: GHG emissions. http://www.transportpolicy.net/standard/eu-light-duty-ghg-emissions/, 2018. [Online; accessed 22-04-2020].

[13] Enviromental Protection Agency (EPA). https://www.fueleconomy.gov/feg/Find.do?action=sbs&id=42510&id=42016, 2020. [Online; accessed 22-04-2020].

[14] Emission Analytics. https://www.emissionsanalytics.com/news/hybrids-are-better, 2019. [Online; accessed 22-04-2020].

[15] Teresa Mendiara, Francisco García-Labiano, A. Abad, P. Gayán, L.F. de Diego, M.T. Izquierdo, and J. Adánez. Negative CO_2 emissions through the use of biofuels in chemical looping technology: a review. *Applied Energy*, 232:657–684, 2018.

[16] P.K. Senecal and Felix Leach. Diversity in transportation: Why a mix of propulsion technologies is the way forward for the future fleet. *Results in Engineering*, 4: 100060, 2019.

[17] Lino Guzzella and Antonio Sciarretta. *Vehicle Propulsion Systems: Introduction to Modeling and Optimization*. Springer Science & Business Media, 2012.

[18] Dongsuk Kum, Huei Peng, and Norman K. Bucknor. Optimal energy and catalyst temperature management of plug-in hybrid electric vehicles for minimum fuel consumption and tail-pipe emissions. *IEEE Transactions on Control Systems Technology*, 21(1):14–26, 2013.

[19] Pierre Michel, Alain Charlet, Guillaume Colin, Yann Chamaillard, Gérard Bloch, and Cédric Nouillant. Optimizing fuel consumption and pollutant emissions of gasoline-HEV with catalytic converter. *Control Engineering Practice*, 61:198–205, 2017.

[20] Daniel F. Opila, Xiaoyong Wang, Ryan McGee, R. Brent Gillespie, Jeffrey A. Cook, and Jessy W. Grizzle. An energy management controller to optimally trade off fuel economy and drivability for hybrid vehicles. *IEEE Transactions on Control Systems Technology*, 20(6):1490–1505, 2012.

[21] Thomas Miro-Padovani, Guillaume Colin, Ahmed Ketfi-Chérif, and Yann Chamaillard. Implementation of an energy management strategy for hybrid electric vehicles including drivability constraints. *IEEE Transactions on Vehicular Technology*, 65(8):5918–5929, 2016.

[22] Soren Ebbesen, Philipp Elbert, and Lino Guzzella. Battery state-of-health perceptive energy management for hybrid electric vehicles. *IEEE Transactions on Vehicular technology*, 61(7):2893–2900, 2012.

[23] Antonio Sciarretta, Domenico di Domenico, Philippe Pognant-Gros, and Gianluca Zito. Optimal energy management of automotive battery systems including thermal dynamics and aging. In *Optimization and Optimal Control in Automotive Systems*, pages 219–236. Springer, 2014.

[24] Cong Hou, Minggao Ouyang, Liangfei Xu, and Hewu Wang. Approximate Pontryagin's minimum principle applied to the energy management of plug-in hybrid electric vehicles. *Applied Energy*, 115:174–189, 2014.

[25] Hoseinali Borhan, Ardalan Vahidi, Anthony M. Phillips, Ming L. Kuang, Ilya V. Kolmanovsky, and Stefano Di Cairano. MPC-based energy management of a power-split hybrid electric vehicle. *IEEE Transactions on Control Systems Technology*, 20(3):593–603, 2011.

[26] Pierluigi Pisu and Giorgio Rizzoni. A comparative study of supervisory control strategies for hybrid electric vehicles. *IEEE Transactions on Control Systems Technology*, 15(3):506–518, 2007.

[27] John. T.B.A. Kessels, Michiel W.T. Koot, Paul P.J. Van Den Bosch, and Daniel B. Kok. Online energy management for hybrid electric vehicles. *IEEE Transactions on Vehicular Technology*, 57(6):3428–3440, 2008.

[28] Stefano Di Cairano, Daniele Bernardini, Alberto Bemporad, and Ilya V. Kolmanovsky. Stochastic MPC with learning for driver-predictive vehicle control and its application to HEV energy management. *IEEE Transactions on Control Systems Technology*, 22(3):1018–1031, 2013.

[29] Jiankun Peng, Hongwen He, and Rui Xiong. Rule based energy management strategy for a series–parallel plug-in hybrid electric bus optimized by dynamic programming. *Applied Energy*, 185:1633–1643, 2017.

[30] Chan-Chiao Lin, Jun-Mo Kang, JW Grizzle, and Huei Peng. Energy management strategy for a parallel hybrid electric truck. In *Proceedings of the 2001 American Control Conference.(Cat. No. 01CH37148)*, volume 4, pages 2878–2883. IEEE, 2001.

[31] Gino Paganelli, Sebastien Delprat, Thierry-Marie Guerra, Janette Rimaux, and Jean-Jacques Santin. Equivalent consumption minimization strategy for parallel hybrid powertrains. In *Vehicular Technology Conference. IEEE 55th Vehicular Technology Conference. VTC Spring 2002 (Cat. No. 02CH37367)*, volume 4, pages 2076–2081. IEEE, 2002.

[32] Simona Onori, Lorenzo Serrao, and Giorgio Rizzoni. Adaptive equivalent consumption minimization strategy for hybrid electric vehicles. In *Dynamic Systems and Control Conference*, volume 44175, pages 499–505, 2010.

[33] Emilia Silvas, Theo Hofman, Nikolce Murgovski, L.F. Pascal Etman, and Maarten Steinbuch. Review of optimization strategies for system-level design in hybrid electric vehicles. *IEEE Transactions on Vehicular Technology*, 66(1):57–70, 2016.

[34] Richard Ernest Bellman. *Dynamic Programming*. Courier Dover Publications, 1957.

[35] Chan-Chiao Lin, Huei Peng, Jessy W Grizzle, and Jun-Mo Kang. Power management strategy for a parallel hybrid electric truck. *IEEE Transactions on Control Systems Technology*, 11(6):839–849, 2003.

[36] Soren Ebbesen, Christian Dönitz, and Lino Guzzella. Particle swarm optimisation for hybrid electric drive-train sizing. *International Journal of Vehicle Design*, 58 (2-4):181–199, 2012.

[37] Mehdi Ansarey, Masoud Shariat Panahi, Hussein Ziarati, and Mohammad Mahjoob. Optimal energy management in a dual-storage fuel-cell hybrid vehicle using multi-dimensional dynamic programming. *Journal of Power Sources*, 250:359–371, 2014.

[38] Yalian Yang, Xiaosong Hu, Huanxin Pei, and Zhiyuan Peng. Comparison of power-split and parallel hybrid powertrain architectures with a single electric machine: Dynamic programming approach. *Applied Energy*, 168:683–690, 2016.

[39] Yuan Zhu, Yaobin Chen, Guangyu Tian, Hao Wu, and Quanshi Chen. A four-step method to design an energy management strategy for hybrid vehicles. In *Proceedings of the 2004 American control conference*, volume 1, pages 156–161. IEEE, 2004.

[40] Z. Khalik, G.P. Padilla, T.C.J. Romijn, and M.C.F. Donkers. Vehicle energy management with ecodriving: A sequential quadratic programming approach with dual decomposition. In *2018 Annual American Control Conference (ACC)*, pages 4002–4007. IEEE, 2018.

[41] Mitra Pourabdollah, Emilia Silvas, Nikolce Murgovski, Maarten Steinbuch, and Bo Egardt. Optimal sizing of a series PHEV: Comparison between convex optimization and particle swarm optimization. *IFAC-PapersOnLine*, 48(15):16–22, 2015. 4th IFAC Workshop on Engine and Powertrain Control, Simulation and Modeling E-COSM 2015.

[42] T. Constantijn J. Romijn, M.C.F. Donkers, John T.B.A. Kessels, and Siep Weiland. A distributed optimization approach for complete vehicle energy management. *IEEE Transactions on Control Systems Technology*, (99):1–17, 2018.

[43] Edward D. Tate and Stephen P. Boyd. Finding ultimate limits of performance for hybrid electric vehicles. Technical report, SAE Technical Paper, 2000.

[44] Mohd Azrin Mohd Zulkefli and Zongxuan Sun. Fast numerical powertrain optimization strategy for connected hybrid electric vehicles. *IEEE Transactions on Vehicular Technology*, 2019.

[45] Mitra Pourabdollah, Nikolce Murgovski, Anders Grauers, and Bo Egardt. Optimal sizing of a parallel PHEV powertrain. *IEEE Transactions on Vehicular Technology*, 62(6):2469–2480, 2013.

[46] Pierre Riedinger, C. Iung, and F. Kratz. An optimal control approach for hybrid systems. *European Journal of Control*, 9(5):449–458, 2003.

[47] Viet Ngo, Theo Hofman, Maarten Steinbuch, and Alex Serrarens. Optimal control of the gearshift command for hybrid electric vehicles. *IEEE Transactions on Vehicular Technology*, 61(8):3531–3543, 2012.

[48] Alexandre Chasse and Antonio Sciarretta. Supervisory control of hybrid powertrains: An experimental benchmark of offline optimization and online energy management. *Control Engineering Practice*, 19(11):1253–1265, 2011.

[49] Sébastien Delprat, Theo Hofman, and Sébastien Paganelli. Hybrid vehicle energy management: Singular optimal control. *IEEE Transactions on Vehicular Technology*, 66(11):9654–9666, 2017.

[50] Thijs van Keulen, Jan Gillot, Bram de Jager, and Maarten Steinbuch. Solution for state constrained optimal control problems applied to power split control for hybrid vehicles. *Automatica*, 50(1):187–192, 2014.

[51] T. Kareemulla, S. Delprat, and L. Czelecz. State constrained hybrid vehicle optimal energy management: an interior penalty approach. *IFAC-PapersOnLine*, 50 (1):10040–10045, 2017. 20th IFAC World Congress.

[52] Jihun Han, Antonio Sciarretta, and Nicolas Petit. Handling state constraints in fast-computing optimal control for hybrid powertrains. *IFAC-PapersOnLine*, 50 (1):4781–4786, 2017. 20th IFAC World Congress.

[53] Marcelino Sanchez and Sebastien Delprat. Hybrid vehicle energy management: Avoiding the explicit hamiltonian minimization. In *2018 IEEE Vehicle Power and Propulsion Conference (VPPC)*, pages 1–5. IEEE, 2018.

[54] Chun Wang, Ruixin Yang, and Quanqing Yu. Wavelet transform based energy management strategies for plug-in hybrid electric vehicles considering temperature uncertainty. *Applied Energy*, 256:113928, 2019.

[55] Constantin F. Caruntu, Mircea Lazar, Rob H. Gielen, P.P.J. Van den Bosch, and Stefano Di Cairano. Lyapunov based predictive control of vehicle drivetrains over can. *Control Engineering Practice*, 21(12):1884–1898, 2013.

[56] Junzhi Zhang, Yutong Li, Chen Lv, Jinfang Gou, and Ye Yuan. Time-varying delays compensation algorithm for powertrain active damping of an electrified vehicle equipped with an axle motor during regenerative braking. *Mechanical Systems and Signal Processing*, 87:45–63, 2017.

[57] Weichao Zhuang, Xiaowu Zhang, Huei Peng, and Liangmo Wang. Rapid configuration design of multiple-planetary-gear power-split hybrid powertrain via mode combination. *IEEE/ASME Transactions on Mechatronics*, 21(6):2924–2934, 2016.

[58] Hamed Ahmadi and José R Martí. Mathematical representation of radiality constraint in distribution system reconfiguration problem. *International Journal of Electrical Power & Energy Systems*, 64:293–299, 2015.

[59] Tobias Nüesch, Philipp Elbert, Michael Flankl, Christopher Onder, and Lino Guzzella. Convex optimization for the energy management of hybrid electric vehicles considering engine start and gearshift costs. *Energies*, 7(2):834–856, 2014.

[60] S. Hadj-Said, Guillaume Colin, A. Ketfi-Cherif, and Y. Chamaillard. Convex optimization for energy management of parallel hybrid electric vehicles. *IFAC-PapersOnLine*, 49(11):271 – 276, 2016. 8th IFAC Symposium on Advances in Automotive Control AAC 2016.

[61] Michael Grant, Stephen Boyd, and Yinyu Ye. Disciplined convex programming. In *Global optimization*, pages 155–210. Springer, 2006.

[62] Michael Grant and Stephen Boyd. CVX: Matlab software for disciplined convex programming, version 2.1, 2014.

[63] Lev Semenovich Pontryagin. The mathematical theory of optimal processes. 1962.

[64] Donald E. Kirk. *Optimal control theory: an introduction*. Courier Corporation, 2012.

[65] L. Lasdon, A. Waren, and R. Rice. An interior penalty method for inequality constrained optimal control problems. *IEEE Transactions on Automatic Control*, 12(4):388–395, 1967.

[66] Milind M. Lele and David H. Jacobson. A proof of the convergence of the Kelley-Bryson penalty function technique for state-constrained control problems. *Journal of Mathematical Analysis and Applications*, 26(1):163–169, 1969.

[67] D. Subbaram Naidu. *Optimal control systems*. CRC press, 2002.

[68] George M. Siouris. *An engineering approach to optimal control and estimation theory*. John Wiley & Sons, Inc., 1996.

[69] Uri M. Ascher, Robert M.M. Mattheij, and Robert D. Russell. *Numerical solution of boundary value problems for ordinary differential equations*, volume 13. SIAM, 1994.

[70] Jacek Kierzenka and Lawrence F. Shampine. A BVP solver based on residual control and the Maltab PSE. *ACM Transactions on Mathematical Software*, 27 (3):299–316, 2001.

[71] Marcelino Sánchez, Sébastien Delprat, and Theo Hofman. Energy management of hybrid vehicles with state constraints: A penalty and implicit hamiltonian minimization approach. *Applied Energy*, 260:114149, 2020.

[72] Nicolas Petit and Antonio Sciarretta. Optimal drive of electric vehicles using an inversion-based trajectory generation approach. *IFAC Proceedings Volumes*, 44 (1):14519–14526, 2011. 18th IFAC World Congress.

[73] J. Frédéric Bonnans and Audrey Hermant. Second-order analysis for optimal control problems with pure state constraints and mixed control-state constraints. In *Annales de l'Institut Henri Poincare (C) Non Linear Analysis*, volume 26, pages 561–598. Elsevier, 2009.

[74] Brian C. Fabien. Numerical solution of constrained optimal control problems with parameters. *Applied Mathematics and Computation*, 80(1):43–62, 1996.

[75] Knut Graichen and Nicolas Petit. Constructive methods for initialization and handling mixed state-input constraints in optimal control. *Journal Of Guidance, Control, and Dynamics*, 31(5):1334–1343, 2008.

[76] Jiageng Ruan, Paul D. Walker, Peter A. Watterson, and Nong Zhang. The dynamic performance and economic benefit of a blended braking system in a multi-speed battery electric vehicle. *Applied Energy*, 183:1240–1258, 2016.

[77] Thomas Miro Padovani, Maxime Debert, Guillaume Colin, and Yann Chamaillard. Optimal energy management strategy including battery health through thermal management for hybrid vehicles. *IFAC Proceedings Volumes*, 46(21):384–389, 2013. 7th IFAC Symposium on Advances in Automotive Control.

[78] Xinfan Lin, Hector E. Perez, Jason B. Siegel, Anna G. Stefanopoulou, Yonghua Li, R. Dyche Anderson, Yi Ding, and Matthew P. Castanier. Online parameterization of lumped thermal dynamics in cylindrical lithium ion batteries for core temperature estimation and health monitoring. *IEEE Transactions on Control Systems Technology*, 21(5):1745–1755, 2013.

[79] Zhuo Yang, Devendra Patil, and Babak Fahimi. Electrothermal modeling of lithium-ion batteries for electric vehicles. *IEEE Transactions on Vehicular Technology*, 68(1):170–179, 2019.

[80] Nikolce Murgovski, Lars Johannesson, Jonas Hellgren, Bo Egardt, and Jonas Sjöberg. Convex optimization of charging infrastructure design and component sizing of a plug-in series hev powertrain. *IFAC Proceedings Volumes*, 44(1):13052–13057, 2011. 18th IFAC World Congress.

[81] Olle Sundstrom and Lino Guzzella. A generic dynamic programming matlab function. In *2009 IEEE Control Applications,(CCA) & Intelligent Control,(ISIC)*, pages 1625–1630. IEEE, 2009.

[82] Rein Luus. *Iterative dynamic programming*. Chapman and Hall/CRC, 2000.

[83] Felix Merz, Antonio Sciarretta, J-C Dabadie, and Lorenzo Serrao. On the optimal thermal management of hybrid-electric vehicles with heat recovery systems. *Oil & Gas Science and Technology–Revue d'IFP Energies nouvelles*, 67(4):601–612, 2012.

[84] Shaobo Xie, Xiaosong Hu, Zongke Xin, and James Brighton. Pontryagin's minimum principle based model predictive control of energy management for a plug-in hybrid electric bus. *Applied Energy*, 236:893–905, 2019.

[85] C.Y. Mo, A.J. Beaumount, and N.N. Powell. Active control of driveability. Technical report, SAE Technical Paper, 1996.

[86] Jonas Fredriksson, Henrik Weiefors, and Bo Egardt. Powertrain control for active damping of driveline oscillations. *Vehicle System Dynamics*, 37(5):359–376, 2002.

[87] Damien Lefebvre, Philippe Chevrel, and Sébastien Richard. An H_∞-based control design methodology dedicated to the active control of vehicle longitudinal oscillations. *IEEE Transactions on Control Systems Technology*, 11(6):948–956, 2003.

[88] M Berriri, Philippe Chevrel, and D. Lefebvre. Active damping of automotive powertrain oscillations by a partial torque compensator. *Control Engineering Practice*, 16(7):874–883, 2008.

[89] Yongsoon Yoon, Youngse An, Youngjoo Park, and H Jin Kim. Model predictive control for drivability enhancement with input dead-segment. In *ICCAS 2010*, pages 916–921. IEEE, 2010.

[90] Paul D. Walker and Nong Zhang. Active damping of transient vibration in dual clutch transmission equipped powertrains: A comparison of conventional and hybrid electric vehicles. *Mechanism and Machine Theory*, 77:1–12, 2014.

[91] Jonas Fredriksson. Improved driveability of a hybrid electric vehicle using powertrain control. *International Journal of Alternative Propulsion*, 1(1):97–111, 2006.

[92] Fazal U. Syed, Ming L. Kuang, and Hao Ying. Active damping wheel-torque control system to reduce driveline oscillations in a power-split hybrid electric vehicle. *IEEE Transactions on Vehicular Technology*, 58(9):4769–4785, 2009.

[93] Hiromichi Kawamura, Ken Ito, Takaaki Karikomi, and Tomohiro Kume. Highly-responsive acceleration control for the nissan leaf electric vehicle. Technical report, SAE Technical Paper, 2011.

[94] Satoru Fujimoto, Kazutaka Adachi, Hiroyuki Ashizawa, and Jun Motosugi. Hev application of shaking vibration control system based on advanced motor control. Technical report, SAE Technical Paper, 2012.

[95] Sriganesh Sriram and David G. Taylor. Modeling and control of power-split powertrains: Examining the influence of drive-shaft compliance. In *2015 IEEE Transportation Electrification Conference and Expo (ITEC)*, pages 1–6. IEEE, 2015.

[96] Raja Sangili Vadamalu and Christian Beidl. MPC for active torsional vibration reduction of hybrid electric powertrains. *IFAC-PapersOnLine*, 49(11):756–761, 2016. 8th IFAC Symposium on Advances in Automotive Control AAC 2016.

[97] Biqing Zhong, Bin Deng, and Han Zhao. Simulation model and method for active torsional vibration control of an hev. *Applied Sciences*, 9(1):34, 2019.

[98] Hui Liu, Xun Zhang, Yinqi Chen, Mahmoud Taha, and Haoxin Xu. Active damping of driveline vibration in power-split hybrid vehicles based on model reference control. *Control Engineering Practice*, 91:104085, 2019.

[99] Notker Amann, J. Bocker, and Franz Prenner. Active damping of drive train oscillations for an electrically driven vehicle. *IEEE/ASME Transactions on Mechatronics*, 9(4):697–700, 2004.

[100] Jianwu Zhang, Benben Chai, and Xingyang Lu. Active oscillation control of electric vehicles with two-speed transmission considering nonlinear backlash. *Proceedings of the Institution of Mechanical Engineers, Part K: Journal of Multi-body Dynamics*, 234(1):116–133, 2020.

[101] Ioan Doré Landau and Gianluca Zito. *Digital control systems: design, identification and implementation*. Springer Science & Business Media, 2007.

[102] Aman Jacknoon, Mohamed Hassan, and Sami El Ferik. Design of rst controllers based on intelligent optimization algorithms. In *2016 Conference of Basic Sciences and Engineering Studies (SGCAC)*, pages 177–182. IEEE, 2016.

[103] Pinar Civicioglu. Backtracking search optimization algorithm for numerical optimization problems. *Applied Mathematics and computation*, 219(15):8121–8144, 2013.

[104] Riadh Madiouni, Soufiene Bouallegue, Joseph Haggege, and Patrick Siarry. Particle swarm optimization-based design of polynomial rst controllers. In *10th International Multi-Conferences on Systems, Signals & Devices 2013 (SSD13)*, pages 1–7. IEEE, 2013.

[105] Bram De Jager, Thijs Van Keulen, and John Kessels. *Optimal control of hybrid vehicles*. Springer, 2013.

[106] E. Silvas. *Integrated optimal design for hybrid electric vehicles*. PhD thesis, Department of Mechanical Engineering, November 2015. Proefschrift.

[107] Steven Masfaraud, Fabrice Danes, Pierre-Emmanuel Dumouchel, Florian De Vuyst, and Nicolas Vayatis. Automatized gearbox architecture design exploration by exhaustive graph generation. In *WCCM XII 2016*, 2016.

[108] Jan Wijkniet and Theo Hofman. Modified computational design synthesis using simulation-based evaluation and constraint consistency for vehicle powertrain systems. *IEEE Transactions on Vehicular Technology*, 67(9):8065–8076, 2018.

[109] Xiaowu Zhang, Huei Peng, and Jing Sun. A near-optimal power management strategy for rapid component sizing of multimode power split hybrid vehicles. *IEEE Transactions on Control Systems Technology*, 23(2):609–618, 2014.

[110] Nicolò Robuschi, Mauro Salazar, Pol Duhr, Francesco Braghin, and Christopher H. Onder. Minimum-fuel engine on/off control for the energy management of a hybrid electric vehicle via iterative linear programming. *IFAC-PapersOnLine*, 52(5):134–140, 2019. 9th IFAC Symposium on Advances in Automotive Control AAC 2019.

[111] Mitra Pourabdollah, Bo Egardt, Nikolce Murgovski, and Anders Grauers. Effect of driving, charging, and pricing scenarios on optimal component sizing of a phev. *Control Engineering Practice*, 61:217–228, 2017.

[112] X. Wei, L. Guzzella, V. I. Utkin, and G. Rizzoni. Model-Based Fuel Optimal Control of Hybrid Electric Vehicle Using Variable Structure Control Systems. *Journal of Dynamic Systems, Measurement, and Control*, 129(1):13–19, 06 2006. ISSN 0022-0434. doi: 10.1115/1.2397148. URL https://doi.org/10.1115/1.2397148.

[113] Nikolce Murgovski, Lars Johannesson, Jonas Sjöberg, and Bo Egardt. Component sizing of a plug-in hybrid electric powertrain via convex optimization. *Mechatronics*, 22(1):106–120, 2012.

[114] X. Hu, N. Murgovski, L. M. Johannesson, and B. Egardt. Optimal dimensioning and power management of a fuel cell/battery hybrid bus via convex programming. *IEEE/ASME Transactions on Mechatronics*, 20(1):457–468, 2015.

[115] Mitra Pourabdollah, Bo Egardt, Nikolce Murgovski, and Anders Grauers. Convex optimization methods for powertrain sizing of electrified vehicles by using different levels of modeling details. *IEEE Transactions on Vehicular Technology*, 67(3): 1881–1893, 2017.

[116] X. Hu, N. Murgovski, L. M. Johannesson, and B. Egardt. Comparison of three electrochemical energy buffers applied to a hybrid bus powertrain with simultaneous optimal sizing and energy management. *IEEE Transactions on Intelligent Transportation Systems*, 15(3):1193–1205, 2014.

[117] Xiaosong Hu, Lars Johannesson, Nikolce Murgovski, and Bo Egardt. Longevity-conscious dimensioning and power management of the hybrid energy storage system in a fuel cell hybrid electric bus. *Applied Energy*, 137:913–924, 2015.

[118] MOSEK ApS. *The MOSEK optimization toolbox for MATLAB manual. Version 9.0.*, 2019. URL http://docs.mosek.com/9.0/toolbox/index.html.

[119] LLC Gurobi Optimization. Gurobi optimizer reference manual, 2020. URL http://www.gurobi.com.

[120] S. Boyd, L. E. Ghaoui, E. Feron, and V. Belakrishnan. *Linear Matrix Inequalities in System and Control Theory*, volume 15. SIAM: Studies In Applied Mathematics, Philadelphia, USA, 1994.

[121] MOSEK ApS. Mosek modeling cookbook, 2018.

[122] S. Amirfarhangi Bonab and A. Emadi. Fuel-optimal energy management strategy for a power-split powertrain via convex optimization. *IEEE Access*, 8:30854–30862, 2020. doi: 10.1109/ACCESS.2020.2972346.

[123] Frederick N. Fritsch and Ralph E. Carlson. Monotone piecewise cubic interpolation. *SIAM Journal on Numerical Analysis*, 17(2):238–246, 1980.

[124] Zheng Chen, Bing Xia, Chenwen You, and Chunting Chris Mi. A novel energy management method for series plug-in hybrid electric vehicles. *Applied Energy*, 145:172–179, 2015.

Hybrid vehicle design and control

This work is concerned with the development of hybrid electric vehicle technologies. It is split into three main topics: • By taking advantage of the extra degrees of freedom present in a hybrid vehicle, the energetic supervisory control,satisfies the power demand from the driver such that the total fuel consumption is minimized. This supervisory control can be cast as an optimal control problem. The contribution of this work is an approach based on Pontryagin's minimum principle, penalty functions, and an implicit Hamiltonian minimization that allows computing the offline energy management under multiple states subject to path constraints. The proposed approach is shown to be up to 46 times faster than dynamic programming. •In a gear-based transmission, undesired drive-shaft oscillations are mainly noticeable at low gears (and therefore low speeds) when the torsional dynamics of the driveshaft are excited with large torque values. The contribution of this work is the design and implementation of a damping controller able to significantly reduce the undesired oscillations. The controller is implemented by adding a damping torque signal to the reference torque of the electric machine commanded by the energetic supervisory control (energy management strategy). No additional actuators are required for the implementation of the controller. Moreover, the damping controller is effective without significantly interfering with the energetic supervisory control. •The complex task of automatically computing the optimal powertrain architecture design subsumes several other important tasks such as the optimization of the supervisory control, the technology of the powertrain components, and the parametrization of such components. In this work, building upon existing results, the powertrain components are fitted into piecewise affine convex models. In this convex formulation, the hybrid powertrain is seen as a power network. The main contribution is the formulation of the energy management and the architecture design in a simultaneous framework via mixed-integer linear programming.

Conception et commande de véhicules hybrides

La thèse s'intéresse au développement des technologies de véhicules hybrides. Elle comprend trois thèmes principaux : •En portant des degrés de liberté supplémentaires du véhicule hybride, la stratégie de gestion énergétique répond aux demandes de puissance du conducteur de telle manière que la consommation totale d'essence soit minimisée. La contribution sur ce sujet est une méthodologie basée sur le principe du minimum de Pontryagin, des fonctions de pénalité, et la minimisation implicite du Hamiltonien. La méthodologie proposée est capable de calculer la stratégie de gestion énergétique, avec plusieurs contraintes sur les états. La méthodologie est illustrée avec deux exemples. Il est montré que la méthodologie proposée est jusqu'à 46 fois plus rapide que la programmation dynamique. •Dans un véhicule avec une boîte de vitesses, la présence des oscillations dans la transmission, qui est plus notable quand le véhicule roule avec le 1^{er} ou 2^{nd} rapport engagé (et donc aux bas vitesses), arrive lorsque la dynamique de torsion de la transmission est excitée par des couples qui changent soudainement et qui atteignent des valeurs considérables. Notre contribution sur ce sujet est la conception et l'implémentation d'une loi de commande réduisant ces oscillations qui diminuent l'agrément de conduite. La commande est mise en œuvre en ajoutant un signal de commande à la consigne de couple de la machine électrique demandée par le superviseur énergétique. La loi de commande ne requiert aucun actionneur supplémentaire. En outre, elle n'interfère pas avec la stratégie de gestion énergétique, et par conséquent, son effet sur la consommation d'essence est négligeable. •Le calcul de l'architecture optimale d'un véhicule hybride est un problème considérablement complexe qui englobe l'optimisation de la stratégie de gestion énergétique, le choix de la technologie des composants du groupe motopropulseur (GMP), et les paramètres de ces composants. Dans ce travail, en s'appuyant sur des résultats existants, le comportement énergétique des composants du groupe motopropulseur est modélisé par des modèles convexes. Avec ces modèles convexes, le GMP hybride est considéré comme un réseau de puissance. La contribution principale est la formulation de la stratégie de gestion énergétique et du choix de l'architecture optimales via un problème de programmation linéaire mixte en nombres entiers.